# Diffraction-Based Detection of Antimicrobial Susceptibility and Mobility of Bacterial Ensembles

**David Volbers**


Munich 2018

# Diffraction-Based Detection of Antimicrobial Susceptibility and Mobility of Bacterial Ensembles

**David Volbers**

PhD-Thesis
at the Department of Physics
at the Ludwig-Maximilians-University
Munich

submitted by
David Volbers
from Herrenberg

Munich, November 16, 2018

Erstgutachter: Prof. Dr. Joachim Rädler
Zweitgutachter: PD Dr. Theobald Lohmüller
Tag der mündlichen Prüfung: 11.1.2019

# Contents

## Zusammenfassung

Antibiotikaresistenzen (ABR) werden zunehmend zu einem ernsthaften Problem im Gesundheitswesen. Die Hauptursache für ABR ist der teils unangemessene und überflüssige Einsatz von Antibiotika. Es wird geschätzt, dass die Zahl der durch ABR verursachten Todesfälle bis 2050 die Zahl der krebsbedingten Todesfälle übersteigen wird. Um eine weitere Verbreitung von ABR zu verhindern, ist es notwendig, bei einer gegeben Infektion so schnell wie möglich ein geeignetes Schmalband-Antibiotikum zu identifizieren. Daher sind Detektionsmethoden, die eine schnelle und hochdurchlässige Form von antimikrobieller Suszeptibilitätstests (AST) ermöglichen, dringend erforderlich.

In dieser Arbeit wird eine Detektionsmethode vorgestellt, die die gleichzeitige Analyse von Wachstum und Mobilität eines Bakterienensembles mit hoher Präzision ermöglicht. Das Verfahren mit dem Namen "Interference Disturbance Analysis" (IDA) basiert auf der zeitlichen Analyse der Intensität eines Beugungspeaks. Ein solcher Beugungspeak entsteht durch die Beleuchtung eines zweidimensionalen Beugungsgitters mit einer kohärenten Laser-Lichtquelle. Die sich oberhalb des Gitters befindenden und bewegenden Bakterien stören die Interferenz der an den einzelnen kreisförmigen Goldstrukturen entstehenden Elementarwellen, was wiederum zu zeitlichen Intensitätsschwankungen des aufgenommenen Beugungspeaks führt.

Um das Funktionsprinzip zu demonstrieren, werden transparente Latex-Beads als nicht lebendes Modellsystem verwendet. Es wird gezeigt, dass die Intensität der Beugungspeaks proportional zur Anzahl der Beads abnimmt. Darüber hinaus erlaubt die Analyse von kurzzeitigen Intensitätsfluktuationen Rückschlüsse auf den Diffusionskoeffizienten von Objekten, die sich oberhalb des Gitters bewegen.

Daraufhin werden *Escherichia coli* Bakterien mit der IDA-Method untersucht. Es wird gezeigt, dass die Intensitätsabnahme direkt proportional zur Zelldichte ist und der Dynamikbereich von einzelnen Bakterien bis zu mehr als 400 Zellen pro Gitter reicht. Die IDA-Methode ermöglicht weiterhin eine quantitative Analyse von Mobilitätsveränderungen in Abhängigkeit von der Zeit und zeigt eine Verringerung des Diffusionskoeffizienten der Bakterien um den Faktor drei während der Anhaftung der Zellen an eine Oberfläche.

Anschließend wird die IDA-Method zur Bestimmung der minimalen Hemmkonzentration (MHK) von drei verschiedenen Antibiotika in jeweils weniger als 2-3 Stunden benutzt. Darüber hinaus wird eine Suszeptibilitätsanalyse in weniger als 40 Minuten präsentiert.

Zusätzlich wird die Wirkung eines photoschaltbaren Antibiotikums untersucht, welches speziell als optische Kontrolle der bakteriellen Mobilität entwickelt wurde. Es wird gezeigt, dass der biologisch aktive Zustand die Wachstumszeiten im Vergleich zum inaktiven Zustand verzögert und dass das photoschaltbare Antibiotikum zu einer Abnahme der bakteriellen Mobilität führt, wobei wiederum eine stärkere Wirkung für den aktiven Zustand gezeigt wird. Analoge Messungen mit einem nicht empfindlichen Bakterienstamm zeigen keine Einschränkung der Mobilität sowie keinen Unterschied zwischen den beiden Zuständen.

Um zu zeigen, dass die IDA-Methode für automatisierte Hochdurchsatzmessungen mit geringen Probenvolumina skalierbar ist, wird ein speziell entwickelter Probenhalter vorgestellt. In diesem Zusammenhang wird ein Setup präsentiert, das die quasisimultane Analyse von 256 Proben mit einem Gesamtprobenvolumen von etwas über 20 µl ermöglicht. Mit Hilfe dieses Setups werden die Auswirkungen sehr kleiner Probenvolumina auf das Wachstum und die Mobilität der Bakterien untersucht. Darüber hinaus werden AST-Messungen in weniger als 100 Nanoliter präsentiert.

Zusammenfassend ermöglicht die IDA-Methode die gleichzeitige und präzise Analyse des Wachstums und der Mobilität bakterieller Ensembles. Hierduch wird ein schneller Test der antimikrobiellen Empfindlichkeit von Bakterien in geringen Probenvolumina bei geringer Zellzahl ermöglicht.

## Summary

Antibiotic resistance (ABR) is becoming an increasingly serious health care issue, arising mainly from the redundant and inappropriate use of antibiotics. It is estimated that the number of deaths due to ABR will surpass the amount of cancer-related deaths by 2050. In order to prevent ABR from further spreading, it is necessary to identify an appropriate narrow-band antibiotic for a given infection as soon as possible. Therefore, detection methods that allow fast and high-throughput antimicrobial susceptibility testing (AST) are highly needed.

In this thesis, a detection method is presented that allows the simultaneous analysis of growth and mobility of a bacterial ensemble with high precision. The method named Interference Disturbance Analysis (IDA) is based on the temporal analysis of the intensity of a diffraction peak. The latter occurs due to the illumination of a two-dimensional diffraction grating with a coherent laser source. Bacteria growing and moving above the grating disturb the interference of the elementary waves originating at the individual circular gold-structures, which in turn leads to temporal intensity fluctuations of the analyzed diffraction peak.

In order to demonstrate the working principle, transparent latex beads are used as a non-living model system. It is presented that the diffraction peak intensity decreases proportionally to the amount of beads. Furthermore, the analysis of short-term intensity fluctuations allows conclusions on the diffusion coefficient of objects moving above the grating.

To evaluate the IDA-method's capability of quantitative bacterial measurements, *Escherichia coli* cells are investigated. It is shown that the intensity-decrease is directly proportional to the bacterial cell density with a dynamic range from single bacteria up to more than 400 cells per grating. The IDA-method further allows a quantitative analysis of mobility changes as a function of time, revealing a decrease of the bacteria's diffusion coefficient by a factor of three during the attachment of the cells to a surface.

Next, the IDA-method is used as an assay for AST by determining the minimum inhibitory concentration (MIC) of three antibiotics and two bacterial species in less than 2-3 hours, respectively. Moreover, the differentiation between a susceptible and a resistant strain can be accomplished in less than 40 minutes.

Additionally, a compound that was designed to optically control the cell-migration of bacteria is investigated with the IDA-method. The photoswitchable, azobene-modified molecule named Azo-PC imitates the FtsZ polymer stabilizing and cell division inhibiting PC190723 agent. It is shown that the biologically active state (trans) delays growth times in comparison to the inactive state (cis) and that the Azo-PC compound leads to a decrease of bacterial mobility, with again a stronger effect measured for the active than for the inactive state. Analogous measurements with a non-susceptible bacterial strain showed no decrease in mobility and no difference between the two states.

To demonstrate that the IDA-method can be scaled for automated high-throughput measurements with low sample volumes, a custom-designed sample holder is introduced. In this context, a setup is finalized that allows the quasi-simultaneous analysis of 256 samples with a total sample volume of just over 20 µl. The setup is further used to investigate the effects of smaller sample volumes on growth and mobility. Moreover, AST measurements in less than 100 nanoliter are presented.

In summary, Interference Disturbance Analysis allows the simultaneous, sensitive evaluation of bacterial growth and mobility. Thus, it enables rapid AST of bacterial strains in low sample volumes while starting from small numbers of cells.

# Chapter 1

# Introduction

"Antibiotic" is a word of Greek origin, which can roughly be translated to 'opposing life' and describes a drug class used in the treatment of bacterial infections. The first antibiotic was discovered in 1928 by Sir Alexander Fleming, who extracted penicillin from the fungus Penicillium rubens [1]. Penicillin inhibits the cell wall synthesis during bacterial growth and cell division, which eventually results in cell death (cytolysis) [78]. The miraculous new drug was initially reserved for the military during World War II [2]. However, as more antibiotics were discovered and the manufacturing processes simplified, the access to antibiotics was facilitated and their use became widely popular. Thus, antibiotics have improved the treatment of infections, revolutionized surgery, paved the way for chemotherapy and were used to facilitate agriculture [3]. However, in the past century, antibiotics were used as a "panacea", a drug of universal remedy and were prescribed to treat the most common and trivial infections, many of which were non-bacterial in nature [4]. In 1945, Sir Alexander Flemming warned in an interview with the *New York Times* that an inappropriate use of penicillin could lead to an increase of resistant mutations of *Staphylococcus aureus* which could in turn lead to more serious infections [5]. It turned out that he was right and within only one year, a large number of *S. aureus* strains became resistant against penicillin [5]. Today, more than 70 years later, the indiscriminate and redundant use of antibiotics continues and has already led to a wide variety of bacteria that are resistant against one or multiple antibiotics [4]. The alarming increase of antibiotic resistance (ABR) in the past years has become a serious global health problem [4][6]. Currently, the number of deaths due to ABR exceeds 700,000 annually and an increase to 10 million per year by 2050 is predicted [7]. Unfortunately, new alternative antibiotics solving this issue are not in sight. One reason for this is that the discovery and permission for clinical usage is extremely time consuming (10 to 25 years) [8]. Moreover, the total development costs per new antibiotic are estimated to exceed 500 million dollars, which makes the effort uneconomical for pharmaceutical companies [8].

In order to find a way to tackle antibiotic resistances, it is crucial to analyze the problem and its origin. Antibiotic resistance is defined as a reduced or non-existent effect of a given antibiotic on the growth of a bacterial strain [9]. The type of resistance can

be distinguished between intrinsic and acquired. Intrinsically resistant bacteria posses the ability to resist an antibiotic due to inherent structural or functional characteristics. However, previously susceptible bacterial strains can acquire antibiotic resistance through horizontal or vertical gene transfer. The former describes the exchange of gene material between two non-relative organisms through mobile genetic elements such as plasmids [10][6]. This allows bacterial ensembles to quickly adapt to new environments [10]. Vertical gene transfer refers to mutations that occur spontaneously or during cell division and the subsequent inheritance of the mutated gene material to following cell generations [9]. Both forms of acquired resistance are an evolutionary process. However, the vast use of antibiotics strongly accelerates this process by applying selective pressure. Broad-spectrum antibiotics, i.e. compounds that act against a wide range of bacteria, are especially damaging [11][12]. After the treatment with a broad-spectrum antibiotic, most of the susceptible bacteria in the host are eliminated. However, a majority of these bacteria are species that naturally occur in the host's microbiome and only resistant bacteria remain [13][14]. Due to the excess of available space and nutrients, the remaining resistant strains proliferate and turn the host into a reservoir of drug resistant bacteria which in turn can spread to other hosts [4][15].

There are two main fields of application that lead to the strong increase in antibiotic resistance: Firstly, antibiotics are extendedly used in livestock in order to promote growth, prevent diseases, produce larger yields and a higher quality product [16]. As a result, antibiotic resistant bacteria arise and reach consumers through meat products [17]. Additionally, the excretion of the bacteria through the livestock's urine and stool leads to an increase of resistant pathogens in the environmental microbiome [17]. The non-therapeutic use of antibiotics in agriculture is highly criticized and negotiations on the reduction of common antibiotics in livestock are in progress in several countries [18]. The second problematic field of application is human health care. The lack of regulations for prescriptions and the possibility to buy antibiotics online have led to a worldwide overuse of these drugs [6]. Furthermore, incorrect prescriptions of antibiotics have caused complications of the patients therapy and have contributed to the increase of resistances. Studies have shown that the treatment indication, therapy duration, or choice of agent are incorrect in 30% to 50% of cases [19][20]. Moreover, 30% to 60% of the antibiotics prescribed in intensive care units were found to be inappropriate, suboptimal or unnecessary [6][20].

A crucial tool in the battle against antibiotic resistances is the determination of an appropriate treatment, also known as antimicrobial susceptibility testing (AST). The term antimicrobial is used to include other microorganisms such as viruses or parasites. Here, however, it refers to the analysis of antimicrobial susceptibility of bacteria. These AST assays usually determine the minimum inhibitory concentration (MIC) of an antibiotic, which is the smallest concentration that inhibits visible growth of bacteria [21]. Breakpoint concentrations of the MIC that differentiate between susceptible and resistant isolates are defined by the European Committee on Antimicrobial Susceptibility Testing

(EUCAST) for all common antibiotics [21]. The typical procedure of AST comprises the extraction of samples from a patients infected body fluids, such as blood or urine, followed by the susceptibility analysis. Frequently used AST techniques in clinical environments are disk diffusion [22][23] and broth microdilution testing [23][24]. The disk diffusion assay is an easy-to-use method, where bacteria are inoculated into a film of agar medium. Filter paper disks which are impregnated with predetermined concentrations of an antibiotic are placed on top of the agar plate and the inoculated plates are incubated for 12 to 24 hours [22]. The diameter of the growth inhibited regions around the filter paper disks allows quantitative conclusions on the bacterial susceptibility. The other gold standard is broth microdilution. Here, liquid medium with different antibiotic concentrations is inoculated with the bacteria of interest and the turbidity is evaluated after 8-16 hours of incubation [24]. In addition to the long incubation times, both methods rely on time-consuming culturing of the bacteria prior to the analysis, in order to obtain sufficient numbers of bacteria for the initial inoculum [21]. Unfortunately, such long total AST durations force physicians to prescribe selective pressure inducing broad-spectrum antibiotics which, as previously described, lead to an increase in resistances [21].

In conclusion, to address the issue of antibiotic resistance, rapid detection methods with low time consumption and without the need of prior culturing techniques are required. A conceivable solution to fulfill these criteria would be the possibility to measure antimicrobial susceptibility with a high sensitivity and in very low volumes, starting with initial cell numbers of less than 100 bacteria. Furthermore, it is desirable to be able to measure bacterial mobility as an early indicator for biofilm formation, which begins with the attachment of single cells to a surface [28]. Biofilms are conglomerations of cells that are held together by a sticky extracellular polymeric matrix, in which bacteria can further increase their antibiotic resistance up to 1000-fold compared to their planktonic counterparts [26][27].

### Overview of this Work

The scope of this thesis is the analysis and development of the so called “Interference Disturbance Analysis” (IDA), a diffraction-based detection method for rapid and sensitive AST. The method utilizes coherent light diffraction at a two-dimensional grating and measures the intensity of a diffraction peak in order to draw conclusions on the amount and movement of objects located above the grating. Setup and grating parameters were designed in order to analyze the growth and mobility of bacterial ensembles in low volumes and with a small number of initial cells.

Chapter 2 gives a detailed description of the detection method as well as of the used materials and setup configurations. Furthermore, the chapter gives an introduction to the theory of the physics involved with the IDA detection method. In Chapter 3, the IDA-method is characterized with the help of transparent latex beads and a microfluidic setup, which provides a non-living model system. The results show a precise correlation between

signal intensity and number of beads. Furthermore, the analysis of short-term intensity fluctuations allows the determination of the beads' diffusion coefficient. The following Chapter 4 presents IDA measurements of bacterial cell ensembles. Here, the correlation between the cell number and the diffraction peak intensity-decrease is depicted and the doubling times of different bacterial strains are determined and confirmed with standard turbidity measurements. Moreover, a decrease in the ensemble's mobility by a factor of 3 was measured due to bacterial attachment to the surface. In Chapter 5, the IDA-method is used for antimicrobial susceptibility testing. To this end, the minimum inhibitory concentration of three different antibiotics and two different bacterial species is determined. Furthermore, rapid susceptibility testing is presented by comparing the short-term intensity fluctuations arising from a sample with and without the recommended breakpoint concentration. In Chapter 6, the IDA-method is applied for the analysis the effect of a photoswitchable antibiotic that was designed as an optical control for bacterial mobility. Chapter 7 presents an analysis of bacterial growth in very low sample volumes. For this, a custom sample holder is introduced that allows IDA measurements in sample volumes between 656 and 60 nanoliters. The sample holder is used to investigate the influence of very low sample volumes on bacterial growth and mobility. Additionally, antimicrobial susceptibility testing is performed in sample volumes of 80 nl and compared to respective measurements in conventional sample volumes of 150 µl. The final Chapter 8 summarizes the results and gives an outlook on potential future applications of the IDA-method.

# Chapter 2

# Interference Disturbance Analysis: Materials, Methods and Theory

This chapter presents the working principle of the Interference Disturbance Analysis (IDA) as well as the used materials and methods. Furthermore, an introduction to the theory of the physics involved with IDA is given. In the first section, the setup and individual components used for the IDA-method are presented. Furthermore, two different configurations of the IDA-method are described, with the first being used to calibrate and confirm the setup and the second being used for high-throughput measurements such as antibiotic concentration series. The following section presents the production of the two-dimensional (2D) grating. Thereafter, diffraction at a 2D-grating is explained with the help of the Fresnel-Huygens principle and the convolution theorem. In addition to this, the grating parameters and their influence on the IDA signal are discussed.

## 2.1 IDA-Setup

The working principle and setup of Interference Disturbance Analysis, short IDA, are discussed in this section. The fundamental physical phenomenon of IDA is diffraction at a two-dimensional gold grating which will be explained in detail in Section 2.3. As a short summary, the illumination of a 2D grating with a coherent laser leads to a diffraction intensity pattern with individual diffraction intensity peaks. The latter arise due to positive interference of elementary waves which are diffracted at the individual structures of the 2D grating (Figure 2.1). Objects of interest such as beads or bacteria that are located above the 2D grating disturb the interference of the elementary waves. This disturbance of the interference, as well as light scattering at the surface of the objects (see Section 2.3.3), lead to an attenuation of the intensity of the diffraction peaks. As a result, the growth and movement of, e.g., bacteria above the grating lead to long- and short-term intensity fluctuations of the diffraction peaks (Figure 2.1). For the IDA-method, the intensity of a first-order diffraction peak is measured with a CMOS camera. The time course of the diffraction peak intensity in turn allows conclusion on parameters such as number, velocity, growth rates and mobility of the objects above the grating. The precise

correlation between these parameters and the diffraction peak intensity is described for beads and bacteria in Chapters 3 and 4, respectively.

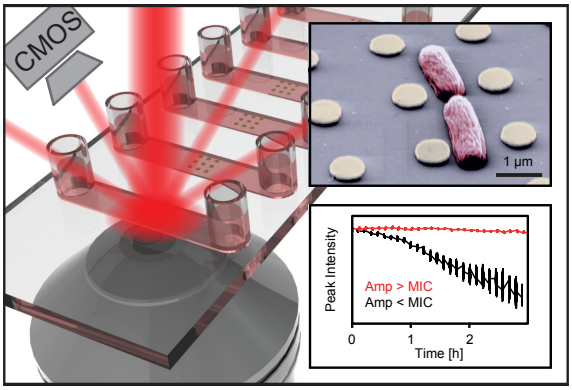


Figure 2.1: **Interference disturbance analysis (IDA).** The IDA method makes use of diffraction at a 2D grating. As shown in the left half, a 2D grating (which is here placed inside a sample container) is illuminated with a coherent laser. As a result of constructive interference of elementary waves, which form at the individual grating structures, diffraction intensity peaks arise. The intensity of such a diffraction peak is recorded over time. When bacteria grow above the grating (upper right inset), the interfering elementary waves are disturbed, which leads to long- and short-term intensity fluctuations of the diffraction peaks. These intensity fluctuations allow conclusions on the growth and mobility of the bacteria and thus enable, e.g., the determination of the minimum inhibitory concentration (MIC) of an antibiotic such as ampicillin (Amp, lower right inset).

### Laser

As an illumination source, an *Ultra Low Noise (ULN) Diode Laser* from *Coherent* was used for the IDA-setup. This laser has a power of 5 mW, a wavelength in the red spectrum ($\lambda = 635 + 7 - 2\,\text{nm}$) and a beam diameter of 1 mm with low divergence [29]. As the name implies, it has a very low RMS-noise of $< 0.06\%$ for bandwidths from 10 Hz to 10 MHz. The low noise is accomplished by forcing the laser into a multi-longitudinal mode. As a further result, mode hopping due to temperature changes is suppressed. A custom designed laser holder was manufactured by the LMU workshop for adjustable alignment, passive heat dissipation and mechanical stability of the laser.

### CMOS-sensor

For the acquisition of the diffraction peak intensity, the UI-1541LE-M monochromatic CMOS-sensor from IDS was used. The sensor chip consists of 1280 x 1024 pixels with a pixel size of 5.2 µm, resulting in an optical area of 6.656 x 5.325 $\text{mm}^2$. The comparatively large pixel size leads to a low signal-to-noise ratio which in turn allows a higher sensitivity of the IDA-method. The gray value depth is 8 bits and thus corresponds to 256

possible pixel values. The CMOS-sensor allows a maximum acquisition rate of 25 frames per second, which was necessary for a high temporal correlation of the diffraction peak intensity and the position of 3 µm sized latex beads, as described in Chapter 3.3. In order to avoid scattered light which can lead to false or noisy diffraction peak intensity signals, an aluminum tube was placed in front of the sensor. A CMOS-sensor was used for intensity acquisition over a photo diode, as it allowed to track the diffraction peak and thus compensate for small setup instabilities arising from, e.g., temperature gradients.

### 2.1.1 Microscope-Configuration for Correlation

Two different configurations of the IDA-method were used in this thesis and are described in detail in the following two subsections. The aim of the microscope-configuration was the correlation of the IDA signal and the real space by simultaneously acquiring the diffraction peak intensity and microscopy images. For this, the IDA-setup was implemented into a *Nikon TI-E Eclipse* inverted microscope. Because the amount and movement of the objects (beads or bacteria) relative to the grating are important for the correlation, it was necessary to have both the objects and the grating in the same focal plane. This was achieved by using *Ibidi sticky-Slide VI 0.4* sample containers, which allow the attachment of a custom coverslip as a container bottom. To this end, the 2D grating was nanolithographed on a borosilicate glass coverslip (Section 2.2), which was subsequently attached to the sticky-Slide sample container. As a result, IDA measurements with the 2D grating inside the sample chamber could be conducted and simultaneously imaged with a 60x magnification objective (Figure 2.2a). A photograph of the IDA microscope-configuration is presented in Figure 2.2b. The laser beam is redirected by a mirror and positioned onto the sample with the nanolithographed 2D grating, resulting in a diffraction pattern (only the 1st order is shown in Figure 2.2b). The latter is acquired with the CMOS-sensor. For this configuration, an additional shutter was placed in front of the laser and the microscope illumination in order to synchronize the diffraction peak intensity and the microscopy images.

### 2.1.2 Scanning-Configuration for High-Throughput

A disadvantage of having the 2D grating inside the sample chamber is that it is hardly possible to clean the chamber and thus reuse a diffraction grating. However, the production of a grating is time-consuming and the need of a new grating for each samples makes high-throughput measurements such as antibiotic concentration series difficult. For this reason, a scanning-configuration of the IDA-setup was designed in order to enable high-throughput measurements. In this configuration, the grating is placed outside of the chamber but in close proximity to the sample container (Figure 2.3a). Thus, a single grating can be used for a theoretically infinite amount of measurements. Additional advantages of this configuration are low preparation times and the possibility to measure

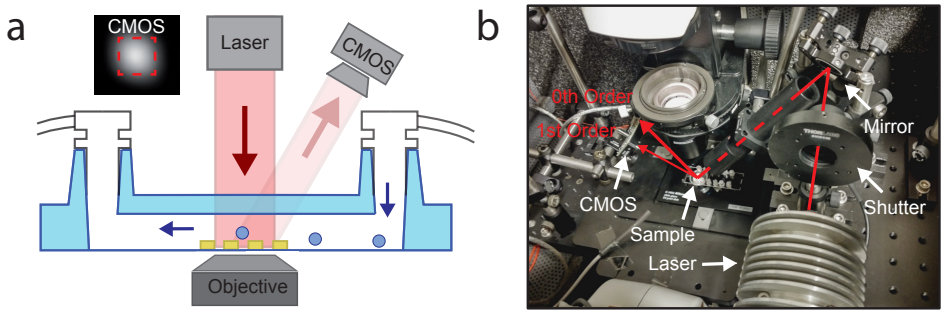


Figure 2.2: **Microscope-configuration of the IDA-setup. a)** Side view of the IDA microscope-configuration. The gold grating (yellow) is lithographed onto a glass coverslip, which in turn is attached to a bottomless sample container. Thus, the grating and the objects of interest (here: 3 µm sized latex beads) are in the same focal plane and allow the correlation of the IDA signal with the real space. The microfluidics indicated by the blue arrows were used to move the latex beads and were not employed for bacterial measurements. **b)** Photograph of the microscope-configuration. The laser beam passes the shutter, which is used to synchronize the intensity and microscopy acquisition, and is redirected onto the sample by a mirror. Here, the coherent laser beam is diffracted at the 2D grating and the intensity of a 1st order diffraction peak is acquired with a CMOS-sensor. Reproduced in part with permission from Nano Letters, in press. Copyright 2018 American Chemical Society.

with standard plastic lab ware. A *Prior Scientific* high precision xyz-scanning stage was used to switch between the individual samples (Figure 2.3b). The xy-component of the scanning stage (*XY flat top stage H101, Prior*) allows lateral travel of 117 x 77 mm with a minimum resolution of 0.2 µm and a repeatability of 0.7 µm over the full travel range. For measurements with *Ibidi µ-Slide VI 0.4* sample containers (compare Figure 2.3a), six samples could be measured simultaneously. Within the scope of this thesis, the scanning-configuration was improved in order to measure up to 256 samples simultaneously, as will be discussed in Chapters 6 and 7. To guarantee optimal growth conditions for the bacteria, the scanning-configuration was placed inside an incubator which was set to 37°C (Figure 2.3b).

## 2.2 Grating Production

The following section gives a brief explanation on how the 2D-grating used in the IDA-setup is fabricated. Depending on the application, two different substrates were used. For measurements with the microscope-configuration (Section 2.1.1), which is used to calibrate and demonstrate the working principle of the IDA-method by correlating the diffraction-signal to microscope images, a transparent substrate in form of borosilicate glass was used. During measurements with the scanning-setup (Section 2.1.2) a non-transparent silicon (Si) substrate was used in order to avoid scattered light and receive

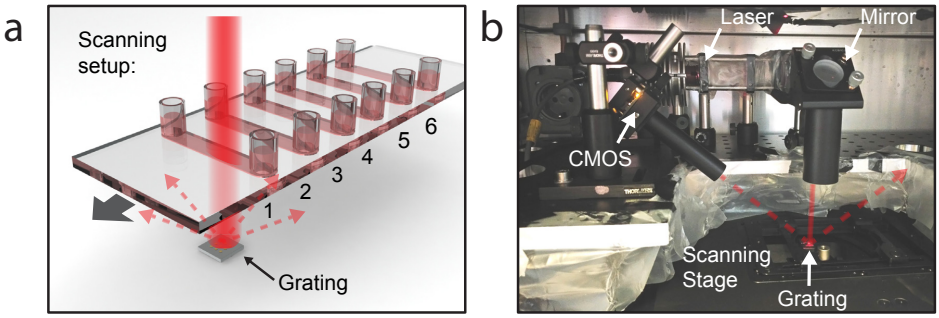


Figure 2.3: **Scanning-configuration for high-throughput measurements. a)** In this configuration, the gold-grating is placed outside of the probing chamber. This allows to scan through multiple samples, as indicated for a sample container with six probing chambers. **b)** Photograph of the IDA scanning-configuration placed inside an incubator. A mirror redirects the laser beam onto the 2D grating which is fixed underneath the mirror. A scanning stage is used to position multiple samples sequentially above the grating. The parafilm seen in the photograph was used to protect the laser beam from air turbulences induced by the incubator's ventilation system. Reproduced in part with permission from Nano Letters, in press. Copyright 2018 American Chemical Society.

a slightly better signal to noise ratio. In the following, the fabrication of a grating on a silicon substrate is explained. The fabrication on a glass substrate requires an additional step which is discussed at the end. The gratings used in this PhD-thesis were fabricated in the clean room of the chair of J. Kotthaus at the LMU Munich.

### Silicon Substrate

In the first step, a 5 x 5 mm silicon chip is taken from a wafer and is cleaned in a petri dish with DMSO inside an ultrasonic cleaner (Figure 2.4a). This is necessary in order to remove a protective lacquer and receive a dust-free and smooth surface. In the next step, the chip is spin-coated with the positive-photo resist polymethyl methacrylate (PMMA, Figure 2.4b). Thereafter, the chip is illuminated by electron beam lithography (*eLine plus, Raith*). In this step, the precise measurements of the grating such as structure width, periodicity and amount of structures can be programmed in the lithography software and are then imprinted on the photo resist (Figure 2.4c). Depending on the scientific question, different parameters were used during the measurements shown in this thesis. However, the diameter of the circular structures is, if not stated otherwise, 800 nm and the periodicity is 2 µm. The amount of structures is stated for the individual IDA configurations in the discussion of the grating parameters in Section 2.3. After electron beam lithography, the photo resist is developed, leading to the dissolution of illuminated photo resist (Figure 2.4d). This sets the illuminated areas of the substrate free, while leaving the unilluminated areas covered with photo resist. In the next step, 3 nm of titanium followed by 60 nm of gold are evaporated onto the chip in an ultrahigh vacuum evaporation

machine (Figure 2.4e). Titanium is used as an adhesion agent and gold was chosen due to its bio-compatibility [30] and high reflectivity [31]. The final step is the lift off of the photo resist (Figure 2.4f). During this step, the chip is put inside a petri dish filled with DMSO which in turn is placed on top of a 75°C hot heating plate for two hours. After the photo resist is removed, merely the gold grating remains on top of the substrate and the chip is ready for application in an IDA-setup.

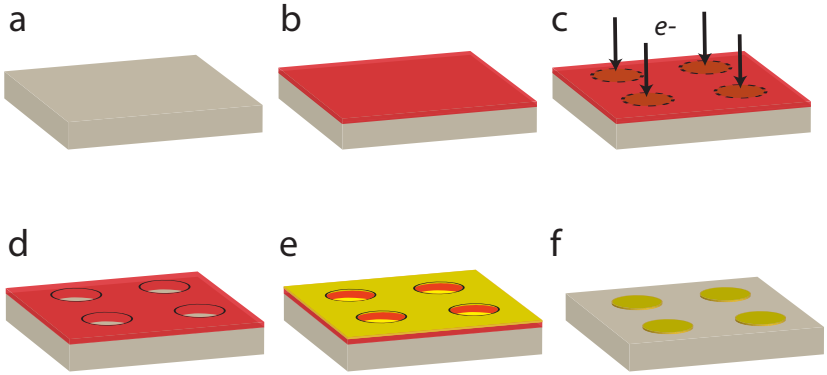


Figure 2.4: **Sample fabrication using electron-beam lithography. a)** Clean silicon substrate. **b)** The photo resist PMMA is spin-coated onto the substrate. **c)** Electron beam lithography allows precise illumination of the substrate with the desired grating parameters. **d)** Development of the photo resist leads to dissolution of the illuminated section. **e)** Evaporation of 3 nm titanium and 60 nm gold. **f)** Finished sample after DMSO lift-off. Image adapted from [32].

### Silicon Dioxide Substrate

The fabrication of a grating on a borosilicate glass substrate is very similar to as shown for a silicon substrate. Since glass is non-conductive, it is required to evaporate an additional layer of chrome before the electron beam lithography step. The conductive chrome layer reduces surface charging due to secondary electron emission during lithography. After electron beam illumination, the chrome layer is removed by chrome etching.

## 2.3 Diffraction

The IDA-method is based on diffraction at a two-dimensional grating. This underlying phenomenon is explained and derived in this section with the help of the Huygen's principle and the convolution theorem. After a derivation of the intensity distribution for a 2D grating, a discussion of the grating parameters and their influence on the IDA signal is given.

### 2.3.1 The Fresnel-Huygens Principle

In 1690 Christiaan Huygens released his work *Trait de la Lumire*, engl. treatise on light, in which he proposes, that every point of a primary wavefront is the origin of a secondary, spherical elementary wave. The wavefront at a later time point is the envelope of the secondary elementary waves (Figure 2.5a, right side of the slit). The secondary waves propagate with the same frequency $\nu$ and velocity v as the primary wave [33]. This statement is known as the Huygens Principle and was later extended to the Fresnel-Huygens principle by the French physicist Augustin-Jean Fresnel, who added that at every subsequent point, the amplitude of the optical field is given by the superposition of all elementary waves under consideration of their amplitude and relative phase [33]. By considering interference in the Fresnel-Huygens Principle, it was suitable to describe diffraction phenomena known from single- and double-slit experiments. When a plane wave impinges on a slit, the resulting superimposed wave propagates not only in the unobstructed but also in the shadowed region (Figure 2.5a). If the slit is of similar size as the wavelength or smaller, the superimposed wave will propagate circularly and at large angles in to the region beyond the obstruction [33].

When coherent light impinges on a double slit, the elementary waves originating from each slit interfere with each other (Figure 2.5b), resulting in intensity maxima and minima in the far field (Figure 2.5c). The difference in the optical path length $\Delta s$ between the elementary waves originating from each slit is given as $\Delta s = d \cdot \sin(\alpha)$ (Figure 2.5b). For normally incident light, interference maxima occur at angles $\alpha$ for which the difference in optical path length is equal to an integer multiple of the wavelength, i.e., the condition $\Delta s_{max} = d \cdot \sin(\alpha_n) = n \cdot \lambda$ with $n \in \mathbb{N}$ is fulfilled. If the light incides with an angle $\alpha_i$, the equation is slightly altered to $d \cdot (\sin(\alpha_i) - \sin(\alpha_n)) = n \cdot \lambda$.

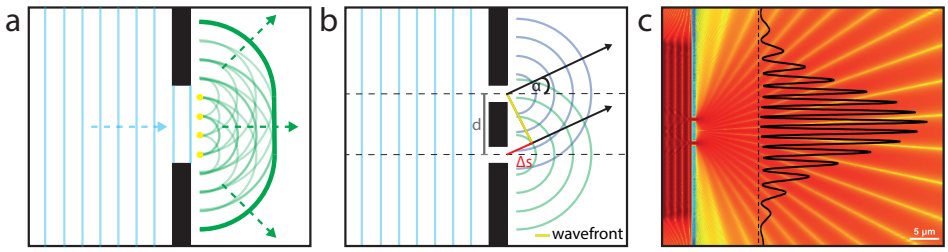


Figure 2.5: **Fresnel-Huygens principle and diffraction at a double slit. a)** Demonstration of the Fresnel-Huygens principle at a single slit. Four exemplary elementary waves originating at the yellow points are shown in transparent green. The resulting superposition of the elementary waves is depicted as a bold green wavefront. **b)** Diffraction at a double slit. The wavefront for the condition $\Delta s_{max} = d \cdot \sin(\alpha) = \lambda$, which results in an intensity maximum, is depicted in yellow. **c)** Finite-difference time-domain simulation of an interference pattern for a two-slit diffraction experiment. The black line shows the intensity profile at the dashed line. Image **c** taken from [34].

### 2.3.2 Convolution Theorem

The electromagnetic field distribution $E(k_x, k_y)$ of light that is diffracted at a given structure can be described analytically by the Fourier transform (FT) of the structure's aperture function [35]. For periodic structures, the electromagnetic field distribution can be calculated with the help of the convolution theorem. The latter states that the Fourier transformation of the convolution of two functions is equal to the product of their Fourier transforms. For a double slit, the aperture function g(x′) can be described as a convolution of a rectangle function f(x′) with two $\delta$-functions h(x′):

$$g(x') = f(x') \otimes h(x') = \int_{-\infty}^{\infty} f(x)h(x' - x)\mathrm{d}x. \tag{2.1}$$

According to the convolution theorem, the Fourier transform of g(x′) is given as:

$$FT\{g\} = FT\{f \otimes h\} = FT\{f\} \cdot FT\{h\} \equiv G(k). \tag{2.2}$$

The plot of the functions g(x′), f(x′), h(x′) and their respective Fourier transforms is presented in Figure 2.6. The resulting Fourier transform of the aperture function g(x′) describes the electromagnetic field distribution $E(k_x)$, which can be used to calculate the intensity distribution $I(k) = |E(k)|^2$ [35][36].

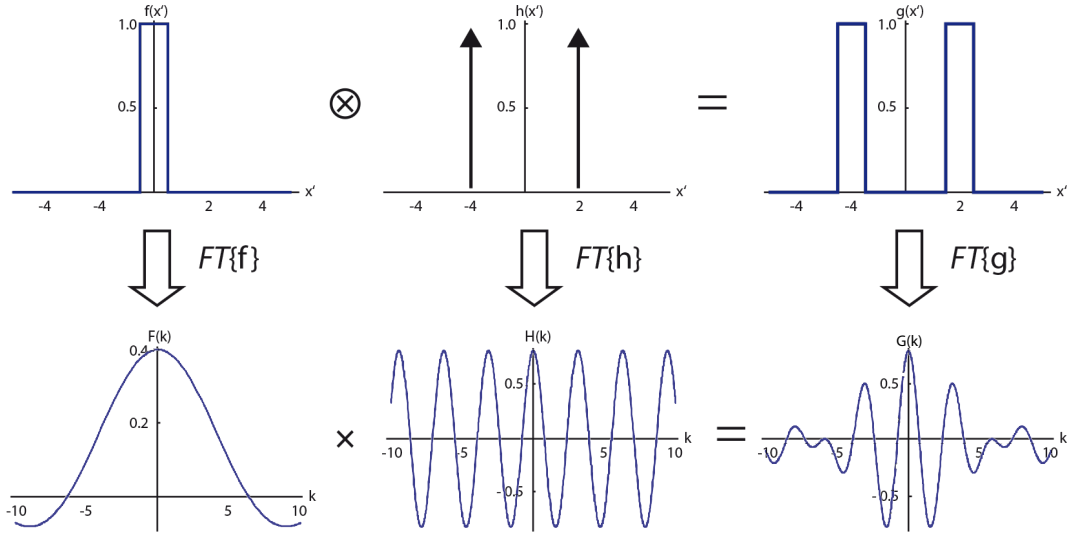


Figure 2.6: **Convolution theorem applied to a double slit.** The upper row shows a rectangle function f(x′) and two $\delta$-functions described by h(x′), as well as the convolution of both functions, resulting in g(x′). The latter describes the aperture function of a double slit. The lower row shows the respective Fourier transform of the upper function. The product of FT{f} and FT{h} results in the Fourier transform of the double slit aperture function, i.e. FT{g}. Image adapted from [34].

### 2.3.3 Diffraction at a Two-Dimensional Grating

The IDA-method presented in this thesis utilizes diffraction at a two-dimensional grating of spherical gold nanostructures. In order to calculate the electromagnetic field distribution $E(k_x, k_y)$ and the respective intensity distribution $I(k_x, k_y)$, the convolution theorem is applied to a two-dimensional grating in the following. The aperture function $a(x', y')$ of a two-dimensional grating with a periodicity p of M structures in x-direction and N structures in y-direction with a diameter d each can be described by a convolution of a quadratic lattice of $\delta$-functions and a circular disk function $a_e(x', y')$:

$$\begin{aligned} a(x', y') &= a_e(x', y') \otimes p^2 \sum_{m=1}^{M} \delta(x' - mp) \sum_{n=1}^{N} \delta(y - np) \\ with\ a_e(x', y') &= \begin{cases} 1\ for\ x'^2 + y'^2 = (\frac{d}{2})^2 \\ 0\ otherwise \end{cases} . \end{aligned} \tag{2.3}$$

The corresponding Fourier transform is:

$$\begin{aligned} FT\{a(x', y')\} = E(k_x, k_y) &= p^2 A_e(k_x, k_y) \sum_{m=1}^{M} e^{-ik_x mp} \sum_{n=1}^{N} e^{-ik_y np} \\ &= p^2 A_e(k_x, k_y) \sum_{m=1}^{M} e^{-ik_x x_m} \sum_{n=1}^{N} e^{-ik_y y_n}, \end{aligned} \tag{2.4}$$

with $x_m \equiv mp$, $y_n \equiv np$, $k_x = \frac{2\pi}{\lambda}\frac{x'}{r}$, $k_y = \frac{2\pi}{\lambda}\frac{y'}{r}$ and $A_e(k_x, k_y)$ being the Fourier transform of the circular disk aperture function (Bessel function) [37], r the distance between the grating and the screen and $\lambda$ the wavelength of the coherent light. A detailed derivation of the aperture function and its Fourier transformation can be found in [34].

The diffraction intensity distribution, which is proportional to the squared modulus of the electromagnetic field distribution, is given as:

$$I(k_x, k_y) \propto \left| p^2 A_e(k_x, k_y) \sum_{m=1}^{M} e^{-ik_x x_m} \sum_{n=1}^{N} e^{-ik_y y_n} \right|^2. \tag{2.5}$$

#### Disturbance by beads and bacteria

When small objects such as beads or bacteria are introduced in the light path, the intensity of the diffraction pattern is disturbed. The disturbance has three different reasons: Firstly, light is scattered at surfaces of two objects with different refractive indices, such as the transition between a bacterium and the surrounding medium. Secondly, the objects absorb light which also leads to a decrease of intensity. For low concentrations of beads or bacteria, the named two effects can be combined and described by *Lambert-Beer's*

*law* [38]. Due to the absorption and scattering, the electric field amplitude is multiplied by a time-dependent attenuation factor $E_{m,n}(t) \leq 1$. The third disturbance reason also arises from the difference in refractive index between the bacterium and the surrounding medium ($\Delta n = n_{med} - n_{bac} \neq 0$). Due to this, light that passes through a bacterium before it hits the grating has a different optical path length than light that directly hits the grating. This can be described by a phase shift $\delta_{m,n}(t)$ of the electromagnetic field, which is time-dependent and only non-zero for grating structures covered by bacteria. This leads to a disturbance of the positive interference of the individual elementary waves and results in a decrease of diffraction peak intensity. With both attenuation terms, the intensity distribution can be calculated as:

$$I(k_x, k_y) \propto \left| \sum_{m=1}^{M} \sum_{n=1}^{N} E_{m,n}(t) e^{i\delta_{m,n}(t)} e^{-i(k_x x_m + k_y y_n)} \right|^2. \tag{2.6}$$

### 2.3.4 Discussion of the Grating Parameters

In the following, the grating parameters used for the IDA measurements presented in this thesis are discussed and motivated. As can be seen from Equation 2.5, the intensity distribution is dependent on the wavelength $\lambda$, the amount of circular gold structures M x N, the periodicity p and the Bessel function, which again is non-linearly dependent on the diameter d. A further relevant parameter of the grating is the height of the gold structures, which was set to 60 nm in order to not influence the bacteria, while obtaining a sufficiently high reflectivity (>90%). In order to correlate the IDA signal to the real space, microscopy images were acquired simultaneously to the diffraction peak intensity with the microscope-configuration described in Section 2.1. The periodicity p = 2 µm and diameter d = 0.8 µm were chosen to yield a good compromise between the simultaneous IDA-signal and microscopy image acquisition and the mobility analysis, which will be described in more detail in Chapter 3. Here, a smaller periodicity with a bigger diameter of the structures allows for a higher spatial resolution of bacterial movement. However, it should still be possible to see and evaluate the bacteria (approx. 1 x 2 µm$^2$) with the microscope-configuration (Figure 2.7).

As can be seen in Equation 2.5, a bigger number of structures leads to a higher signal and to a higher statistical relevance due to a higher amount of simultaneously evaluated bacteria. However, a larger grating also results in a smaller sensitivity of bacteria due to the constructive interference amount of each single gold structure. For the microscope-configuration, the number of circular gold-structures M x N was set to 30 x 30 (60 x 60 µm$^2$), as this size would still allow growth measurements starting from single bacteria (see Chapter 4) with a good signal-to-noise ratio, while simultaneously enabling growth measurements over two orders of magnitude. For the scanning-configuration, 60 x 60 structures were used in order to achieve a higher comparability between different IDA measurements with low bacterial starting concentrations.

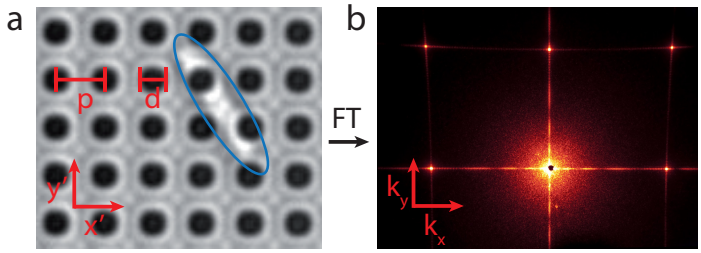


Figure 2.7: **Discussion of the IDA grating parameters. a)** Cutout from a transmission bright-field microscope image with a two-dimensional gold-grating (black circles) and one bacterium on top of it (indicated with a blue outline). The bars show the grating parameters periodicity p = 2 µm and diameter d = 0.8 µm, which were used for IDA measurements in this thesis. **b)** Exemplary photograph of the diffraction intensity distribution from a red laser beam diffracted at a 2D dimensional grating. Image **b** taken from [34]. Reproduced in part with permission from Nano Letters, in press. Copyright 2018 American Chemical Society.

# Chapter 3

# Characterization with Transparent Latex-Beads

In this chapter, the working principle of the IDA-setup is presented and analyzed with the help of transparent latex-beads as a well-defined, non-living model system. To be able to achieve comparable and reproducible results, the 3 µm-sized latex-beads were diluted, such that small numbers of beads could be moved across the grating at a time with a microfluidic setup as described in Section 3.1. The simultaneous recording of the amount of beads and the IDA-signal showed a strong correlation, as exemplarily shown in Figure 3.1. A detailed, quantitative analysis of the individual events of beads crossing the grating is given in Section 3.2. With the help of the microscope-configuration (Section 2.1.1), the exact correlation between the bead's position within a unit-cell of the grating and the resulting diffraction peak intensity-decrease could be determined and is presented in Section 3.3. Based on the position-dependent intensity-decrease, a continuous model was established that correlates the diffusion coefficient of the beads to short-time intensity fluctuations of the IDA-method. The model described in Section 3.4 can further be transferred to bacterial measurements, which will be discussed in Chapter 4.

## 3.1 Microfluidic Setup

In order to evaluate the influence of an interference-disturbing particle on the diffraction-peak intensity, 3 µm-sized transparent latex-beads were used as a non-living model system due to their consistent and symmetric shape as well as the ease of tracking their position [39]. To manipulate their position and movement, a microfluidic setup with a pump was used (Landgraf Laborsysteme, model LA100). For the measurements discussed in this chapter, 3 µm-sized latex-beads from Sysmex-Partec were used and diluted in order to obtain bead-densities that would allow the analysis of single-beads. After dilution, the beads were given inside a probing well of an *Ibidi sticky-slide µ-well VI 0.4* attached to a customized, transparent glass-bottom with an electron-beam lithographed gold-grating on the inside of the probing chamber. The latter allows the simultaneous analysis of the beads' position on top of the grating and the respective diffraction peak intensity-

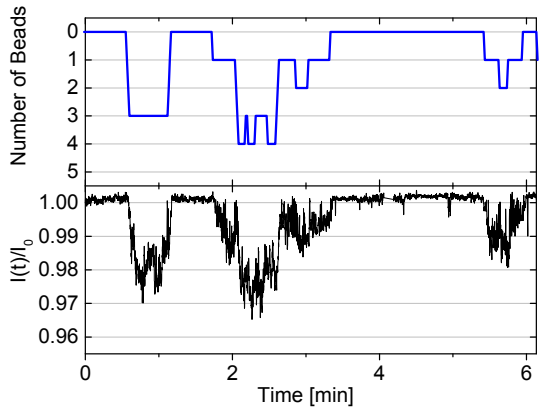


Figure 3.1: **Simultaneously acquired number of beads and normalized diffraction-peak intensity.** Dynamic correlation of the bead amount and normalized diffraction peak intensity for several crossing events of one to four beads. The data shows a strong correlation between the two measured values. Reproduced with permission from Nano Letters, in press. Copyright 2018 American Chemical Society.

decrease, since the beads and the grating are thus in the same focal-plane. The grating parameters used in this chapter are 30 x 30 gold structures with a periodicity p = 2 µm, diameter d = 800 nm and height h = 60 nm. The application of different flow-velocities allowed the analysis of the correlation between bead velocity and short-term intensity fluctuations.

## 3.2 IDA of Transparent Latex-Beads: Results

The microfluidic-setup described in the previous section allows the analysis of the influence of a single or multiple beads and their disturbance of the interfering elementary waves on the diffraction-peak intensity. Microscope images of one to four beads on top of the grating are presented in Figure 3.2a. The trajectory of a single bead crossing the grating due to the microfluidic-flow is here depicted by a red line. The corresponding normalized diffraction-peak intensity to the single-beads crossing is shown in Figure 3.2b. The average diffaction-peak intensity during the crossing of the bead is marked as mean normalized intensity (MNI, red line). The results show that as soon as the bead reaches the gold grating, the diffraction-peak intensity immediately decreases by approx. $0.54 \pm 0.07\%$ in MNI. The time-points at which the bead enters and exits the area of the grating are marked by $t_1$ resp. $t_2$. During the bead's crossing of the grating, short-term intensity fluctuations can be seen. The amount of short-term fluctuations, i.e. intensity maxima resp. minima, between $t_1$ and $t_2$ is with a total number of 30 equivalent to the amount of unit-cells passed by the bead. This observation hints at a direct connection between the bead's position inside an unit-cell of the grating, i.e. the quadratic space in between four adjacent gold structures (2 x 2 µm$^2$), and the intensity fluctuations and will be discussed

in more detail in the following section. Parts of the work presented in this section were a collaboration with Konstantin Ditzel within the scope of his bachelor thesis [39].

In addition to the single beads, the effect of interference disturbance by multiple beads was analyzed. Figure 3.2c shows exemplary normalized diffraction-peak intensities for one to four beads (I-IV). The inset shows averaged mean normalized intensities of crossing events for one bead (eleven events), two beads (six events), three beads (two events) and four beads (three events). The results show that a linear increase in the number of beads leads to a linear decrease of diffraction-peak intensity, with a fit of MNI[%](x) = 100.0 - 0.43·x (red line).

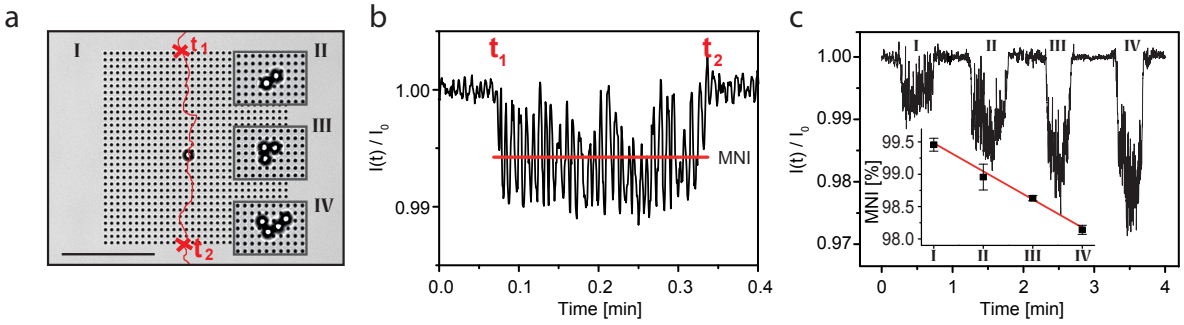


Figure 3.2: **Interfernce disturbance analysis of 3 µm-sized latex-beads. a)** Microscope images of one to four beads on top of the grating (I-IV). The red line marks the trajectory of the bead crossing the grating. The red crosses $t_1$ and $t_2$ mark the entrance and exit of the bead's crossing. The scale bar is 30 µm. **b)** Normalized diffraction-peak intensity of the single bead crossing shown in a). The time-points $t_1$ and $t_2$ show the beginning and ending of the traversal. The mean normalized intensity (MNI) of approx. 0.995 during the crossing is marked with a red line. **c)** Exemplary normalized diffraction-peak intensities for crossings of one to four beads (I-IV). The inset shows the averaged MNI values for in total 22 crossing events with a linear fit of MNI[%](x) = 100.0 - 0.43·x (red line). Reproduced (modified) with permission from Nano Letters, in press. Copyright 2018 American Chemical Society.

## 3.3 Position-Dependent Intensity Decrease

It was shown in the previous section that the amount of short-term intensity fluctuations in Figure 3.2b is equal to the amount of unit-cells of the gold grating which the bead traverses during the same time. The latter suggests that the diffraction peak intensity varies depending on the precise position of the bead within an unit-cell of the grating. In order to validate and analyze this, the Orca-05G digital CCD camera (Hamamatsu) from the microscope-configuration 2.1.1 was replaced by an Andor Zyla CMOS camera

that allows acquisition rates of 25 frames per second with a resolution of 1392 x 1040 pixels. The intensity of the diffraction peak was recorded accordingly with 25 frames per second as well. Additionally, two shutters were added to the setup: one in front of the laser and one in front of the microscope-camera. By closing and opening both shutters simultaneously once before and once after a measurement, the microscope images could be synchronized with the diffraction-peak intensity acquisition. During the measurements, the focus plane was kept in place with a perfect focus system.

The determination of the bead's precise position within a unit-cell was done by image analysis using OpenCV and with the help of Valentin Stierle (Figure 3.3). The image analysis was done in several steps. In the first step, the area of the circular gold structures is determined by applying a threshold (Figure 3.3b, cyan outlines). Thereafter, the center of mass of each individual gold structure is evaluated (Figure 3.3b, cyan crosses). To make sure that all gold structures are captured and no errors due to beads occurred, the median of three images at different time points, i.e. the beginning, the middle and the end of the passing event, was used. Such a median image yields the grating without a bead on top. In the next step, the difference between the median image and the regular image with bead is calculated (Figure 3.3c). A threshold is applied to the result, yielding the yellow outline in Figure 3.3c. The whole area of the bead is then determined using openCVs minimum enclosing circle function (red outline in Figure 3.3c) and the center of mass is calculated (green cross in Figure 3.3c). Locating the bead's center of mass in each frame allows to reconstruct its trace and precise position within each unit cell (Figure 3.3d). The position can then be correlated to the diffraction-peak intensity as shown in Figure 3.3e. When the resulting data-points of each unit-cell, i.e. the squares enclosed by cyan dotted-lines in Figure 3.3e, are combined, a map of the correlation between the diffraction-peak intensity and the bead's position within a unit-cell arises as a result (Figure 3.3f). This analysis thus has shown that the diffraction peak intensity is position-dependent and that intensity fluctuations of approx. 1% occur due to positional changes of the bead smaller than the periodicity of the grating.

Since the intensity fluctuations are dependent on the bead's position, it should be possible to draw conclusions on the mobility of the respective disturbing bead by analyzing the intensity fluctuations temporally. To probe this, single beads were moved across the grating with two different flow velocities, i.e. 0.01 ml/min resulting in an average bead velocity of 1.98 µm/s (Figure 3.4a) and 0.02 ml/min with an average bead velocity of 4.72 µm/s (Figure 3.4b). The average bead velocities were evaluated from the microscope images. In addition to this, a single bead was positioned above the grating, whereupon the microfluidic flow was stopped, leading to a random movement of the bead due to Brownian motion (Figure 3.4c). The respective intensity fluctuations of the passing events were Fourier transformed, yielding a peak for each of the two different flow velocities as well as a decay for the bead moving due to Brownian motion (Figure 3.4d). A Gaussian peak was fitted to each Fourier amplitude spectrum of the constant flow velocities, resulting in a peak position of 0.97 Hz for 0.01 ml/min (red line, Figure 3.4d) and of 2.32 Hz for

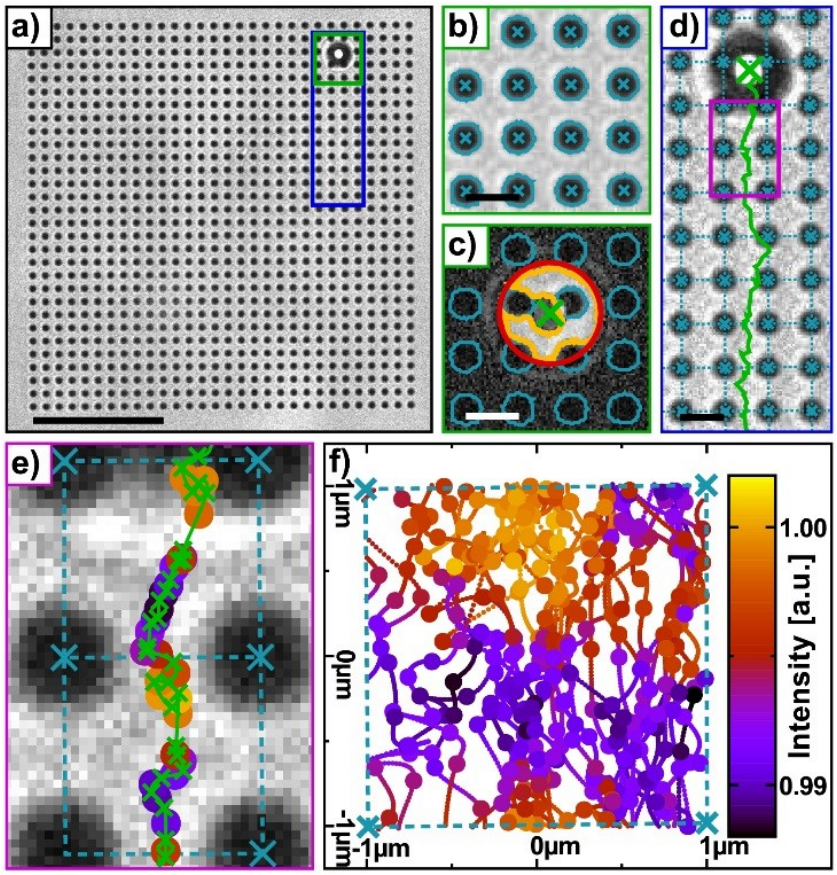


Figure 3.3: **Correlation of the bead's position and the diffraction peak intensity.** **a)** Microscope image of a 60 x 60 µm$^2$-sized grating with 30 x 30 circular gold structures with a single bead on top. The scale bar is 20 µm. **b)** Segment of the grating marked with a green square in panel **a** without a bead. The cyan circles mark the outlines of the gold structures and the cyan crosses the respective centers of mass. **c)** Same section as in panel **b**, showing the difference between an image with and without a bead. The yellow outline marks the thresholded image and the red circle the minimum enclosing circle. The green cross marks the bead's center of mass. **d)** Section marked as a blue rectangle in panel **a**. The green line depicts the determined trace of the bead. **e)** Correlation between the bead's position (green crosses) and the diffraction peak intensity (color-coded circles) of the section marked purple in panel **d**. The dotted cyan squares mark two unit-cells. **f)** Combination of the correlated data of a single-bead's trace in one unit-cell. The thicker dots show the measured position and the thin splines the interpolation between two bold dots. Reproduced with permission from Nano Letters, in press. Copyright 2018 American Chemical Society.

0.02 ml/min (blue line, Figure 3.4d). In order to compare the positions of the peaks to the actual bead velocities, the amount of 'passed unit-cells per second' is multiplied with the periodicity of the grating, i.e. 2 µm. The latter results in determined bead velocities of 1.94 µm/s for the slower velocity (0.01 ml/min) and 4.64 µm/s for the faster velocity (0.02 ml/min). Both results are in good agreement with the velocity determined from the microscope analysis of 1.98 µm/s for the slower and 4.72 µm/s for the faster velocity. These results thus verify the capability to determine the velocity of linearly moving beads from short-term intensity fluctuations. The Fourier spectrum of the Brownian motion movement was fitted by an exponential decay function and is discussed in more detail in Section 3.4. As a reference, the Fourier spectrum of the background noise without a bead on top of the grating is shown in Figure 3.4d as a green line.

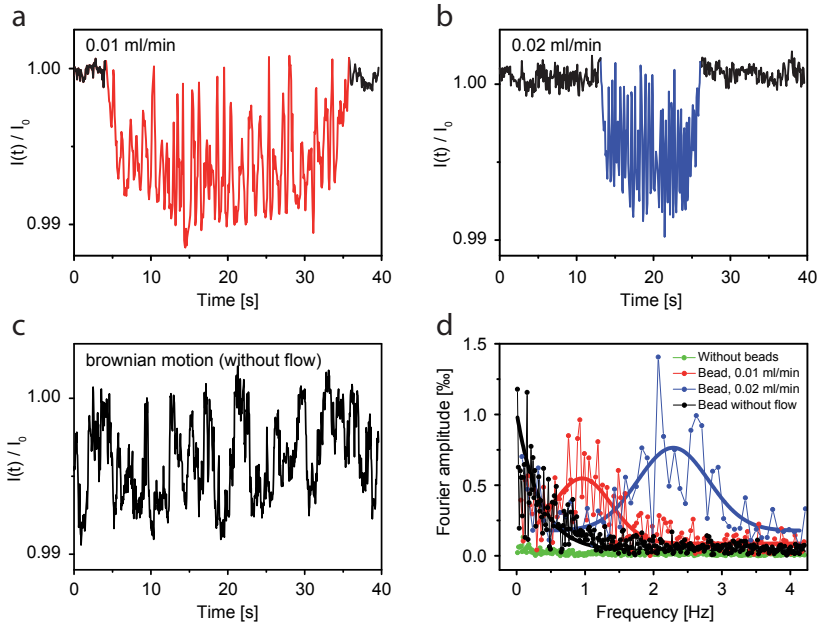


Figure 3.4: **Intensity fluctuations due to different bead velocities and their respective Fourier transformation. a)** Short-term intensity fluctuations induced by a moving latex-bead with a flow-velocity of 0.01 ml/min. **b)** Analogous short-term intensity fluctuations for a flow-velocity of 0.02 ml/min. **c)** Short-term intensity fluctuations induced by a latex-bead moving due to Brownian motion. **d)** Fourier spectra from the fluctuations shown in **a** (red), **b** (blue), **c** (black) and from background fluctuations without a bead on top of the grating, but with a flow of 0.02 ml/min. The points connected by thin lines show the data and the bold lines show the respective fit. A Gaussian fit yields a peak at 0.97 Hz and 2.32 Hz for the constant flow velocities of 0.01 ml/min (red) and 0.02 ml/min (blue), respectively. The Fourier spectrum arising from Brownian motion was fitted by an exponential decay, which is discussed in more detail in Section 3.4. Reproduced in part with permission from Nano Letters, in press. Copyright 2018 American Chemical Society.

Having shown that the diffraction peak intensity-decrease is position-dependent (Figure 3.3f), the smallest resolvable changes of a bead's position is determined in the following. To obtain a derivable function, the mapping of the position-dependent intensity-decrease presented in Figure 3.3f was fitted by a polynomial function of 25th order (Figure 3.5a) using Wolfram Mathematica. Subsequently, the gradient field of the polynomial function is calculated. The absolute value of the gradient field is shown in Figure 3.5b. A line profile of the region with the highest absolute gradient is shown in Figure 3.5c for the polynomial fit and in Figure 3.5d for the respective absolute of the gradient field.

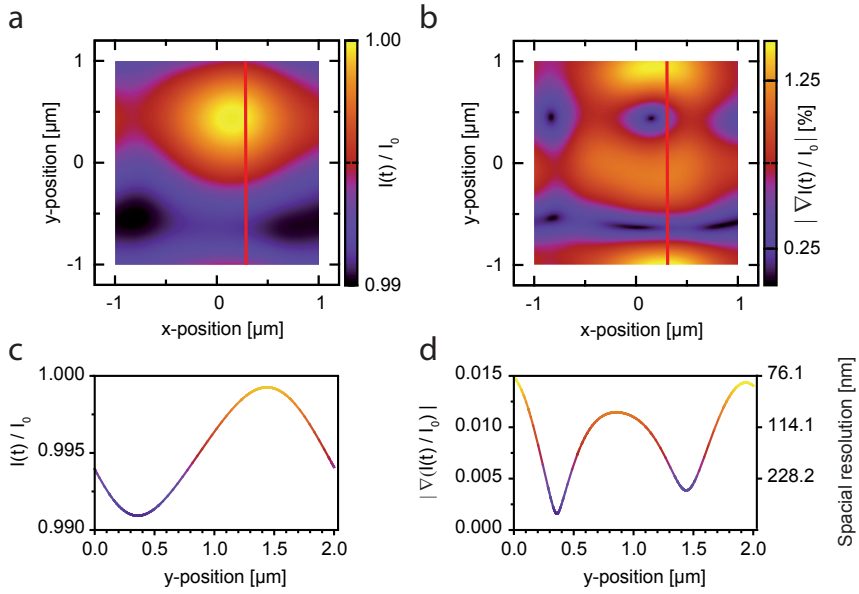


Figure 3.5: **Spatial resolution of changes in a bead's position. a)** Polynomial fit of 25th order to the position-dependent intensity-decrease shown in Figure 3.3f. **b)** Absolute of the gradient field calculated from the fitted polynomial shown in panel **a**. **c)** Line profile of the normalized diffraction peak intensity for the section with the steepest gradient, also depicted as a red line in panel **a**. **d)** Analogous line profile of the gradient, depicted in panel **b** as a red line, with the maximum absolute value of the gradient field of $0.015\,\mu m^{-1}$. The spatial resolution was calculated by dividing the background noise by the absolute of the gradient of the polynomial fit. The average spatial resolution was found to be 150 nm and the maximum spatial resolution is 75 nm. Reproduced in part with permission from Nano Letters, in press. Copyright 2018 American Chemical Society.

The maximum absolute value of the gradient field is at

$$|\nabla \frac{I(t)}{I_0}|\ [1.29|0.06] \ = \ 0.0152\ \mu m^{-1}. \tag{3.1}$$

To determine the smallest detectable change in bead position, first, the standard deviation of the background intensity fluctuations of the IDA-setup without a bead above the grating is determined ($\sigma_{background} = 2.91 \cdot 10^{-4}$, calculated over 15 seconds) and is

multiplied by 3.92 in order to receive the 95% prediction interval of the background fluctuations. The latter is then divided by the maximum of the absolute of the gradient in order to calculate the smallest detectable change in position:

$$\frac{3.92 \cdot \sigma_{background}}{|\nabla \frac{I(t)}{I_0}|[1.29|0.06]} = \frac{1.141 \cdot 10^{-3}}{0.0152\ \mu m^{-1}} = 0.075\ \mu m = 75\,nm. \tag{3.2}$$

The average spatial resolution of the unit-cell was found to be 150 nm.

## 3.4 Continuous Approximation and Mobility-Simulation

In the previous section, it was shown that the short-term intensity fluctuations induced by beads with a constant speed allow the determination of the respective bead's velocity. The Fourier spectrum of intensity fluctuations arising due to the disturbances of a bead moving above the grating without any applied microfluidic flow shows higher Fourier amplitudes for lower than for higher frequencies. The latter is in indicator for Brownian noise, i.e. a signal arising from Brownian motion. In order to characterize the noise and confirm the assumption, the power spectral density (PSD) is plotted against the frequency. In general, the PSD of noise is proportional to $1/f^{\beta}$, whereas white noise corresponds to $\beta = 0$, pink noise to $\beta = 1$ and Brownian noise to $\beta = 2$ [40][41]. Plotting the logarithm of the PSD vs. the logarithm of the frequency and applying a linear fit yields $\beta$ as the negative slope of the fit [41]. The analysis of the intensity fluctuations of a single bead without flow, as presented in Figure 3.4c, results in $\beta = 1.64 \approx 2$ (Figure 3.6, and thus confirms the Brownian motion of the bead. The slightly smaller $\beta$ presumably arises from a rest momentum of the bead, as it was moved on to the grating with the micofluidic system, as well as from a possible thermal-gradient.

A typical measure for random motion (such as Brownian motion) is the diffusion coefficient [42]. The ability to analyze short-term intensity fluctuations regarding information on the diffusion coefficient of the objects moving above the grating is especially interesting for bacteria, since bacterial movement in general occurs as a random movement due to e.g. flagella-driven run-and-tumble cycles, gliding or passive Brownian motion [43][44][45]. The analysis of bacterial motion with the IDA-setup will be discussed more thoroughly in Chapter 4.4. This section presents an analysis method that allows a quantitative deduction of the diffusion coefficient from short-term intensity fluctuations induced by randomly moving objects. For this, a simulation in Wolfram Mathematica was developed and the resulting correlation between short-term intensity fluctuations and diffusion coefficient is compared to experimental results.

The fundamental idea of the following simulation was to generate short-term intensity fluctuations for randomly moving objects with different diffusion coefficients based on the

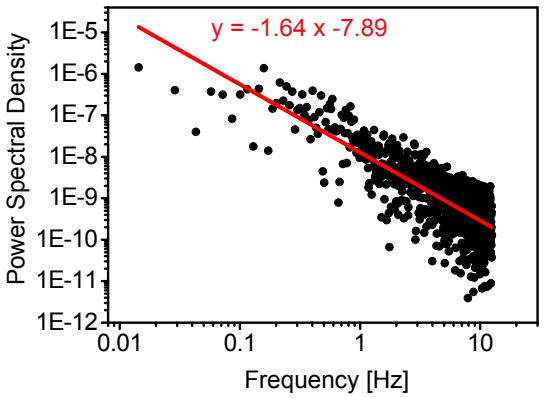


Figure 3.6: **Power spectral density (PSD) for short-term intensity fluctuations arising from a bead moving due to Brownian motion (log-log plot).** The negative slope of the linear fit function (red) yields $\beta = 1.64 \approx 2$. This means that the movement of the bead arises mainly from Brownian motion, as the PSD of the latter is proportional to $1/f^2$.

position-dependent intensity-decrease presented in Figure 3.3f. Subsequently, the simulated intensity fluctuations were Fourier transformed and the Fourier spectra correlated to the input diffusion coefficients. To that end, the position-dependent intensity-decrease (Figure 3.7a) was fitted by a two-dimensional polynomial function (Figure 3.7b, and previously discussed in Figure 3.5a. This continuous fit is utilized to simulate the short-term intensity fluctuations induced by one or multiple objects above the grating. For this, a random walk of an object is simulated by defining a run-and-tumble, i.e. the object moves a given distance per time section, whereupon it changes its direction by a random degree and then moves again for the given distance. The amount of tumbles was set to 25 per second, i.e. the same amount of images and intensity points acquired per second as in Section 3.3. The input diffusion coefficient was varied between 0 and 0.20 µm$^2$, as the upper boundary is the theoretical diffusion coefficient for 3 µm-sized beads in water at $37°C$ without restrictions in any dimension. The comparison to the theoretical diffusion coefficient for beads at room temperature and close to a surface will be discussed in more detail later in this section. The resulting trace of a random walk with a diffusion coefficient $D_1 = 0.05\,\mu m^2/s$ (green) and $D_2 = 0.15\,\mu m^2/s$ (blue) is shown in Figure 3.7b. The respective simulated intensity fluctuations are presented in Figure 3.7c. It can be seen that the higher diffusion coefficient $D_2$ results in bigger amplitudes of high frequencies as $D_1$. In order to receive information on the distribution of low and high frequencies, the Fourier amplitudes are fitted with an exponential decay function:

$$FA(f) = FA_0 \cdot e^{(-\frac{f}{\nu})} + c. \tag{3.3}$$

The fit-parameter $FA_0$ gives the Fourier amplitude at $f = 0\,Hz$ and $c$ is the y-axis offset. The important fit-parameter, however, is the exponential decay constant $\nu$, as it marks the frequency at which the fit decays to $FA(f) = \frac{FA_0}{e} + c \approx 0.368 \cdot FA_0 + c$

and thus is a measure for the distribution of high and low frequencies in the short-term diffraction peak intensity fluctuations. This means that a higher diffusion coefficient results in comparatively bigger Fourier amplitudes of high frequencies and thus in a larger exponential decay constant $\nu$. This can be seen for the two exemplary diffusion coefficients, with $\nu = 0.5\,\mathrm{Hz}$ for $D_1 = 0.05\,\mu\mathrm{m}^2/\mathrm{s}$ and $\nu = 1.8\,\mathrm{Hz}$ for the $D_2 = 0.15\,\mu\mathrm{m}^2/\mathrm{s}$. The exponential decay constant was extracted from simulated short-term fluctuations over 1000 data points (i.e. 40 seconds) for 40 diffusion coefficients between $D = 0\,\mu\mathrm{m}^2/\mathrm{s}$ and $D = 0.20\,\mu\mathrm{m}^2/\mathrm{s}$ as well as for one, five and ten objects moving simultaneously and independently on top of the grating. Each of the 120 parameter combinations was simulated 100 times and the evaluated exponential decay constants $\nu$ were averaged. The resulting correlation between the exp. decay constant $\nu$ and the input diffusion coefficient D is presented in Figure 3.7e. It was found that the decay constant $\nu$ is linearly proportional to the Diffusion coefficient D and is independent of the amount of objects moving on top of the grating. The latter is especially interesting for bacterial ensembles to e.g. determine the point in time, at which the bacteria attach to a surface and will be discussed in more detail in Chapter 4.4.

The resulting correlation of the decay constant $\nu$ and the diffusion coefficient is given as $\nu(D) = 10.4 \cdot D + 0.115$ for the simulation based on the 2D polynomial fit. Analogously to the simulation, the measured short-term intensity fluctuations allow conclusions on the diffusion coefficient of single beads with $D(\nu) = (\nu - 0.115)/10.4$. The experimental short-term intensity fluctuations arising from a bead that moved due to Brownian motion (Figure 3.4d) were Fourier transformed and the decay constant was found to be $\nu = 0.762\,\mathrm{Hz}$. Using the results from the mobility simulation, this corresponds to a diffusion coefficient of $0.0622\,\mu\mathrm{m}^2/\mathrm{s}$.

In order to compare this result with diffusion theory, the Einstein-Stokes equation [46] is used to calculate the expected diffusion coefficient. This equation describes the diffusion coefficient of spherical particles moving due to Brownian motion in infinitely dilute solutions. Einstein derived from Fick's law that particles in Brownian motion have a diffusion coefficient of

$$D = k_B T \,/f, \tag{3.4}$$

with $k_B$ being the Boltzmann's constant, $T$ the temperature and $f$ the frictional coefficient of the particle, which in general is unknown [47]. Stokes showed that for spherical particles with radius $r$ in a fluid with viscosity $\eta$, the frictional coefficient is given as [48]:

$$f_o = 6\pi\eta r, \tag{3.5}$$

and thus the respective diffusion coefficient is given as:

$$D_o = \frac{k_B T}{6\pi\eta r}. \tag{3.6}$$

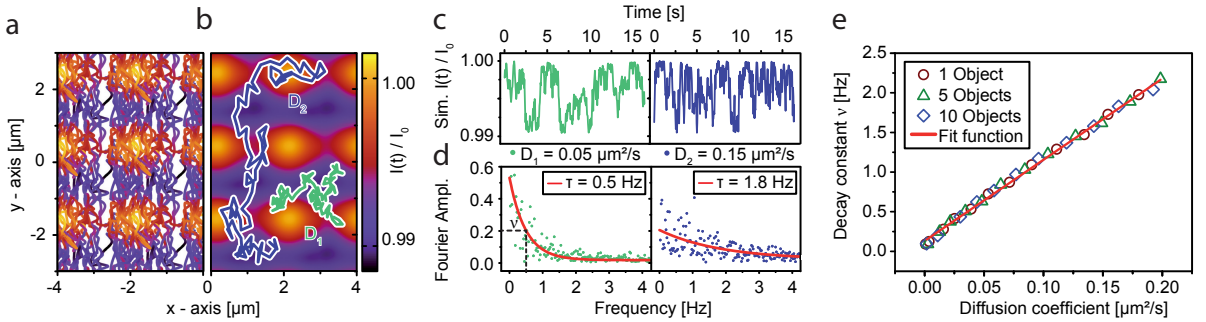


Figure 3.7: **Simulation of the position-dependent intensity-decrease of randomly moving objects. a)** Montage of the position-dependent intensity-decrease as shown in Figure 3.3f for 2 x 3 unit-cells. **b)** Two-dimensional, polynomial fit of 25th order of the position-dependent intensity-decrease shown in panel **a**. The intensity is color-coded. The green and blue line show the traces of simulated random walks for two different diffusion coefficients $D_1 = 0.05\ \frac{\mu m^2}{s}$ (green) and $D_2 = 0.15\ \frac{\mu m^2}{s}$ (blue). **c)** Simulated short-term intensity fluctuations for the diffusion coefficients shown in panel **b**, $D_1$ (left) and $D_2$ (right). **d)** Fourier amplitudes of the short-term intensity fluctuations shown in panel **c**. The red line shows the exponential decay fit and the dotted lines mark the decay constant $\nu$ in the left panel. The resulting decay constants are $\nu_1 = 0.5\,\mathrm{Hz}$ for $D_1$ and $\nu_1 = 1.8\,\mathrm{Hz}$ for $D_2$. **e)** The simulated decay constant $\nu$ is linearly proportional to the input diffusion coefficient. The proportionality is independent of the amount of disturbing objects above the grating, as presented for one, five and ten independently moving objects. The red linear fit function is $\nu(D) = 10.4 \cdot D + 0.115$. Reproduced (modified) with permission from Nano Letters, in press. Copyright 2018 American Chemical Society.

For spherical particles moving closely to a surface, hydrodynamic coupling between the particle and the surface reduces the lateral diffusion coefficient to approximately [49] [50][51]:

$$D \approx D_o(1 - \frac{9}{16}\frac{r}{h}), \tag{3.7}$$

with $h$ being the distance of the particle's center to the surface. For the presented measurements with 3 µm-sized beads, which were performed at $T = 20°C$ in water with a viscosity $\eta = 1\,m\,Pa\,s$, and under the assumption that the beads are moving directly above the surface, this results in:

$$D \approx 0.1431(1 - \frac{9}{16}\frac{r}{h})\,\mu m^2/s \;=\; 0.0626\,\mu m^2/s. \tag{3.8}$$

This result is in very good agreement with the diffusion coefficient determined from the simulation of $D_{sim} = 0.0622\,\mu m^2/s$.

This section has shown that the IDA-setup enables a mobility analysis of objects moving above the grating and, as will be presented in the next chapter, also allows a quantitative, non-absolute, temporal course of the diffusion coefficient of a bacterial ensemble.

# Chapter 4

# IDA of Living Bacterial Cells

Having shown that the IDA-method can be used to quantify the amount and mobility of latex-beads, this chapter discusses the analysis of living bacterial ensembles above the gold grating (Figure 4.1). In the first section, it is shown that a growing bacterial ensemble leads to a progressively decreasing diffraction-peak intensity. This section further shows the ability of the IDA-method to resolve growth on the single-cell level. The correlation between IDA-signal and amount of bacteria is further discussed in Section 4.2, where the detection range over two orders of magnitude of cell numbers is presented. Section 4.3 describes the extraction of bacterial growth parameters from IDA-measurements and compares the results to standard optical density analysis. In the last section, the mobility analysis presented in Chapter 3.4 is applied to a bacterial growth measurement. Here, a decrease of the bacterial mobility by a factor of three due to attachment of the cells to the surface and each other can be concluded from the IDA-signal.

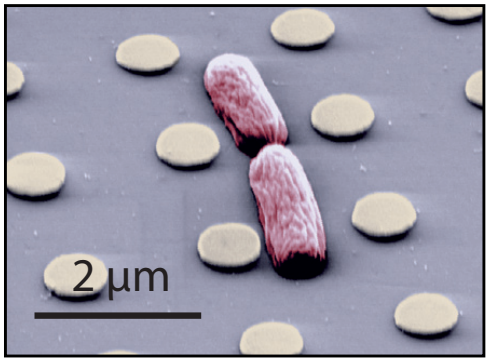


Figure 4.1: **Scanning electron micrograph of bacteria on top of a gold grating.** The false-colored SEM-micrograph shows two bacteria on top of a gold grating on a silicon substrate. The periodicity of the grating is 2 µm and the diameter of the gold islands is 0.8 µm. The same parameters were used for all measurements in this chapter. Reproduced (modified) with permission from Nano Letters, in press. Copyright 2018 American Chemical Society.

## 4.1 Quantitative Growth at the Single-Cell Level

As discussed in the introduction of this thesis, the increasing number of multi-resistant bacteria is a major health issue for the current as well as upcoming generations. To be able to tackle the further spreading of multi-resistant bacteria, it is important to prescribe an appropriate and specific antibiotic for a given inflammation as soon as possible. In order to do so, the process of antimicrobial susceptibility testing (AST) likewise has to be shortened significantly. While conventional AST setups take up to 20 hours to find a suitable antibiotic [52], several new promising techniques were presented in the recent past that allow AST in less than three hours [52][53]. A high sensitivity of bacterial growth is important for fast results [54]. In this context, the sensitivity of the IDA-setup for growth measurements of low cell numbers is evaluated in this section.

A second crucial feature of a robust, novel AST assay is a good understanding of the measured signal and it's interpretation. In order to quantify and analyze the correlation between the number of bacteria and the diffraction peak intensity, microscopy images of the bacteria growing on top of the grating together with the corresponding diffraction peak intensity were acquired simultaneously using the microscope-configuration presented in Chapter 2.1.1. Similar to the measurements with the transparent latex-beads, the bacteria were grown on a gold grating using a silicon dioxide substrate that was attached to an *Ibidi sticky-Slide VI 0.4*. As a model bacterium, the non-pathogenic *Escherichia coli* (*E. coli*) S-strain (BZB1011 [55]) was examined. To assure natural, exponential growth behavior, bacteria were grown over night prior to each measurement. The overnight culture was then diluted to an $OD_{600}$ of 0.05 and the bacteria were grown to $OD_{600}$ 0.2 in a day culture, thus ensuring that they are in the exponential growth phase during the experiment. The resulting suspension was then again diluted by a factor of 150, resulting in approx. zero to one bacteria on top of the grating at the beginning of a measurement. The measurements in this section were performed without microfluidic flow and at room temperature.

The resulting diffraction-peak intensity course for a bacterial growth measurement is shown in Figure 4.2a. The growth of the bacteria on the grating resulted in a continuous decrease of the diffraction-peak intensity of approx. 20% after the first ten hours (black line). A reference measurement without bacteria remained stable at $I(t)/I_0 = 1.000 \pm 0.006$ (red line). In order to correlate the IDA-signal to the amount of bacteria, the microscopy images were evaluated. To this end, the number of bacteria was determined manually for each frame until the population reached 20 bacteria. The amount was consequently correlated to the respective diffraction peak intensity-decrease. The results are shown in Figure 4.2b. The intensity was averaged over 60 seconds, in order to increase the bacterial resolution. The plot shows a linear correlation between the mean normalized intensity and the number of bacteria n, with the linear fit being $f(n) = 1 - 7.86 \cdot 10^{-4}\, n$ (red line). The error-bars mark the 95% prediction interval, i.e. $\pm 1.96 \cdot \sigma$. Dividing the average 95% prediction interval by the slope of the fit shows

that the IDA-setup allows bacterial growth measurements of low cell numbers with a resolution of $\frac{3.92 \cdot \sigma_{mean}}{fitslope} = 1.6$ bacteria.

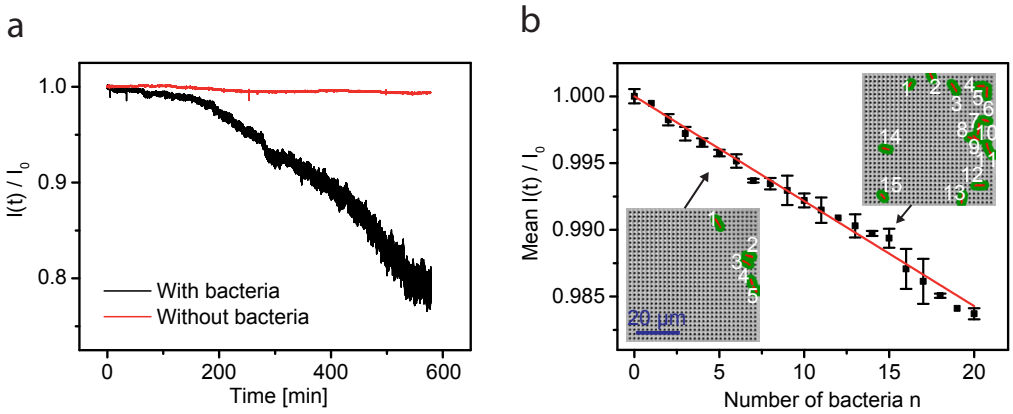


Figure 4.2: **Quantitative growth detection at the single-cell level.**
**a)** Diffraction-peak intensity course for a bacterial growth measurement in LB medium (black line) as well as a control measurement without bacteria (red line). Disturbances arising from the bacteria lead to a diffraction peak intensity-decrease of approx. 20% after 10 hours, while the control measurement remains stable at $I(t)/I_0 = 100.0 \pm 0.6\%$ during the same duration. **b)** The mean normalized intensity plotted against the respective number of bacteria n shows a linear decrease. A fit gives $f(n) = 1 - 7.86 \cdot 10^{-4} n$ (red line). The error bars mark $\pm 1.96 \cdot \sigma$, i.e. the 95% prediction interval. The intensity was averaged over 60 seconds, in order to increase the bacterial resolution. Division of the average 95% prediction interval by the slope of the fit shows a bacterial resolution of 1.6 bacteria. Reproduced (modified) with permission from Nano Letters, in press. Copyright 2018 American Chemical Society.

While the signal seems to be noisy due to the movement of the bacteria and the resulting short-term intensity fluctuations, the measurement in Figure 4.2a yields high signal-to-noise ratios (SNR) as soon as the first bacteria grow on top of the grating. Using $SNR = \frac{\mu}{\sigma}$ with $\mu$ being the mean diffraction-peak intensity-decrease and $\sigma$ being the standard deviation (both calculated over a time interval of 1 minute) yields the following SNRs at the given time points:

| Time [min] | 30 | 100 | 200 | 300 | 400 |
|---|---|---|---|---|---|
| SNR | 4.9 | 11.4 | 29.2 | 32.6 | 36.2 |

Table 4.1: **Signal-to-noise ratios (SNR).** Signal-to-noise ratios for the bacterial growth measurement shown in Figure 4.2a. The results show a high SNR for bacterial growth measurements already after 30 minutes.

A further comparison between the counted number of bacteria, the area of the grating covered by the bacteria and the mean diffraction-peak intensity (averaged over two seconds) of the growth measurement shown in Figure 4.2 is given in Figure 4.3. Comparing the three plots shown in the figure does not only show a clear correlation between the counted bacteria and the diffraction-peak intensity, but also between the covered area and the other two parameters. The covered area was determined by subtracting the background image, i.e. an image of the grating without bacteria, from the image at a given time. This procedure is described in more detail in the following section.

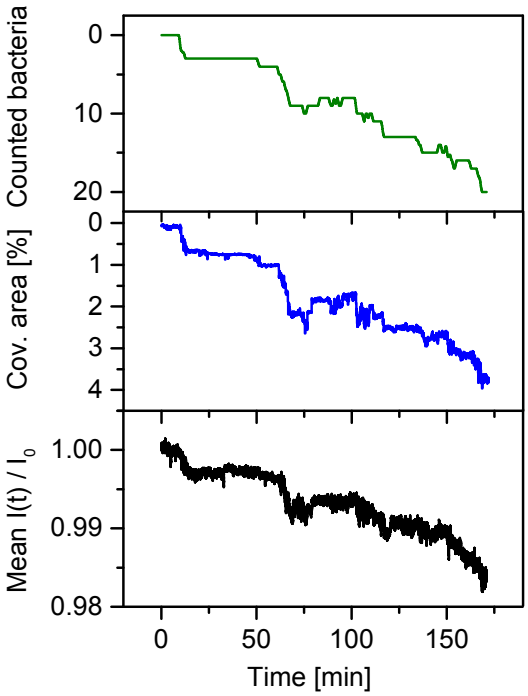


Figure 4.3: **Comparison of bacterial number, covered area and mean normalized intensity.** The direct comparison between the hand-counted bacteria (top-graph), covered area obtained from microscopy middle-graph) and the diffraction-peak intensity (bottom graph) for the first 150 minutes of the growth measurement presented in Figure 4.2a shows a strong correlation. Reproduced with permission from Nano Letters, in press. Copyright 2018 American Chemical Society.

## 4.2 Quantitative Growth over Two Orders of Magnitude

While the first 20 bacteria were countable from the microscopy images, determining the precise amount of bacteria beyond 20 is not feasible, as the bacteria start to agglomerate

and lose a precise outline, in addition to the already hampered visibility due to the gold grating. To be able to correlate the IDA-signal to higher numbers of bacteria, the area of the grating that is covered by bacteria was evaluated. It was shown previously that the covered area is a suitable measure for the cell amount [56]. As shown in the top two graphs of Figure 4.3, there is a linear correlation between the covered area and the counted bacteria, with 1% of covered area corresponding to approx. 4.7 bacteria. The covered area was determined from the microscopy images by subtracting an image of the grating without bacteria from the whole measurement stack. A binary threshold was then applied, yielding the visible bacteria above the grating, which could be quantified by reading out the relative amount of covered area. Yet, this method underestimates the actual area covered by bacteria because of obstructions in form of gold islands as well as outer regions of the bacteria getting lost due to gray values close to the background. To compensate for this, the resulting covered area was corrected with a multiplication factor. The latter was retrieved by evaluating the area covered by bacteria outside of the grating at approx. 50% covered area and dividing it by the respective determined covered area of the section covered by the grating.

The correlation between the normalized diffraction-peak intensity and the covered area was performed for two long-time bacterial growth measurements. The results are shown in Figure 4.4. The left plot, Figure 4.4a, shows the evaluation for the growth measurement from Figure 4.2a. Again, a linear correlation between the normalized diffraction-peak intensity and the covered area can be found, with the fit-function being $f(x) = 1 - 0.0037\,x$. Figure 4.4b depicts the correlation for the data from a longer growth measurement shown in Figure 4.7a. The plot shows a linear correlation for approx. the first 70% of covered area as well, with a very similar fit function of $f(x) = 1 - 0.0036\,x$. At a covered area of 70% or higher, the bacteria begin to grow on top of each other and aggregate, resulting in a non-linear relation between the diffraction-peak intensity and the covered area. While we were unable to determine the number of bacteria after the ensemble started to grow in the third dimension and aggregate, we did not see a kink or unusual behavior of the IDA-signal at covered areas of approx. 70%. This suggests that the IDA-signal is suitable for growth measurements in 2D and, to a certain degree that is to be determined in future projects, in 3D.

## 4.3 Extracting Growth Parameters

Since the IDA-method shows a linear correlation between bacterial number and the decrease of the diffraction-peak intensity, it allows for quantitative growth analysis of bacterial ensembles on a surface. Bacterial growth in general is divided into four different phases [8]: 1. The lag phase, during which the bacteria adapt to growth conditions. During this phase, synthesis of enzymes, RNA, and other molecules occurs [57]. 2. The exponential phase, during which exponential growth occurs and the growth rates or doubling times are extracted. This phase takes place until the medium's nutrients are de-

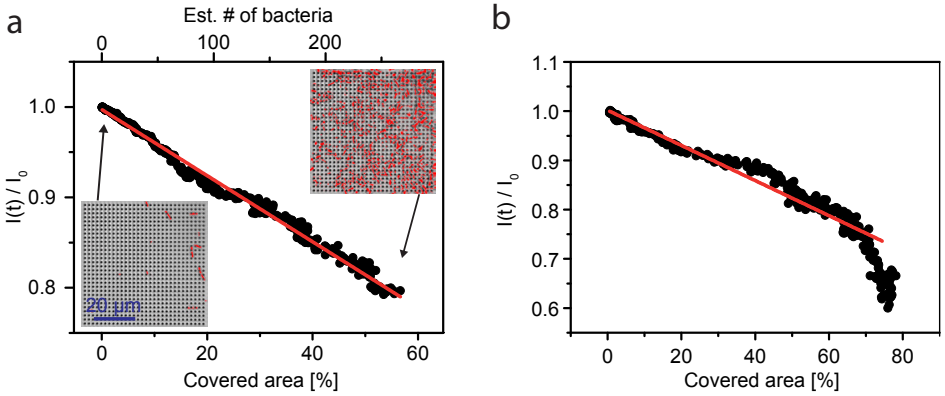


Figure 4.4: **Correlation between diffraction-peak intensity and covered area.** **a)** Normalized diffraction-peak intensity plotted against the grating area that is covered by bacteria for the growth measurement shown in Figure 4.2a. The plot shows a linear correlation with a fit function of $f(x) = 1 - 0.0037\,x$ (red line). The estimated amount of bacteria is determined by extrapolating the data shown in Figure 4.2b and 4.3, with 1% of covered area being equivalent to approx. 4.7 bacteria. Microscopy images were taken every minute and the diffraction-peak intensity was averaged over the respective minutes. The microscopy images shown in the corners were taken at t = 100 min (left) and t = 550 min (right). **b)** Normalized diffraction-peak intensity plotted against the grating area covered by bacteria for the growth measurement shown in Figure 4.7a. The linear section, which ranges from 0% up to approx. 70% covered area, has a similar slope to the one shown in **a**, with the fit function being $f(x) = 1 - 0.0036\,x$. At 70% covered area, the bacteria start to aggregate as well as grow in the third dimension. Reproduced (modified) with permission from Nano Letters, in press. Copyright 2018 American Chemical Society.

pleted and it is enriched with waste products, or the available space is used up. 3. The stationary phase, occurring when bacterial growth stagnated due to one of the above-mentioned reasons. During this phase, rates of cell-division and cell-death balance each other out [58]. 4. The death phase, during which bacteria die due to a lack of nutrients or other influences such as non-tolerated temperatures or toxins.

In this section, the doubling times of two bacterial strains are measured using the IDA-setup and are compared to results obtained with a standard technique, the optical density analysis at $\lambda = 600\,\text{nm}$ ($OD_{600}$). To this end, the *E. coli* S-strain (BZB1011 [55]) and C-strain (BZB1011 E2C [55]) were used, as these differ significantly in their doubling times [59]. Both starter cultures were grown overnight at 37°C in LB medium and were resuspended in the morning to an $OD_{600}$ of 0.05. The suspension was then grown to an $OD_{600}$ of 0.2 to assure exponential growth. Subsequently, it was once again diluted by a factor of 50 in LB medium, resulting in an even distribution of one to five bacteria above a gold grating. To reduce the lag phase as much as possible, the handling of the bacteria at room temperature was kept to a minimum of approx. 10 minutes. The

diffraction-peak intensity is plotted as $1-(I(t)/I_0)$ in order to compare the results to the $OD_{600}$-measurements.

To be able to measure six growth curves simultaneously while using the exact same bacterial cultures, the scanning configuration for high-throughput as described in Section 2.1.2 was used at T = 37°C. Since in this configuration the bacteria were grown in a separate plastic dish and no optical microscope control can be applied, 120 x 120 µm$^2$-sized gratings (60 x 60 gold structures) were used to assure starting concentrations of 1-5 bacteria above the grating. The results of the simultaneously acquired IDA-measurements for three S-strain (red) and three C-strain (blue) growth curves are shown in Figure 4.5a. The bold points show the averaged data of one scanning cycle, i.e. three samples per strain and one minute of acquisition per sample. Bacterial growth can be described mathematically by a sigmoidal logistic function,

$$N(t) = \frac{N_{max}}{1 + e^{-\mu(t-t_c)}}, \tag{4.1}$$

with the doubling times given as $\ln(2)/\mu$ [60]. Fitting the latter to the diffraction peak intensity-decrease yields doubling times of $\mu_s = 26.7 \pm 1.4$ min for the S-strain and $\mu_c = 32.7 \pm 0.9$ min for the C-strain (Table 4.2). The doubling times of sixteen further samples were simultaneously measured using a reference technique, i.e. optical density measurement at 600 nm wavelength (Perkin Elmer Lambda EZ201 spectrophotometer) [61], in order to confirm the results obtained from the IDA-setup. Therefore, eight samples per strain, taken from the same overnight culture as the IDA-samples, were analyzed. The results of the $OD_{600}$-measurements are shown in Figure 4.5b and Table 4.2. The bold points again show the averaged data. Applying the sigmoidal growth fit function (Equation 4.1) to the individual growth curves yields doubling times of $28.7 \pm 2.4$ min for the S-strain and $33.5 \pm 2.2$ min for the C-strain, which are in good agreement with the doubling times obtained from the IDA-measurement. All results were analyzed using the t-test (in Wolfram Mathematica), a test to measure the statistical significance of results. The test yielded a probability-value (p-value) of 0.0029 for the IDA-measurements and 0.0017 for the $OD_{600}$-measurements. Both values are far below the desired p-value of 0.05. The latter means that the probability that both datasets are from an identical real set of measurement values is below 5%. In conclusion, this paragraph has shown that the IDA-method is capable of bacterial growth measurements with a precision similar to that of optical density setups.

To show that a bacterial growth measurement has surpassed the exponential growth phase, it is suitable to plot the data in a semi-logarithmic graph. The exponential growth phase can then be seen as a linear section. The following stationary phase is marked by a strong decline of the slope. The S- and C-strain measurements obtained with the IDA-setup plotted in a semi-logarithmic graph can be seen in Figure 4.6. During the first 30 minutes, the diffraction-peak intensity is similar to the starting intensity I(0), resulting in a comparatively noisy signal. After approx. 45 minutes, the exponential phase

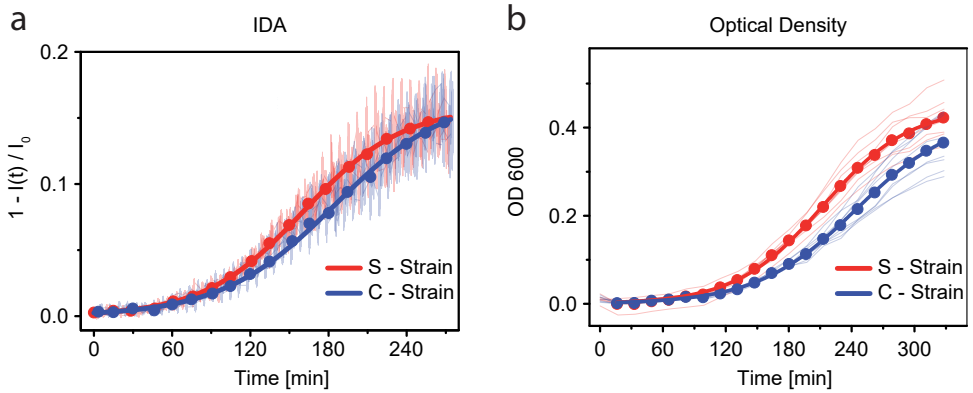


Figure 4.5: **Bacterial growth curves obtained from the IDA-setup and optical density measurements. a)** Diffraction peak intensity-decrease for six bacterial growth curves of the S- and C-strain, with three measurements of each strain. The bold points and lines show averaged data and a sigmoidal logistic fit. The resulting doubling times are $\mu_s = 26.7 \pm 1.4\,\text{min}$ for the S- and $\mu_c = 32.7 \pm 0.9\,\text{min}$ for the C-strain. **b)** Optical density measurement at $\lambda = 600$ nm of bacterial growth for eight samples of S- and C-strain, respectively. The bold points and lines show averaged data and a sigmoidal logistic fit. The resulting doubling times are $28.7 \pm 2.4\,\text{min}$ for the S- and $33.5 \pm 2.2\,\text{min}$ for the C-strain. All measurements were performed in LB medium. Reproduced with permission from Nano Letters, in press. Copyright 2018 American Chemical Society.

begins and lasts until approx. 150 minutes. The doubling times can also be extracted by fitting a linear fit to the exponential phase in the semi-logarithmic plot and calculating the reciprocal of the slope. This method yields doubling times of $28.8 \pm 2.4$ minutes for the S- and $32.3 \pm 3.5$ minutes for the C-strain. These values are in good agreement with the logistic fit evaluation method.

When the total diffraction peak intensity-decrease at the stationary phase of growth measurements in the microscope-configuration (Figure 4.7a, maximum decrease $\approx 60\%$) and the scanning-configuration (see Figure 4.5a, maximum decrease $\approx 15\%$) are compared, it can be seen that the ability to measure in high-throughput comes with a tradeoff in form of a reduced sensitivity by a factor of 3-4. This reduced sensitivity assumedly arises due to the greater distance between the bacteria and the diffraction grating (at least $180\,\mu\text{m}$). Albeit the reduced bacterial sensitivity, the mobility analysis of the bacteria is feasible with both the microscope-configuration and the scanning-configuration, which will be presented in the following Section 4.4 and Chapter 6.

## 4.4 Mobility Analysis

In the previous chapter, the IDA-setup was used to determine the speed of moving latex-beads and a model was presented in Section 3.4 that allows the determination of a dif-

| | IDA: Doubling times [min] | | | |
|---|---|---|---|---|
| C-strain 1 | 31.94 | | S-strain 1 | 25.71 |
| C-strain 2 | 32.48 | | S-strain 2 | 28.268 |
| C-strain 3 | 33.598 | | S-strain 3 | 26.196 |
| | OD: Doubling times [min] | | | |
| C-strain 1 | 36.69 | | S-strain 1 | 23.673 |
| C-strain 2 | 33.086 | | S-strain 2 | 30.7655 |
| C-strain 3 | 33.485 | | S-strain 3 | 30.79 |
| C-strain 4 | 30.176 | | S-strain 4 | 27.814 |
| C-strain 5 | 35.25 | | S-strain 5 | 31.39 |
| C-strain 6 | 30.32 | | S-strain 6 | 26.3855 |
| C-strain 7 | 34.83 | | S-strain 7 | 29.9157 |
| C-strain 8 | 34.4506 | | S-strain 8 | 29.259 |

Table 4.2: **Doubling times obtained from the IDA and optical density (OD) measurements.** Individual results for the doubling times extracted from the growth curves shown in Figure 4.5.

fusion coefficient from the short-term intensity fluctuations. This model is based on the Fourier transformation of the short-term intensity fluctuations. After the transformation, the spectrum of the Fourier amplitudes is studied. Because the diffraction-peak intensity depends on the disturbing object's position within a unit-cell, as shown in Figure 3.7a for beads, faster movements of objects on top of the grating lead to more high-frequency intensity fluctuations and thus also to bigger Fourier amplitudes at higher frequencies. The distribution of the Fourier spectrum follows an exponential decay and an exponential fit can be used to extract the decay constant $\nu$. It was shown in Figure 3.7e that the decay constant $\nu$ is proportional to the diffusion coefficient of the moving objects, while being independent of the amount of objects moving simultaneously on top of a grating.

The mobility analysis was applied to the bacterial growth measurement shown in Figure 4.7a. During this measurement, the bacteria were grown on a 60 x 60 $\mu m^2$-sized gold grating (30 x 30 gold structures) using a $SiO_2$-substrate and measured with the microscope configuration (Chapter 2.1.1) in order to correlate the IDA-results to real-space microscopy images. Figure 4.7a further shows two exemplary microscopy images at $t_1 = 300\,\text{min}$ and $t_2 = 500\,\text{min}$. At $t_1$, the evaluated covered area is approx. 51% and the bacteria are evenly distributed across the grating. The image at $t_2$ (covered area $\approx 76\%$) shows that the bacteria are packed densely and started to aggregate and adhere to the surface. The short-term fluctuations over 1.3 minutes (1000 data points) are presented in Figure 4.7b. Comparing the intensity fluctuations, the data for $t_1$ (left half) shows bigger amplitudes for high-frequency fluctuations than the data of $t_2$. The respective Fourier amplitudes with an exponential decay fit (red line) can be seen in Figure 4.7b. The data for $t_1$ yields an exponential decay constant of $\nu = 0.5\,\text{Hz}$, which is five times higher than the result for $t_2$ with $\nu = 0.1\,\text{Hz}$. This means that the Fourier spectrum at $t_1$ has a bigger ratio of high frequencies than the Fourier spectrum at $t_2$. Applying the mobility-model

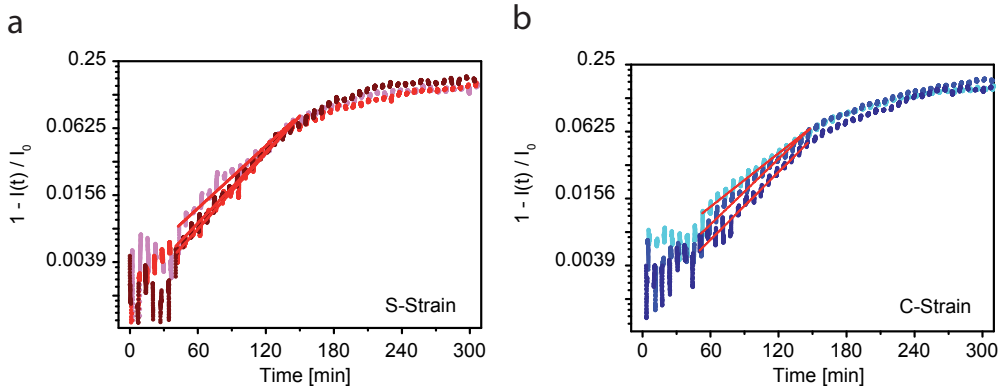


Figure 4.6: **Semi-logarithmic plot of IDA-measurements of bacterial growth. a)** Semi-logarithmic plot of the diffraction peak intensity-decrease for the three S-strain growth measurements shown in Figure 4.5a. The red lines show a linear fit to the exponential growth phase. The resulting doubling times are $28.8 \pm 2.4$ minutes. **b)** Analogous plot for the C-strain measurements shown in Figure 4.5a. The doubling times extracted from the linear fits (red lines) are $32.3 \pm 3.5$ minutes. Reproduced in part with permission from Nano Letters, in press. Copyright 2018 American Chemical Society.

to the whole growth measurement with intervals of 1000 data points or 1.3 minutes each yields the decay constant $\nu$ progression as shown in Figure 4.7d. The blue curve shows a moving average over 100 data points. The progression of $\nu$ stays constant for the first 300 minutes during which the bacteria maintain the same mobility respectively diffusion coefficient. At $t = 300\,\text{min}$ the decay constant $\nu$ decreases by a factor of 3.2 until approx. $t = 500\,\text{min}$, where it stays constant again. This decrease in diffusion coefficient can be ascribed to the attachment of the bacteria to a surface as well as to each other. This behavior is an indicator for early stages of biofilm formation [62][63]. *E. coli* bacteria assemble extracellular adhesive amyloid fibres after approx. 360 minutes, which improve surface attachment and promote biofilm formation [64]. In addition to this, it was previously shown under similar measurement conditions that *E. coli* bacteria form biofilms at such advanced time-points due to nutrient limitations [65].

In order to confirm the mobility analysis with the actual movement of the bacterial ensemble, microscopy images were taken every 30 seconds. Since the decay constant $\nu$ in Figure 4.7 is independent of the amount of bacteria, an according analysis of the microscopy images was applied. For this purpose, the gray value difference between two subsequent images $(P_{i+1} - P_i)$ was calculated. The latter yields the area corresponding to the bacteria that have moved between the two images. If a bacterium has attached to the surface, it does not contribute to this value. To normalize the amount of moving bacteria to the absolute amount of bacteria, the result was divided by the difference between the current image and the background image $(P_i - P_0)$, i.e. an image of the grating without bacteria. The results are presented in Figure 4.8. Since the images were acquired

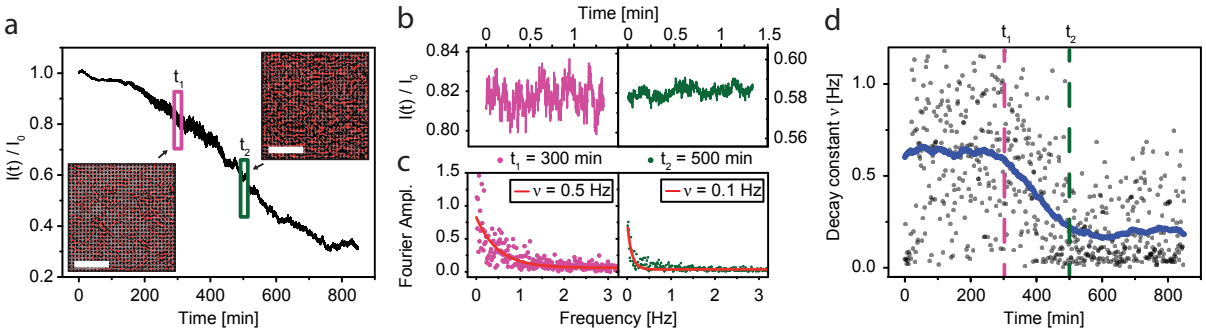


Figure 4.7: **Mobility analysis of a bacterial growth measurement. a)** Normalized diffraction-peak intensity for a bacterial growth measurement of *E. coli*. The microscopy images were taken at $t_1 = 300\,\text{min}$ (left) and $t_2 = 500\,\text{min}$ (right). The scale bar is $20\,\mu\text{m}$. **b)** Short-term intensity fluctuations at $t_1$ (magenta) and $t_2$ (green) for 1.3 minutes (1000 data points). **c)** Fourier spectrum of the short term intensity fluctuations shown in **b**. The red line shows an exponential decay fit, with a decay constant $\nu = 0.5\,\text{Hz}$ for $t_1$ and $0.1\,\text{Hz}$ for $t_2$. This means that the intensity fluctuations from $t_1$ have a bigger relative amount of high-frequent Fourier amplitudes due to a higher diffusion coefficient resp. mobility of the bacteria. **d)** Decay constants $\nu$ for the whole growth measurement. The gray points show the decay constants for intervals of 1.3 minutes (1000 data points) and the blue points depict a moving average over 100 decay constants. The decay constant $\nu$ of the bacterial ensemble stays constant during the first 300 minutes. Between $t = 300\,\text{min}$ and $t = 500\,\text{min}$, the decay constant decreases by a factor of 3.2 and subsequently remains constant again. Reproduced (modified) with permission from Nano Letters, in press. Copyright 2018 American Chemical Society.

with a bright-field microscope and the bacteria are obstructed by the gold structures, this analysis is comparatively noisy for very low bacterial amounts, i.e. the beginning of the experiment up until approx. $t = 130\,\text{min}$. Thereafter, the analysis shows that the relative amount of moving bacteria stays the same until $t = 300\,\text{min}$, where it decreases for the next 200 minutes. In total, the time course shows a similar behavior as the decay constant $\nu$ in Figure 4.7, with a decrease of mobile bacteria at the exact same time, thus confirming the ability to measure bacterial mobility with the IDA-setup. The latter holds the potential for analyses of biofilm-forming bacterial strains towards e.g. antimicrobial susceptibility or mobility-restricting drugs.

While the measurements presented in this section so far were all conducted with the microscope-configuration and with the diffraction grating positioned inside the probing channel, the following experiment demonstrates that the mobility analysis is also possible with the scanning-configuration, where the diffraction grating is outside of the probing channel. To this end, we used transparent Ibidi µ-slides (VI 0.4) with planar probing channels with a measurement volume of $150\,\mu\text{l}$. Bacteria were grown and analyzed with

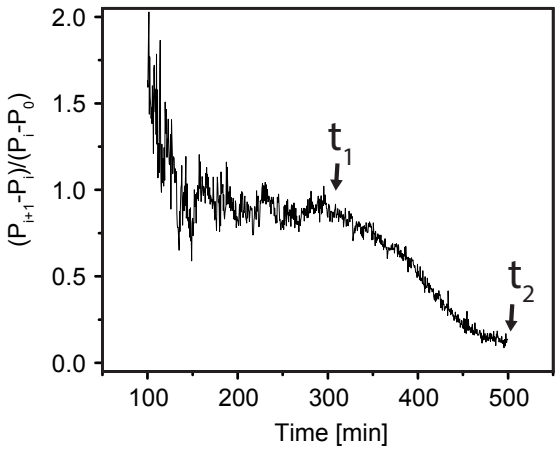


Figure 4.8: **Image analysis of the bacterial mobility.** Time-course of the image analysis describing the mobility of the bacterial growth measurement shown in Figure 4.7 which es evaluated as $(P_{i+1} - P_i)/(P_i - P_0)$. The results show a decrease of mobile bacteria over the exact same duration as in Figure 4.7c, with a decrease of the mobility between $t_1 = 300$ min and $t_2 = 500$ min. Reproduced (modified) with permission from Nano Letters, in press. Copyright 2018 American Chemical Society.

the IDA-setup in two channels simultaneously. One channel was left untreated and the other one was previously passivated with poly-L-lysine (PLL). PLL is a cationic polymer known to enhance the attachment of bacteria to surfaces [66].

The PLL passivation was done by covering the bottom of the probe channel with 50 µl of PLL. The latter was left for two hours to act upon the surface. The well of the probe channel was thereafter rinsed three times with 150 µl of MilliQ water and twice with M63 minimal medium. For the preparation of the measurement, the S-strain was grown overnight at 37C in M36 minimal medium. The minimal medium was used to guarantee the functionality of PLL. The overnight culture was diluted to an $OD_{600}$ of 0.05 and the subsequent day-culture was left to grow until it reached an $OD_{600}$ of 0.2. For the measurement without PLL, 60 µl of the day-culture were given inside the probe channel and the latter was filled with an additional 90 µl of M63 medium. The probe channel with PLL-treated surface was filled with 20 µl of day-culture and filled with an additional 130 µl of M63 medium. The bacteria in both channels were placed inside an incubator for 10 minutes for them to settle to the bottom, whereupon the channels were rinsed three times with M63 medium, thus achieving similar starting concentrations of bacteria in both channels (see Figure 4.9a and b). Subsequently, the IDA measurements were started. During the measurements, the probe channel was kept at 37 °C. The bacteria on the surface without PLL show a decay constant $\nu$ which is higher than the respective value for the PLL passivated sample by a factor of 2-3 (Figure 4.9c). This result shows

that our method is capable of analyzing bacterial adhesion properties to differently functionalized surfaces in both IDA configurations.

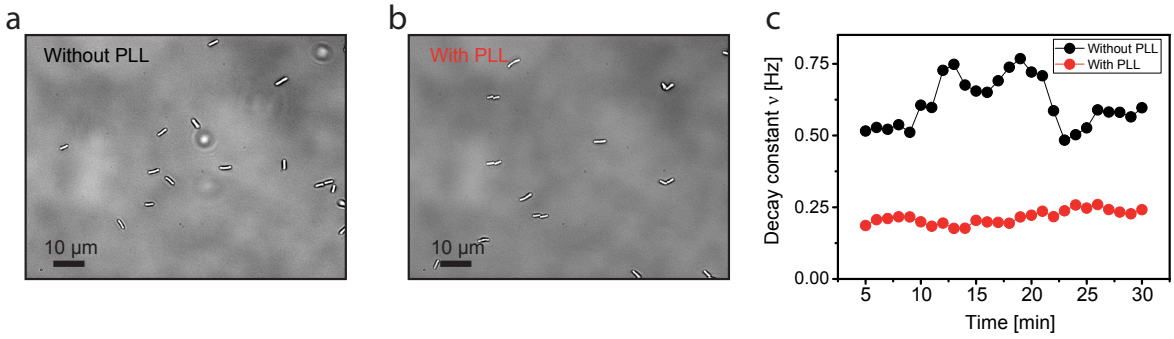


Figure 4.9: **Mobility analysis of S-strain *E.coli* with and without poly-L-lysine (PLL) surface passivation. a)** Microscopy image of the starting bacterial density of the sample without PLL surface passivation. **b)** Microscopy image of the starting bacterial density of the sample with PLL surface passivation, as a confirmation that both samples had similar starting concentrations of bacteria. **c)** Mobility analysis for 30 minutes for bacterial movement on a surface with and without PLL passivation (moving average over five minutes). The sample without PLL passivation shows a similar decay constant $\nu$ as the bacteria in the growth measurement from Figure 4.7 before the attachment to the surface. The sample with PLL on the other hand shows a decay constant $\nu$ similar to the bacteria from Figure 4.7 after they had attached to the surface, which is approx. 2-3 times smaller than $\nu$ of the sample without PLL.

## 4.5 IDA of Bacteria Extracted from Blood Serum

The measurements shown so far in this chapter were all done with isolated samples of bacterial strains. However, in clinical samples, such as blood or urinary tract infections, other components as, e.g., blood cells are located inside the sample and the bacteria need to be isolated for IDA evaluation. There are several techniques that allow the isolation of bacteria from blood or urine samples in a short time of less than 10 - 20 minutes [67]. One example being differential centrifugation [68][69], where the sample is first centrifuged at a lower RPM in order to sediment blood cells. The supernatant is then centrifuged at higher RPMs in order to sediment the bacteria. For a simulation of the second step of this isolation technique, we inoculated Bacillus subtilis (NCIB 3610) in blood serum at approx. $10^7$ cells/ml. The bacteria were then extracted from the sample by centrifugation at 6000 rpm for five minutes, whereupon the supernatant was resuspended in Mueller Hinton Broth and subsequently analyzed with the IDA-method. While some lipid aggregates

still remained, bacterial growth was rapidly and clearly detectable with the IDA-setup (Figure 4.10).

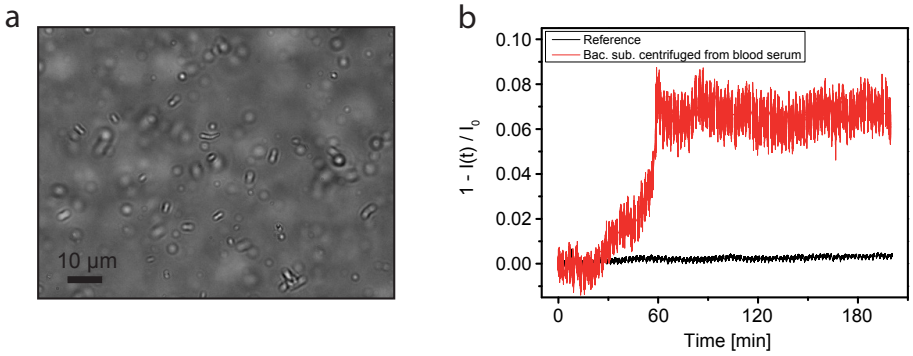


Figure 4.10: **Growth analysis of bacteria after extraction from blood serum. a)** To simulate a biological sample, Bacillus subtilis (NCIB 3610) were inoculated in blood serum at approx. $10^7$ cells/ml. After centrifugation at 6000 rpm for five minutes, the liquid part was removed and the remains were resuspended in Mueller Hinton Broth. The microscopy image shows the resuspended sample, with some lipid aggregates still remaining. This sample was evaluated with the IDA method. **b)** IDA-measurement of the sample described in panel **a**. Despite the debris, bacterial growth was rapidly and clearly detectable.

In summary, this chapter has shown that the IDA-method allows a sensitive detection of bacterial growth, ranging from single to hundreds of bacteria. Furthermore, the detection method can be used to correctly determine doubling times and to analyze the mobility of the bacterial ensemble. Here, it was shown that the mobility decreases due to the attachment of the bacteria to a surface and varies for differently passivated surfaces.

# Chapter 5

# Antimicrobial Susceptibility Testing

The amount of multidrug-resistant bacteria has increased alarmingly in the past years due to a redundant and inappropriate use of antibiotics [4][6]. With currently 700,000 annual deaths due to antibiotic resistance (ABR), this number is estimated to increase up to 10 million by 2050 [7]. A crucial factor in the increase of antibiotic resistances is the use of broad-spectrum antibiotics as a quick first-choice, because the identification of an appropriate small-band antibiotic with conventional AST methods can take up to several days [52]. To support the emerging battle against antibiotic resistance, methods that allow fast and accurate antimicrobial susceptibility testing (AST) are urgently needed. An early identification and subsequent therapy with an appropriate antibiotic can further lead to lower mortality rates, a shortened care duration, performance of less invasive procedures and substantial cost savings [70][71]. While there are several methods to determine the antibiotic resistance of a given bacterium, a large number of techniques still relies on phenotypic antibiotic susceptibility testing, i.e. monitoring bacterial growth of samples with and without antibiotic [72][73][54][53]. Such methods are especially used when determining the minimum inhibitory concentration (MIC). The latter is the minimum concentration of an antibiotic needed to inhibit bacterial growth and thus stop further spreading of a bacterial inflammation.

Having shown in the previous chapter that bacterial growth can be detected with the IDA-setup, this chapter addresses the efficacy and speed of AST with the IDA-setup. In the first section, the scanning-configuration presented in Chapter 2.1.2 was used to determine the MIC of three different antibiotics (ampicillin, kanamycin and vancomcin) and two different bacterial species (*Escherichia coli* and *Bacillus subtilis*). The second section discusses the mobility analysis and the standard deviation of the short-term intensity fluctuations as potential early indicators for antimicrobial susceptibility.

## 5.1 Determining the Minimum Inhibitory Concentration

### Ampicillin

Ampicillin ($C_{16}H_{19}N_3O_4S$) is a $\beta$-lactam, broad-spectrum, semisynthetic penicillin [8][74]. It was discovered in 1958 and put to commercial use in 1961 by J.H.C. Nayler, F.P. Doyle and associates at the British company Beecham Laboratories [75][76]. It is used to treat infections by gram-negative (e.g. *Escherichia coli*) as well as gram-positive bacteria (e.g. *Staphylococcus aureus*) [74]. Since ampicillin belongs to the group of penicillins, it is an inhibitor of the cell wall synthesis. The antibiotic binds the enzyme transpeptidase, a penicillin-binding-protein (PBP), which is needed for the cross-linking of peptide chains with glycan chains during the cell wall formation [77][78]. As a result, the transpeptidase reaction is inhibited while the cell-wall synthesis continues [8]. The newly created cell wall is not cross-linked and thus very instable. In addition to this, the antibiotic-PBP-complex stimulates the release of autolysins which decompose the existing cell wall. As a result, differences in the osmotic pressure between the surrounding medium and the inside of the cell lead to cell lysis, i.e. the breakdown of the cell. A main difference between ampicillin and the natural penicillin (penicillin G), lies in ampicillin's ability to target gram-negative bacteria. The latter results from an amino group (NH2, Figure 5.1), which is not present in the original Penicillin G, and allows the ampicillin to enter the pores of the outer membrane of gram-negative bacteria [79].

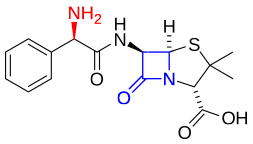


Figure 5.1: **Chemical structure of Ampicillin.** The $\beta$-lactam ring is marked in blue and the amino group, which allows ampicillin to target gram-negative bacteria, is marked in red.

In order to analyze the efficacy of AST-measurements with the IDA-setup, the MIC of Ampicillin was determined for the *E. coli* S-strain (BZB1011 [55]). For this, starter cultures of the *E. coli* bacteria were grown overnight at $37°C$ in Mueller Hinton Broth. The overnight cultures were diluted to an $OD_{600}$ of 0.05 and subsequently grown to an $OD_{600}$ of 0.2. The resulting suspension was then diluted once more by a factor of 50 in medium containing the ampicillin concentration of interest in order to start with approximately one to five bacteria above the 2D diffraction grating. All shown concentration-series were done with the same starting culture. The measurements of six different ampicillin concentrations were conducted simultaneously with the scanning-configuration for high-throughput (Section 2.1.2) using a $\mu$-slide VI 0.4 (Ibidi) with six parallel probing channels and at $T = 37°C$. The IDA-signal was recorded over one minute per concentration, whereupon the scanner moved the slide to the next channel. The resulting time-courses of the diffraction peak intensity-decrease $(1 - I(t)/I_0)$ are presented in Figure 5.2a. In order to deter-

mine the MIC, i.e. the minimum concentration showing no bacterial growth, a sigmoidal function was fitted to the diffraction peak intensity-decrease (average over one minute) plotted against the ampicillin concentration for each measurement cycle, as shown for t = 120 min in Figure 5.2b. The MIC was determined by calculating the intersection of the tangent of the fit's inflection point and the 0 horizontal line. This evaluation allows an estimation of the real MIC from the discrete sample of concentrations. The resulting MIC over the whole measurement is presented in Figure 5.2c. The latter shows that an approximate MIC of 2 mg/l can be determined in less than two hours. The $R^2$ values of the sigmoidal fit (Figure 5.2d) indicate that the fit can not be applied properly earlier than after approx. 100 minutes, as the diffraction peak intensity-decrease time-courses do not differ sufficiently before. The MIC of approx. 2 mg/l measured with the IDA-setup is in good agreement with literature values of 2 & 4 mg/l [80][81].

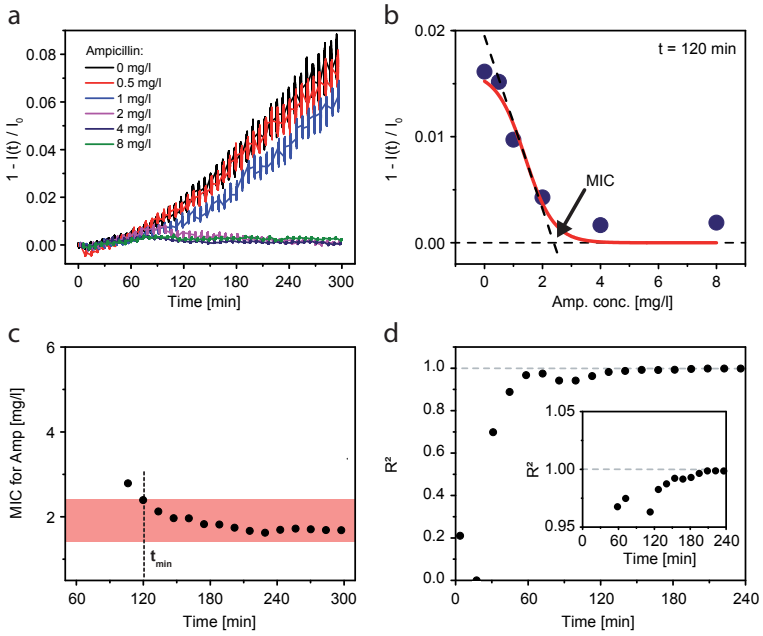


Figure 5.2: **Determining the MIC of ampicillin for *E. coli* bacteria with the IDA-setup. a)** Diffraction-peak intensity time-courses for six different ampicillin concentrations between 0 and 8 mg/l. **b)** Diffraction peak intensity-decrease (average over one minute) plotted against the ampicillin concentration for the measurement cycle at t = 120 min. A sigmoidal function was fitted to the data and the MIC is evaluated by calculating the intersection between the tangent line of the inflection point and the 0 horizontal line. **c)** Resulting determined MIC of approx. 2 mg/l for the whole measurement. The literature values are 2 & 4 mg/l [80][81]. **d)** $R^2$-values of the sigmoidal fit used to calculate the results shown in panel **c**. The $R^2$-values show that the fit does not adequately apply to the data prior to t = 120 min. Reproduced in part with permission from Nano Letters, in press. Copyright 2018 American Chemical Society.

### Kanamycin

Kanamycin ($C_{18}H_{36}N_4O_{11}$) belongs to the group of aminoglycosides, i.e. antibiotics containing amino acids. It was first isolated from *Streptomyces kanamyceticus* by Hamao Umezawa in 1957 and is of clinical importance for gram-negative bacteria [82]. Aminoglycosides bind to the 30S subunit of the ribosom and thus inhibit the synthesis of proteins needed for cellular growth [8][83]. Kanamycin is mainly used for the treatment of tuberculosis and as a reserve antibiotic for severe infections where first-line antibiotics do not show sufficient results.

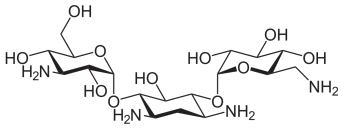


Figure 5.3: **Chemical structure of Kanamycin.** Structurally, Kanamycin consists of two amino sugars (left and right complexes) linked to an aminocyclitol ring nucleas by glycosidic bonds [84].

The MIC of kanamycin was determined for *E. coli* bacteria using the IDA-setup. Preparations of the concentration series were done analogously to the ampicillin measurements, but with kanamycin concentrations between 0 and 4 mg/l. The resulting diffraction peak intensity-decreases show a very small effect on the growth of *E. coli* for 0.25 mg/l and a moderate impairment on growth for 0.5 mg/l. Samples with a kanamycin concentration of 1 mg/l or higher showed no bacterial growth. Applying the dynamic MIC-determination analysis, as presented in Figure 5.2b, yields an MIC of approx. 1.25 mg/l after 120 minutes. The latter is in agreement with literature values which vary between 0.5 and 8 mg/l [80].

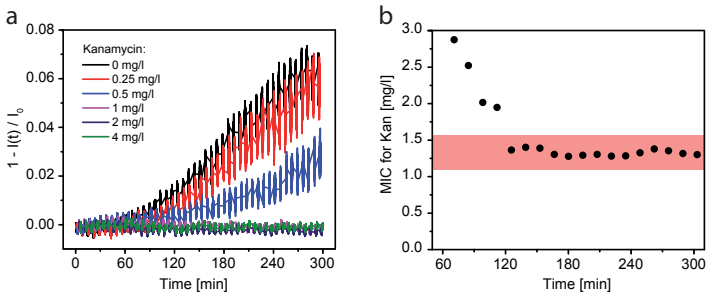


Figure 5.4: **Determination of the MIC of kanamycin for *E. coli* bacteria with the IDA-setup. a)** Diffraction-peak intensity time-courses for six different kanamycin concentrations between 0 and 4 mg/l tested on *E. coli* bacteria. **b)** The evaluation method presented in Figure 5.2b was used to determine an MIC of approx 1.25 mg/l after 120 minutes. Reproduced with permission from Nano Letters, in press. Copyright 2018 American Chemical Society.

### Vancomycin

Vancomycin ($C_{66}H_{75}C_{12}N_9O_{24}$) is a glycopeptide antibiotic and bactericidal against most gram-positive bacteria [85]. It was first isolated from *Streptomyces orientalis* in 1953 by E.C. Kornfield, who had obtained the organism from a dirt sample sent to him from Borneo by a missionary [86]. After reports of successful treatment of serious staphylococcal infections, it was approved by the US Food and Drug Administration and subsequently put to clinical use in 1958 [85]. Vancomycin binds to the D-alanyl-D-alanine tail of the muramylpentapeptide. The resulting complex cannot be processed by the enzyme glycosyltransferase, which results in an inhibition of the incorporation of murein monomers in the peptidoglycan chain [85]. As a results, the cell wall synthesis is inhibited.

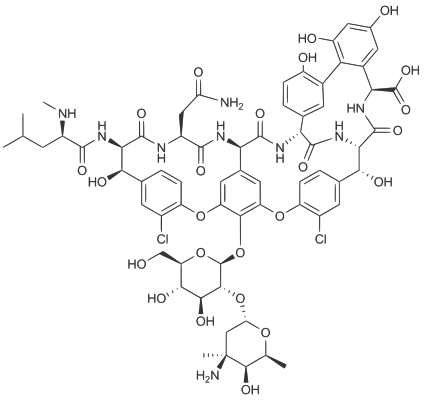

Figure 5.5: **Chemical structure of Vancomycin.** Vancomycin ($C_{66}H_{75}C_{12}N_9O_{24}$) has a molar mass of 1449.3 g/mol and inhibits the cell wall synthesis of gram-positive bacteria such as *Bacillus subtilis*.

Since Vancomycin is not effective against the gram-negative Escherichia coli used in the two previous AST measurements, the compound was analyzed using gram-positive Bacillus subtilis bacteria (NCIB 3610 strain [87]). Previously, an MIC of 0.25 mg/l was reported for W168 [88], which derives from the same bacterial strain as the analyzed NCIB 3610 [89]. For this reason, a measurement series with vancomycin concentrations between 0 and 1 mg/l was conducted with the IDA-setup. While similar growth curves with a slight delay of initial growth time were observed for 0, 0.064 and 0.12 mg/l vancomycin, bacteria in medium with 0.25 mg/l vancomycin or more did not grow. The dynamic MIC evaluation (Figure 5.2b) shows that an MIC of approx. 0.25 mg/l could be determined after approx. 180 minutes. Thus, the results are in good agreement with literature values [89].

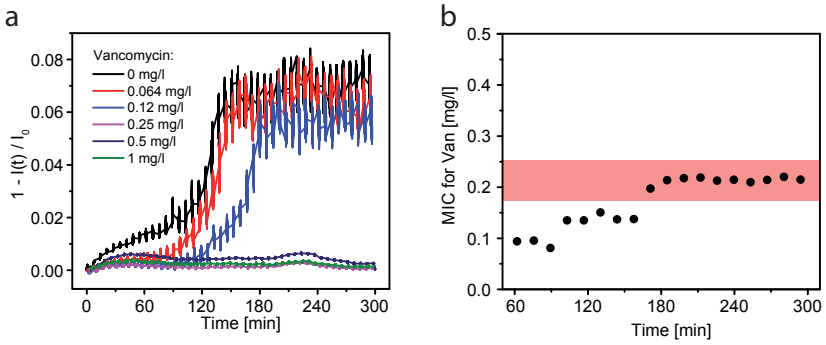


Figure 5.6: **Determination of the MIC of vancomycin for *B. subtilis* bacteria with the IDA-setup. a)** Diffraction-peak intensity time-courses for six different vancomycin concentrations between 0 and 1 mg/l tested on *Bacillus subtilis* bacteria. **b)** An MIC of approx. 0.25 mg/l could be determined after 180 minutes. The same MIC of 0.25 mg/l was reported in a study by Fang et al. [88] for *B. subtilis* W168, which derives from the same bacterial strain as *B. subtilis* NCIB3610 that was used in the presented measurement. Reproduced with permission from Nano Letters, in press. Copyright 2018 American Chemical Society.

## 5.2 Noise Analysis as a Potential Early Indicator for Antimicrobial Susceptibility

This section gives a discussion on the analysis of the short-term intensity fluctuations as a potential early indicator for susceptibility. The analysis of the noise of a signal has been previously utilized for antimicrobial susceptibility testing, e.g. by analyzing the variance of the deflection of a bacteria-covered cantilever [90]. Here, a decrease of the variance was measured due to a metabolism shock as a response to the antibiotic attack. For Interference Disturbance Analysis, the mobility analysis yielding the decay constant $\nu$ which is proportional to the diffusion coefficient (Chapter 3.4 and 4.4) as well as the standard deviation (SD) of the short-term intensity fluctuations are discussed as potential early susceptibility indicators. In order for the standard deviation to be independent of the current intensity and thus comparable throughout a growth measurement, it is normalized and calculated as:

$$Norm.\ SD(t_j) = \sqrt{\frac{1}{N-1}\sum_{i=j-N}^{j}\left(\frac{I(t_i) - I(\bar{t}_j)}{I(\bar{t}_j)}\right)^2}. \tag{5.1}$$

The normalized standard deviation was calculated over intervals of 5 seconds or N = 50 data points, resulting in 12 normalized SD values per acquisition interval of one minute. In Chapter 3, it was shown that the short-term intensity fluctuations arise due to small movements of the objects above the grating (Figure 3.3f). We found that the normalized SD is proportional to the amount of moving bacteria above the grating. To this end,

microscopy images of the growth measurement shown in Figure 4.2 were evaluated by calculating the absolute difference between two consecutive images ($P_i$ and $P_{i+1}$) and dividing this by the time between two images for the growth measurement (Figure 5.7).

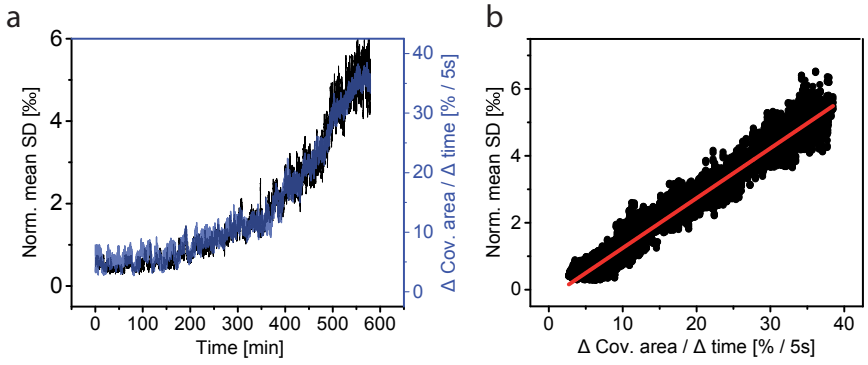


Figure 5.7: **Interpretation of the normalized standard deviation. a)** The normalized mean SD is a robust measure of the amount of moving bacteria above the grating ($\Delta$Cov. area / $\Delta$time). The latter was evaluated by calculating the absolute difference between two consecutive images ($P_i$ and $P_{i+1}$) and dividing this by the time between two images (here, 5 seconds). **b)** Direct correlation between the normalized mean SD, which was averaged over intervals of 1 minute, and the difference in covered area per time. The linear fit function is $f(x) = 0.15‰ \cdot x - 0.25$. Reproduced (modified) with permission from Nano Letters, in press. Copyright 2018 American Chemical Society.

### Ampicillin

When an antibiotic susceptibility test is measured simultaneously to a control measurement with the same starting concentration of bacteria but without antibiotic, the SD can act as an early indicator for antibiotic susceptibility, as shown in the following discussion. The normalized SD of the ampicillin concentration series from Figure 5.2 is shown in Figure 5.8a. It can be seen that the SD of all concentrations begins at the same value, while it increases for concentrations of 1 mg/l as well as smaller concentrations, and decreases for 4 and 8 mg/l as well as for 2 mg/l after a short increase. If one does not want to determine the MIC and is only interested in whether a given bacterium from e.g. an infection is susceptible to an antibiotic or not, it is appropriate to analyze the bacterias behavior in medium with the breakpoint value recommendations for the antibiotic concentration provided by the European Committee on Antimicrobial Susceptibility Testing (EUCAST) [80]. If growth of the bacteria is still measured with antibiotic concentrations higher or equal to the breakpoint value recommendation, it is considered as resistant against the respective antibiotic. Analyzing antibiotic susceptibility by comparing the behavior of bacteria in medium with breakpoint antibiotic concentrations to bacteria in medium without antibiotic has proven to be a rapid method for AST [54]. The breakpoint value recommendation for ampicillin and *E. coli* is 8 mg/l. A comparison of the

normalized SD (averaged over the one minute acquisition interval) for *E. coli* in MHB with and without 8 mg/l ampicillin for the first 60 minutes is presented in Figure 5.8b. The error bars mark the 99% confidence interval (CI) of the mean. It can be seen that the SD of the sample with ampicillin decreases by a factor of approx. 1.5, while the SD of the sample without antibiotic increases by approx. the same factor. It can further be observed that an antibiotic effect can be detected after 25 minutes, when the 99% confidence intervals can be distinguished.

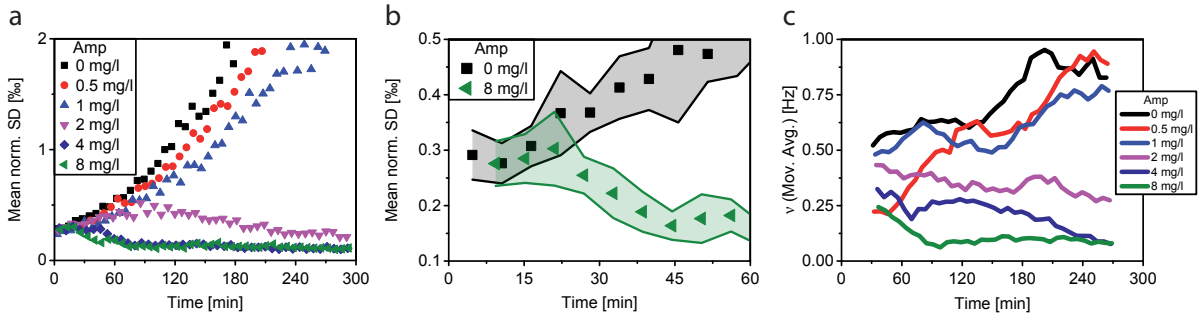


Figure 5.8: **Noise analysis of the short-term intensity fluctuations for an ampicillin concentration series. a)** Normalized standard deviation of short-term intensity fluctuations from IDA measurements of *E. coli* in MHB with ampicillin concentration between 0 and 8 mg/l. The SD is calculated over consecutive 50 data points, i.e. 5 seconds, and the average of 12 SD values per one-minute acquisition interval is calculated. **b)** Comparison of the mean normalized SD for bacteria in MHB with 0 and 8 mg/l. An antibiotic effect can be seen after 25 minutes, when the 99% confidence intervals (shaded error bands) can be distinguished. **c)** Dynamic analysis of the decay constant $\nu$ for six different *E. coli* growth measurements with ampicillin concentrations between 0 and 8 mg/l. A moving average over 10 data points, i.e. approx. 60 minutes, was applied. Reproduced in part with permission from Nano Letters, in press. Copyright 2018 American Chemical Society.

In addition to the SD, the short-term intensity fluctuations of the AST measurements were evaluated by applying the mobility analysis introduced in Chapter 3.4. The resulting time courses of the decay constant $\nu$ for the ampicillin measurements (Figure 5.2) are presented in Figure 5.8c. Because the mobility values tend to scatter, which could be observed in the mobility analysis of the growth measurement in the previous chapter (Figure 4.7d), a moving average over 10 data points or approx. 60 minutes was applied. The results show a mobility increase over time for concentrations lower than the MIC and a decrease for concentrations above it. While it is probable that the increase in mobility arises from a general vector flux of the bacterial ensemble due to a concentration or thermal gradient, a possible explanation for the decrease of mobility for concentrations above the MIC could be that the cells undergo lysis, resulting in smaller movements of

the biological material and smaller amplitudes of high-frequency intensity fluctuations. A further observation is that the initial $\nu$ is bigger, when the ampicillin concentration is higher (with an exception of 0.5 mg/l). Drawbacks of the mobility are that, due to the comparatively strong scattering of the values, long acquisition durations are needed, thus making it difficult for it to be useful as an early susceptibility indicator, especially when using a scanning configuration. However, it is useful for providing additional information on the mobility of bacteria, e.g. in order to analyze surface passivation (Chapter 4.4) or mobility-influencing antibiotics as will be discussed in Chapter 6.

As a control measurement, the response of an *E. coli* S-strain that was genetically modified in order to be resistant against ampicillin through an arabinose induced GFP plasmid (pBAD24-GFP [91]) was analyzed. For the susceptible strain, an antibiotic effect could be determined after 25 minutes (Figure 5.8b) and no increase of the mean normalized SD was measured over a total measurement duration of 600 minutes (Figure 5.9a). Contrary to this, the 99% confidence intervals of the resistant E. coli sample with and without the breakpoint recommendation concentration of ampicillin were indistinguishable over the same measurement duration (Figure 5.9b). Thus, it was confirmed that the ampicillin had no effect on the growth of the resistant strain. These results show that the standard deviation is a potential indicator for rapid susceptibility testing.

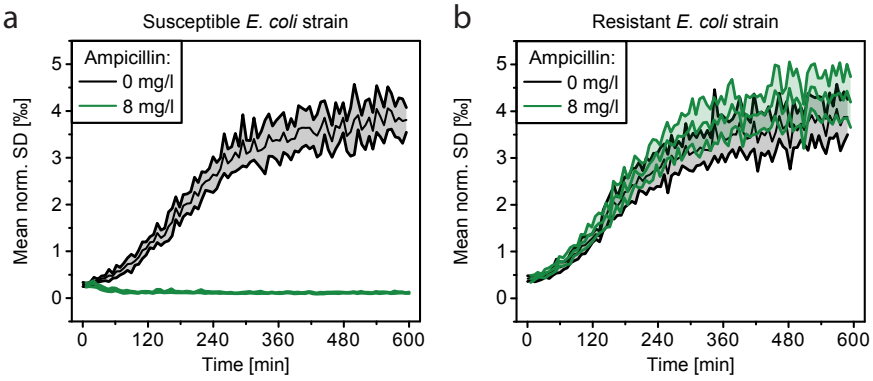


Figure 5.9: **Noise analysis of the short-term intensity fluctuations for an ampicillin concentration series. a)** Mean normalized SD for IDA measurements of the ampicillin susceptible *E. coli* S-strain (BZB1011) in MHB with 0 and with 8 mg/l ampicillin. The error bands show the 99% confidence interval of the mean. An antimicrobial effect can be detected after 25 minutes. After a decrease during the first 60 minutes, no increase of the SD was measured for the sample with 8 mg/l. **b)** Analogous measurement as in panel a but with a genetically modified, ampicillin resistant version of the S-strain. The 99% confidence intervals are indistinguishable for the total measurement duration of 600 minutes (10h). Reproduced (modified) with permission from Nano Letters, in press. Copyright 2018 American Chemical Society.

### Kanamycin

The analysis of the normalized SD for the kanamycin concentrations series shows a similar behavior as the diffraction peak intensity-decrease (Figure 5.10a). Samples with a kanamycin concentration higher than the MIC monotonously increase whereas those with a concentration lower than the MIC do not show an increase. A comparison of the normalized SD of the sample with and without 4 mg/l kanamycin shows that the respective 99% confidence intervals can be distinguished after less than 60 minutes (Figure 5.10b). The mobility analysis shows again an increase for the samples with kanamycin concentrations lower than the MIC as well as for 4 mg/l and no increase for 1 and 2 mg/l (Figure 5.10c). The smaller impact than for ampicillin could be explained by the fact that kanamycin does not induced cell-lysis, while ampicillin does. This explains why the mobility for higher concentrations than the MIC does not decrease, as the movement of the bacteria stays constant throughout the measurement.

Concerning a critical discussion of the stability of the IDA setup, empirical experiences during the experimental works for this thesis have shown that for the mobility analysis to yield clear results, a stable IDA setup is required. Several external influences such as the ventilation system of the incubators or incompletely sealed sample chambers can distort the mobility analysis. In addition to this, the measurement setups were often rebuilt or modified in order to analyze different questions of interest, thus leading to slightly inconsistent measurement-stabilities. An exemplary, seldom occurring instability of the diffraction peak intensity can be seen in Figure 5.10d. The plot shows a kanamycin concentration series for concentrations between 0 and 8 mg/l, i.e. the breakpoint value recommendation for *E. coli* and kanamycin [80]. A strong, periodic fluctuation of the diffraction peak intensity can be seen in the measurements with 1 - 8 mg/l. While the fluctuations assumingly occurred due to insufficiently sealed sample chambers or due to the ventilation system of the incubator, they only occurred to this degree in this measurement. An analysis of the normalized SD shows that despite the instabilities of the intensity, the sample with 0 mg/l and the sample with 8 mg/l can be distinguished in less than 40 minutes (Figure 5.10e). This shows that the normalized SD is a robust parameter, which is independent of long-term intensity fluctuations and setup instabilities. The mobility analysis presented in Figure 5.10f shows a strong increase for the sample without kanamycin, a small increase for 0.5 mg/l and a comparatively flat time course for the other samples. In addition to this, a trend to lower mobilities with increasing kanamycin concentrations is visible. This is roughly in agreement with the previous kanaymcin measurement. However, the normalized SD appears to be a more reliable indicator of antimicrobial susceptibility than the mobility analysis.

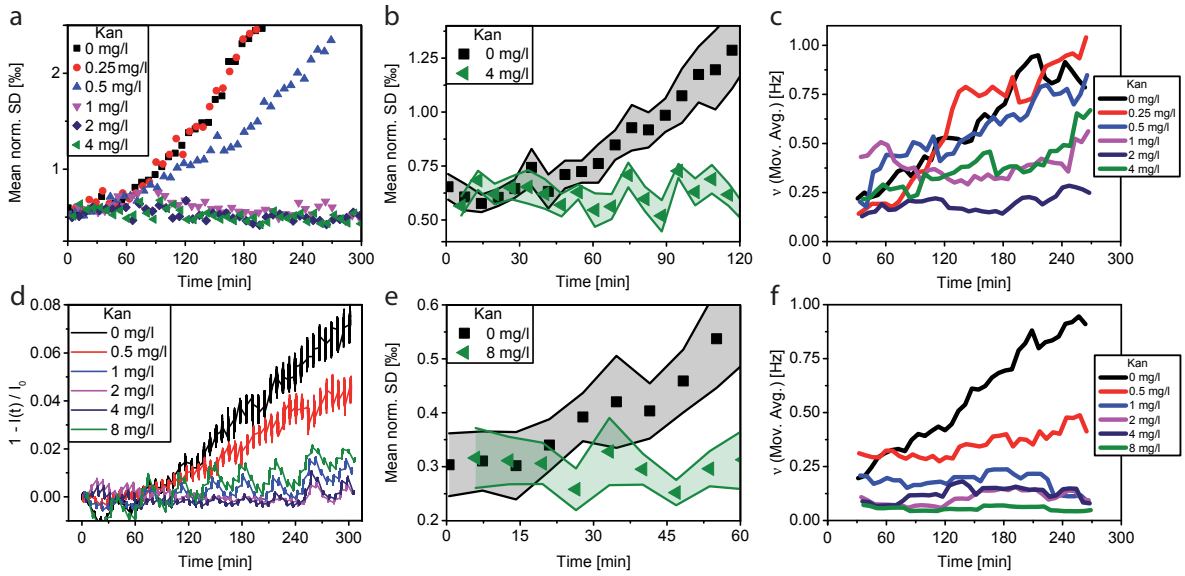


Figure 5.10: **Noise analysis of the short-term intensity fluctuations for two kanamycin concentration series.** **a)** Normed SD for the kanamycin concentration series shown in Figure 5.4. **b)** Comparison of the mean normalized SD for *E. coli* in MHB with 0 and 4 mg/l. The error bars mark the 99% CI. The response of the antibiotic treatment can be detected in less than 60 minutes. **c)** The mobility analysis shows a stronger increase of $\nu$ for 0-0.05 mg/l than for 1-4 mg/l. However, the results yield no conclusive additional information. **d)** Diffraction peak intensity-decrease for growth measurements of E. coli in MHB with kanamycin concentrations between 0 and 8 mg/l, showing strong intensity fluctuations arising from setup-instabilities. **e)** Comparison of the normalized SD for a sample without antibiotic and a sample with 8 mg/l kanamycin, i.e. the breakpoint value recommendation. Despite the long-term intensity instabilities, the antimicrobial susceptibility can be detected in the normalized SD after 38 minutes. **f)** Mobility analysis for the IDA-measurements shown in panel **d**. A moving average over 10 points or approx. 60 minutes was applied to the decay constant $\nu$. Reproduced in part with permission from Nano Letters, in press. Copyright 2018 American Chemical Society.

### Vancomycin

The mean normalized SD of the Vancomycin concentration series discussed in the previous section is shown in Figure 5.11a. The results show the same MIC as the diffraction peak intensity-decrease analysis. For vacomycin and *B. subtilis*, there is no breakpoint value recommendation by the EUCAST. For this reason we used 1 mg/l vancoymcin for susceptibility testing, which is the highest concentration from the MIC determination series where no growth was visible over the duration of the measurement. As a reference: the breakpoint value recommendation for vancomycin and *S. aureus* is 2 mg/l[80]. The comparison of the normalized SD of a sample with and without 1 mg /l vancomycin shows that an antibiotic effect could be detected after 29 minutes, as after that time point the 99% confidence intervals could be distinguished (Figure 5.11a). An analysis of the mobility of the MIC determination concentration series shown in Figure 5.6 yields no considerable additional information (Figure 5.11c).

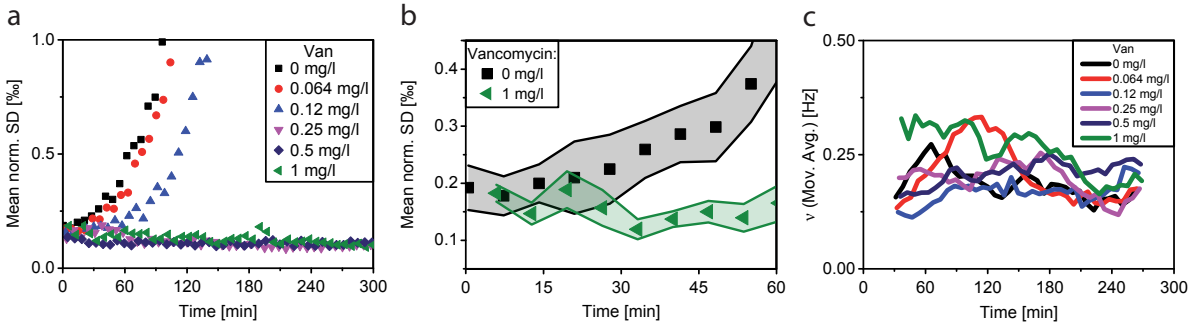


Figure 5.11: **Noise analysis of the short-term intensity fluctuations of a vancomycin concentration series. a)** Mean normalized SD of the short-term intensity fluctuations from IDA measurements of *B. subtilis* in MHB with vancomycin concentrations between 0 and 1 mg/l. **b)** Comparison of the mean normalized SD for the sample with and without 1 mg/l vancomycin. The error bars mark the 99% confidence interval of the mean. An antibiotic effect could be detected after 29 minutes, as this marks the timepoint where the 99% confidence intervals could be distinguished. **c)** The mobility analysis shows no considerable additional information. Reproduced in part with permission from Nano Letters, in press. Copyright 2018 American Chemical Society.

In addition to a susceptibility test of *B. subtilis* and vancomycin in MHB, the standard medium used for AST, a susceptibility measurement was conducted using a minimal medium, M63, in which *B. subtilis* grow slower and in total to a smaller amount due to the restrained nutrients (Figure 5.12a). For this measurement, the breakpoint recommendation concentration for vancomycin and *S. aureus* was used (2 mg/l). Despite the slower growth in M63 medium, an antibiotic effect could be determined in less than 60 minutes from the SD analysis. Again, no increase of the SD was detected during the total measurement duration of 600 minutes.

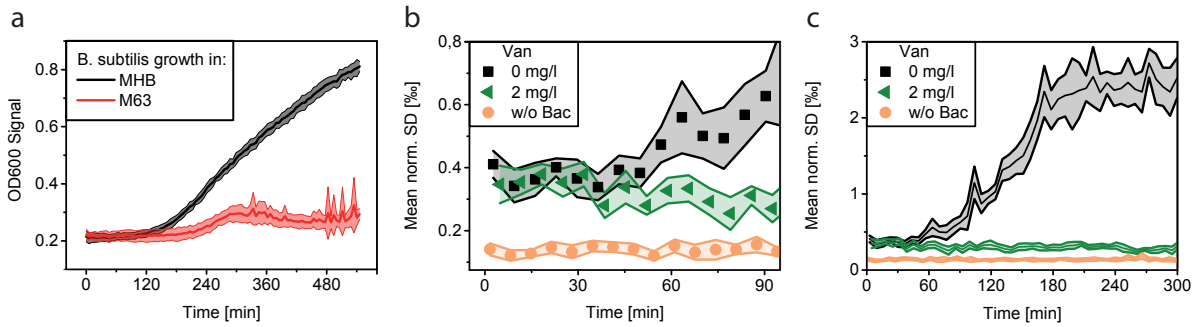


Figure 5.12: **Susceptibility testing in minimal medium. a)** $OD_{600}$ plate reader measurement of *B. subtilis* in MHB (black) and M63 minimal medium (red). The same starting concentration as for the IDA measurements was used, but higher volumes of 500 µl per sample. It can be seen that the growth in M63 medium is delayed by approx. 120 minutes and leads to a small increase of OD compared to growth in MHB. The bold lines show the average of six measurements each and the error bands a 95% confidence interval. **b)** Normed SD of IDA measurements of B. subtilis in M63 minimal medium with and without 2 mg/l vancomycin. The 99% confidence intervals could be distinguished after 29 minutes. **c)** Over the total measurement duration of 300 minutes, no increase of the SD for the sample with 2 mg/l vancomycin was detected.

In summary, it was shown in this chapter that the IDA method could be used to determine the MIC of three different antibiotics and two different bacterial species in less than 2-3 hours. In addition to this, the analysis of the normalized SD can act as an early susceptibility indicator. Here, simultaneous measurements of samples without antibiotic and with breakpoint value recommendations concentrations provided by the EUCAST showed that an antimicrobial effect could be detected in less than 30-60 minutes in MHB and in minimal M63 medium. A further advantage of the normalized SD is that it is stable against measurements instabilities such as laser intensity instabilities arising temperature variations, which can occur when the door of an incubator is opened in order to place a sample inside the setup. In the future, the stability of the SD and the intensity could be improved by, e.g., vibration-damping of the laser and the grating, possibly leading to quicker AST results. The mobility analysis yields additional information which is especially of interest for mobility decreasing antibiotics, as will be shown in the next chapter.

# Chapter 6

# Photoswitchable Antibiotic

With the efficacy of conventional antibiotics decreasing due to an increase of resistance, novel approaches to control bacterial growth are highly sought-after. One promising approach is the use of photoswitchable antibiotics, i.e. a molecule that can be switched between a biological active and inactive state through illumination with a given wavelength [92][93]. Such photoswitchable antibiotics allow a high spatio-temporal control and can yield several further advantages. For instance, they can be used in order to reduce the high occurrence of antibiotics in the environment [94][95], a problem originating from an extensive use of antibiotics in healthcare [96] and agriculture [97]. This is done by designing the molecule in such a way that the photo-activated state has an antibiotic effect which is lost after thermal relaxation to the ground state. Should the antibiotic find its way into the environment, it is harmless and can not lead to an increase in antibiotic resistance. An according quinolone antibacterial agent has been presented in the recent past [98]. Further applications include photopharmacological inhibitors of amidohydrolase enzymes, photoswitchable compounds based on the antibiotics nalidixic acid and ciprofloxacin [99] as well as growth-selection of a single bacterial strain out of a mixture of multiple strains by illumination with the appropriate wavelength [100].

In this chapter, a novel, photoswitchable antibiotic "Azo-PC" is analyzed with the IDA-setup. The antibiotic was designed as an optical control of bacterial migration, thus being an optimal candidate for IDA-measurements. The chemical properties and principle of action of the compound are discussed in the first Section 6.1. In the following Section 6.2, an extension to the high-throughput setup (Chapter 2.1.2) is presented, which was needed for the photoswitchable measurements (and allows an even higher throughput as will be discussed in more detail in Chapter 7). The IDA-results are presented in Section 6.3. Here, the influence of the Azo-PC in its active and non-active state on bacterial growth and mobility are analyzed. The work presented in this chapter was a collaboration with the group of Prof. Dirk Trauner (New York University), especially his PhD student Peter Ruehmann as well as with Julian Aschauer (LMU) within the scope of his master thesis [101].

## 6.1 FtsZ-Inhibitor Azo-PC

The compound analyzed in this chapter, "Azo-PC", was designed and synthesized by the group of Prof. Trauner (NYU) as an optical control of bacterial migration based on the model of PC190723 [102][103]. The latter is a synthetic, small-molecule antibacterial that prevents cytokinesis [102]. The PC190723 antibiotic targets FtsZ, a cell division protein which forms single-stranded filaments that are important for the formation and constriction of the cytokinetic ring [104][105]. The benzamide derivative PC190723 molecule enhances the assembly of purified FtsZ into filaments and bundles, thus leading to mislocalized FtsZ foci and resulting in inhibition of cell division [104][102][106]. The PC190723 and Azo-PC are expected to have an effect on bacterial migration and mobility, as the inhibition of FtsZ depolymerization not only leads to the already mentioned subsequent prevention of cytokinesis, making it more difficult for the flagellum to move the exceptionally elongated bacterium, but also leads to a less dynamic cytoskeleton [104][106]. It is important to note that while PC190723 targets the FtsZ in *Staphylococcus aureus* and *Bacillus subtilis*, it does not affect *Escherichia coli*[104]. This means that measurements with *Escherichia coli* serve as a reliable control when analyzing the Azo-PC.

Concerning the chemical structure, the Azo-PC compound is an azobenzene version of PC190273. The main difference between both compounds is that, for the Azo-PC, the R1-O-C-R2 junction is replaced by a R1-N=N-R2 junction, i.e. the functional group of diazene (Figure 6.1) [107][93]. The diazene junction exists as two geometric isomers: the trans- (Figure 6.1, "trans-Azo-PC, active") and the cis-state (Figure 6.1, "cis-Azo-PC, inactive") [108]. The photoresponsive molecule can be switched between the thermodynamically more stable trans-state to the cis-state via UV light, also known as photoisomerization [109]. Relaxation to the trans state can be achieved by illumination with a different wavelength as well as spontaneously, by thermodynamical relaxation.

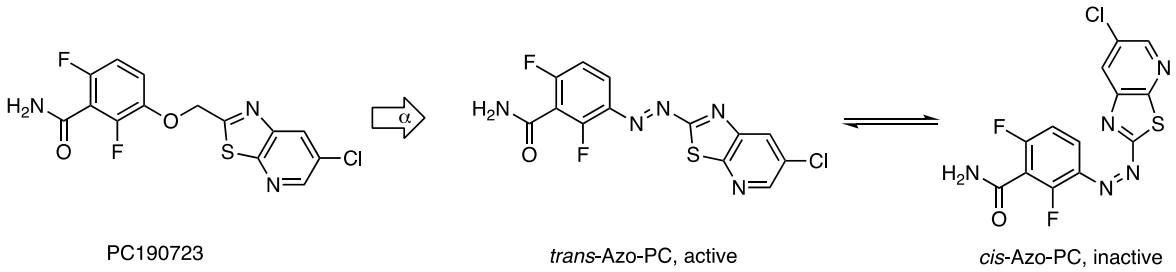


Figure 6.1: **Chemical structure of PC190723 and Azo-PC in the trans- and cis-state.** Azo-PC is modeled after the cytokinesis inhibitor PC190723. The thermodynamically stable trans-state is expected to be biologically active, as its structure is similar to that of PC190723. The respective photoisomeric counterpart, the cis-state, is expected to be biologically less active, as it should not fit in the binding pocket of the target FtsZ protein. Image provided by Peter Ruehmann (NYU).

A switch between the two states is accompanied by a big change in geometry and polarity [110]. The effectiveness of a given drug is strongly dependent on its pharmacodynamic and pharmacokinetic properties [111][112], such as polarity and size of the compound. Being able to control these properties with the help of a light-source allows a spatio-temporal manipulation of a drug's efficacy. The Azo-PC compound was designed to show similar activities to the PC190273 compound in the trans-state (Figure 6.1). Thus, the trans-state is the biologically active state, with the cis-state being less active, as it is proposed that it does not fit in the binding pocket of the FtsZ protein. Switching from the trans- to the cis-state can be achieved by illumination with a wavelength of $\lambda = 390\,\text{nm}$ (Figure 6.2a, purple line). Relaxation to the trans-state is feasible with $\lambda = 500\,\text{nm}$ light (Figure 6.2a, cyan line) or spontaneously through thermodynamical relaxation. The cis-state of the Azo-PC compound has a half-life of 4 minutes at a temperature of $T = 37°C$ (Figure 6.2b).

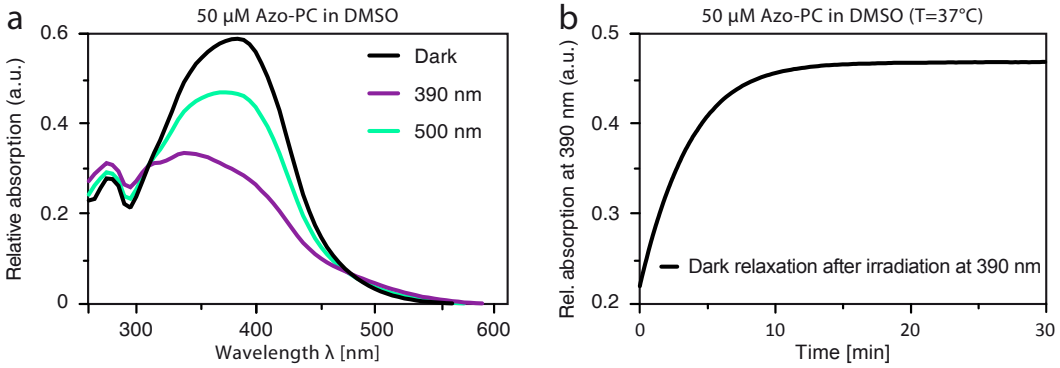


Figure 6.2: **Azo-PC absorption spectrum and relaxation half-life. a)** Absorption spectrum of Azo-PC without prior illumination (dark, black line) and after illumination with 390 nm (purple line) and 500 nm (cyan line). **b)** Absorption at 390 nm after prior illumination with 390 nm, showing the thermodynamical relaxation of the cis-state back to the trans-state at $T = 37\,°C$ with a half-life of 4 minutes. Data provided by Peter Ruehmann (NYU).

## 6.2 High-Throughput Scanning Configuration with a Fiber Coupler

When measuring concentration series of the Azo-PC compound, it is desirable to measure the trans- and cis-state simultaneously using the same starting bacterial culture, thus ensuring maximum comparability between both states. To be able to do so, the high-throughput setup described in Chapter 2.1.2 was extended for an even higher throughput (Figure 6.3a) and UV-LEDs were added in order to control the switching mechanism (Figure 6.3b) [101]. A slide holder was designed that allows the simultaneous measurement of four sample slides in the size of a regular microscope slide (75 x 25 mm). To

maintain a high measurement duration per well, the laser beam ($\lambda = 635\,\text{nm}$) was split up in four beams using a 630 nm 1x4 Narrowband Fibre Optic Coupler from Thorlabs, optimized for coupling wavelengths with an operating range of $630 \pm 15\,\text{nm}$ (Figure 6.3a, beam splitter) [101]. Therefore, the laser beam was guided into a glass fiber (Thorlabs HP600 single mode fiber, wavelength range from 600 to 700 nm) using a Thorlabs Fiberport Coupler (Figure 6.3a, coupler). After the beam splitter, the four resulting beams were collimated using a Thorlabs Fixed Focus Collimator (Figure 6.3a, collimator). The latter employs an aspheric lens to generate a beam diameter of 1.5 mm. Each beam was aligned to a 2D-grating and a first order diffraction peak of each resulting diffraction pattern was acquired with a CMOS-camera. For simultaneous concentration series of the trans- and cis-state of Azo-PC, two Ibidi µ-Slides VI 0.4 with six different Azo-PC concentrations each, were measured. In order to measure both states simultaneously, the cis-slide was illuminated with three LEDs with wavelengths $\lambda = 390\,\text{nm}$ and an emission angle of 110° for an even illumination of the sample (Figure 6.3b). Each LED has a power of approx. 4 mW. To shelter the trans-slide from the UV-light, a plastic plate was positioned between both slides as a light barrier (Figure 6.3b).

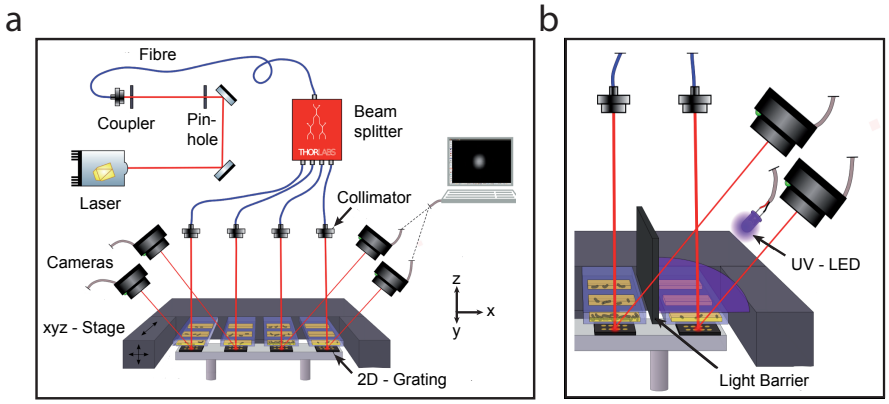


Figure 6.3: **Extension to the scanning-configuration for higher throughput and measurements of photoswitchable compounds. a)** In order to measure up to four slides with six different concentrations each, the laser was split up into four beams. For this, the beam was coupled into a single mode fiber and was then split in to four beams through passive fiber coupling. The resulting beams were collimated and aligned to a respective 2D-grating. **b)** During simultaneous measurements of the trans- and cis-state, the cis-sample was illuminated with UV-LEDs ($\lambda = 390\,\text{nm}$), while the trans-sample was sheltered from the UV-light by a plastic barrier. Images taken from [101].

## 6.3 Azo-PC: IDA-Results

For the preparation of the measurements with Azo-PC as well as the respective controls, *Bacillus subtilis* bacteria (NCIB 3610-strain [87]) were grown over night in Mueller Hinton Broth (MHB). The overnight culture was subsequently diluted in MHB to obtain a

turbidity of $OD_{600} = 0.1$. The substance of interest (e.g. Azo-PC) was diluted in MHB in order to receive the desired concentration. The bacteria from the $OD_{600} = 0.1$ suspension were diluted by a factor of 50 in the respective substance-solutions and were shaken using a tabletop vortex mixer. As a sample holder, Ibidi µ-Slides VI 0.4 were used. Of each sample-suspension, 30 µl were given inside a channel of the slide, thus filling the middle compartment of the latter. The wells at each end were sealed using 15 µl anti-evaporation oil. In order to achieve a high ratio of cis:trans molecules in the cis-sample from the beginning of the measurement on, the preparations were done with turned-off room lights and under illumination with 390 nm UV-light. It is important to mention that a ratio of 100% cis-molecules after photoisomerism is unrealistic due to thermal relaxation and in the best case a ratio of approximately 85:15 for cis:trans is to be expected [98].

### 6.3.1 Azo-PC: Growth Analysis

Since the Azo-PC compound is dissolved in DMSO, which is known to have an antimicrobial effect on bacterial growth in higher concentrations [113], a control measurement of the DMSO tolerability for the used *Bacillus subtilis* strain was done using the IDA-setup and the results are shown in Figure 6.4. The intensity is averaged over the one-minute measurement duration per sample. No difference in the growth behavior between the reference measurement without DMSO and DMSO concentrations of up to 4% was observed. This is in good agreement with previous studies of the effect of solvents on growth of different bacterial strains [114]. The DMSO concentration for the following Azo-PC measurements was consistently set to 3.33% for all samples.

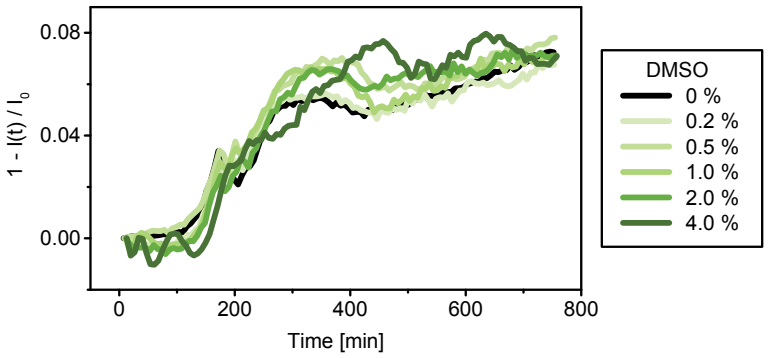


Figure 6.4: **Analysis of the DMSO tolerance for *Bacillus subtilis* (NCIB 3610).** Diffraction peak intensity-decrease for growth measurements of *Bacillus subtilis* in MHB with DMSO concentrations between 0% and 4.0%. No influence on the bacterial growth was observed for the given DMSO concentrations. In a consequence, the DMSO-concentration was consistently set to 3.33%, i.e. the DMSO concentration of the respective highest Azo-PC concentration analyzed.

In order to analyze the effect of Azo-PC on Bacillus subtilis bacteria, growth measurements were conducted with in total eleven different Azo-PC concentrations between

0 mg/l and 100 mg/l for the trans- and cis-state simultaneously (two measurements with 0-100 mg/l, Figure 6.5 and A.1; and two measurements with 0-16 mg/l, Figure A.2 and A.3). Concerning the peak intensity-decrease, an increasing delay of the growth with increasing Azo-PC concentration could be observed for both the trans- and the cis-state. However, this antibacterial effect was more pronounced for the biologically active state (trans), with no visible growth for 100 mg/l during the duration of the measurement. The growth measurements with the cis-state of the Azo-PC compound showed growth for all concentrations, although the two highest concentrations show a strong delay of the growth with only a small decrease of diffraction peak intensity.

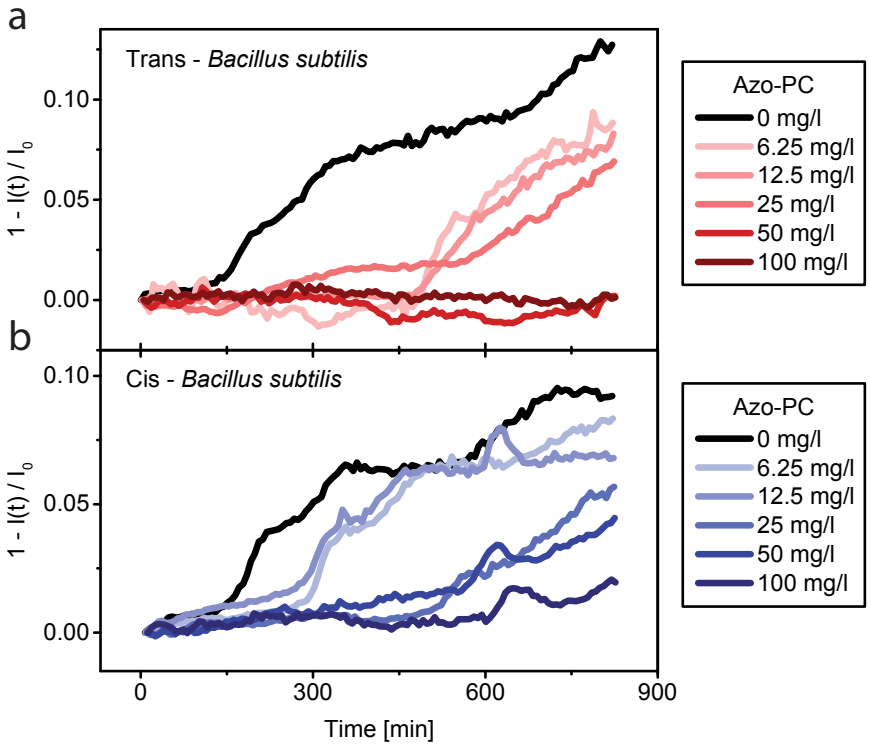


Figure 6.5: **Influence of Azo-PC in the trans- and cis-state on the growth behavior of *Bacillus subtilis*.** **a)** Normalized diffraction peak intensity-decrease for growth measurements of *B. subtilis* with Azo-PC concentrations between 0 mg/l and 100 mg/l in the biologically active trans-state. An antibacterial effect can be seen, as the growth is increasingly delayed with increasing Azo-PC concentration. **b)** Analogous growth measurements of *B. subtilis* as in panel **a** but with $\lambda = 390$ nm illumination, resulting in photoisomerization of Azo-PC to the non-active cis-state. The estimated cis:trans ratio is 85:15. A delay of the bacterial growth is observed as well, however less pronounced as for the trans-state.

The effect of delayed growth was quantified by fitting a logistic function,

$$y(t) \;=\; \frac{y_{max}}{1 + e^{-\mu(t-t_c)}} + c, \tag{6.1}$$

to the exponential growth phases of the growth measurements and evaluating the critical growth time $t_c$, i.e. when the fit curve has reached half of its maximum (Figure 6.6a). In order to evaluate the delay of growth for a given Azo-PC concentration, the difference between the respective critical growth time and the critical growth time of the respective growth measurement without Azo-PC was calculated. This is demonstrated for 12.5 mg/l (Cis) in Figure 6.6a, where the growth delay is calculated as $\delta t_c \;=\; t_{c,12.5} - t_{c,0}$. The resulting growth delays $\delta t_c$ for the eleven measured Azo-PC concentrations for the trans- and cis-state are presented in Figure 6.6b. The analysis elucidates the increased delay of bacterial growth for samples with Azo-PC in the trans-state compared to the cis-state. It can be seen that the growth delay $\delta t_c$ increases stronger for smaller than for bigger Azo-PC concentrations. For this reason, the data was fitted with a logarithmic function,

$$y(x) \;=\; a - b \cdot ln(x + c), \tag{6.2}$$

with y being the growth delay $\delta t_c$, x the Azo-PC concentration in mg/l, and a, b, c fit parameters. The logarithmic fit-function to the trans-state is

$$y(x) \;=\; -14.9 + 159.8 \cdot \; ln(x + 0.2), \tag{6.3}$$

and the respective fit-function to the cis-state is

$$y(x) \;=\; -264.5 \;+\; 161.4 \cdot \; ln(x + 4.4). \tag{6.4}$$

The growth delay $\delta t_c$ for the cis-state fit-function at 100 mg/l Azo-PC is equal to the $\delta t_c$ for the trans-state fit-function at an Azo-PC concentration of 20.5 mg/l, thus showing that a cis:trans-ration of approx. 20:80 appears reasonable.

In addition to the delay-analysis, the difference between the critical growth times for the respective trans- and cis-state, $\Delta t_c$, was determined for each concentration (Figure 6.6a and c). The results show almost no difference in $\Delta t_c$ for concentrations smaller than 4 mg/l and a maximum $\Delta t_c$ of approx. 300 minutes. The purple line in Figure 6.6c shows a logarithmic fit function $y(x) \;=\; 92.4 + 34.4 \cdot ln(x - 0.9)$.

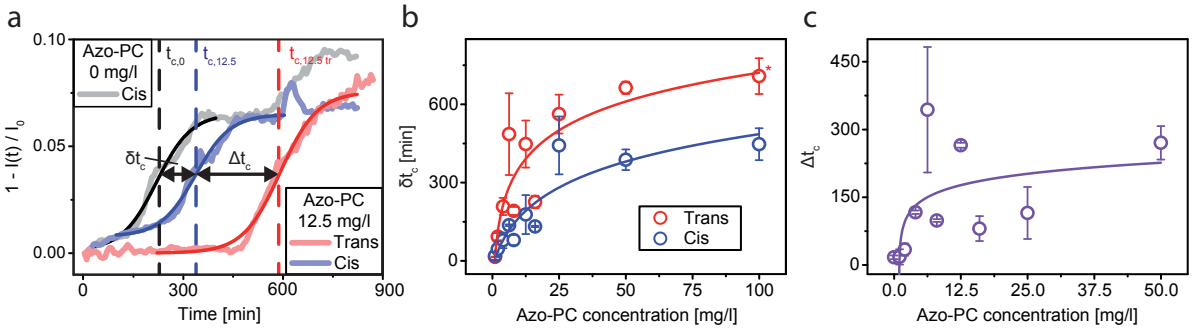


Figure 6.6: **Critical growth times $t_c$, growth delay $\delta t_c$ and difference in critical growth times $\delta t_c$ for the trans- and cis-state of Azo-PC measurements with *B. subtilis*.** **a)** A logistic fit was fitted to the exponential growth phases for 24 growth measurements of in total 11 different Azo-PC concentrations. The time point of growth was determined from the critical growth time $t_c$. The growth delay, compared to the respective growth curve without Azo-PC, was determined as $\delta t_c = t_{c,Azo-PCconc.} - t_{c,0\,mg/lAzo-PC}$. Further, the difference in time points of growth for the trans- and cis-state of a given Azo-PC concentration was evaluated as $\Delta t_c = t_{c,Trans} - t_{c,Cis}$. **b)** The growth delay $\delta t_c$ shows a stronger delay of growth for the trans-state (red) than for the cis-state (blue). The respective logarithmic fit-functions are $y(x) = -14.9 + 159.8 \cdot ln(x + 0.2)$ for the trans-state and $y(x) = -264.5 + 161.4 \cdot ln(x + 4.4)$ for the cis-state. For an Azo-PC concentration of 100 mg/l in the trans-state (marked by an *), no growth was visible during the duration of the measurement, so the total duration was used as a minimum $t_c$. **c)** The difference of critical growth times $\Delta t_c$ shows almost no effect for Azo-PC concentrations smaller than 4 mg/l and a maximum $\Delta t_c$ of approx. 300 minutes. The logarithmic fit function is $y(x) = 92.4 + 34.4 \cdot ln(x - 0.9)$. All points mark the average values with the respective standard deviations.

Control measurements with *Escherichia coli* bacteria, which are non-susceptible to the model-molecule PC190723 [104], were conducted with Azo-PC concentrations between 0 and 16 mg/l, resp. 32 mg/l (Figure A.4 and 6.7). The results showed no delay in the growth for the trans-state of the Azo-PC and once no delay (Figure A.4) as well as once a small delay for the cis-state (Figure 6.7). While the small effect on the cis-state is of interest for potential further analysis, it is the opposite effect as seen for measurements with *B. subtilis* and thus confirms the hypothesis of the trans-state of the photoswitchable Azo-PC operating similar to the PC190723 molecule.

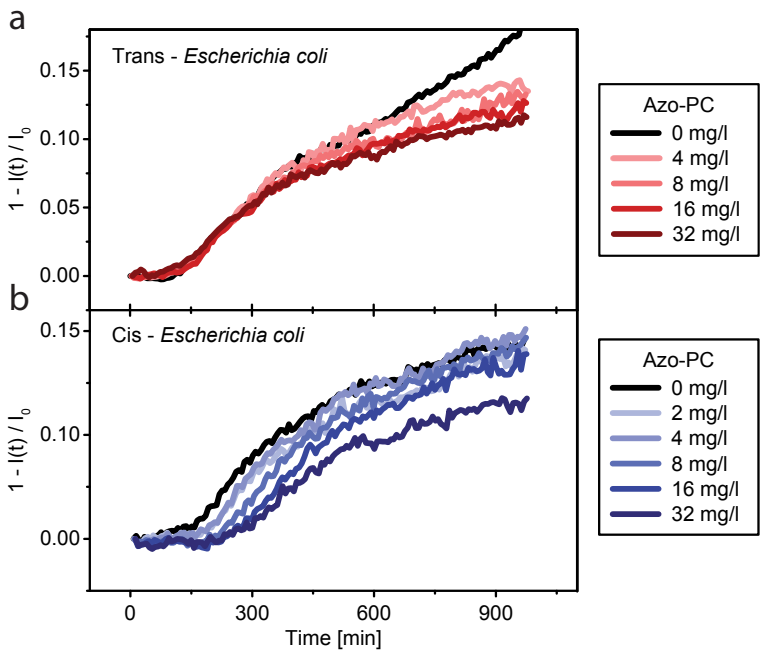


Figure 6.7: **Influence of Azo-PC in the trans- and cis-state on the growth behavior of *Escherichia coli*. a)** Growth measurements of *E. coli* with 0-32 mg/l Azo-PC were conducted as a control, since *E. coli* are non-susceptible to the model-molecule of the Azo-PC trans-state. The results for Azo-PC (trans-state) show no influence of the growth of *E. coli* and are thus in good agreement with literature on PC190723 [104]. **b)** A small delay of growth could be measured for the cis-state, which is the opposite effect as shown for *B. subtilis*.

### 6.3.2 Azo-PC: Mobility Analysis

The Azo-PC compound was designed as an optical control for bacterial migration and mobility. In order to assess its effectiveness in this matter, the 24 growth measurements with 11 different Azo-PC concentrations were analyzed using the mobility analysis presented in Chapter 3.4 and 4.4. The dynamic analysis of the resulting decay constants $\nu$, which are proportional to the diffusion coefficient, for the growth measurements shown in Figure 6.5 is presented in Figure 6.8. The plots show a moving average over 40 data points. It can be seen for both states that a higher concentration of Azo-PC leads to a smaller decay constant $\nu$ (with 6.25 mg/l in the trans-state being the only outlier). In addition to this, an increase in mobility during the beginning of the experiment is observed for smaller concentrations (6.25 mg/l and 12.5 mg/l), which may be caused by an initial lag phase, leading to a smaller mobility of the bacteria, or due to the presence of an overall velocity field arising from a nutrient gradient [115]. The intermediate concentrations (25 mg/l and 50 mg/l) show a decrease over time and the highest concentration (100 mg/l) results in a low mobility throughout the measurements. The measurements with the trans-state show a smaller decay constant $\nu$ than their cis-state counterparts. The differences in mobility between the trans- and cis-state are discussed in more detail

in Figure 6.9. The mobility analysis of the control measurements with *Escherichia coli* shows no influence of the Azo-PC in trans-state on the decay constant $\nu$ (Figure 6.8c and A.5). During the beginning of the experiments, a slight increase in mobility is observed, possibly arising from a gradient of nutrients or temperature [115]. An overall velocity field was observed during a majority of bacterial growth measurements with the microscope-setup. After the slight increase, the decay constant $\nu$ stays constant throughout the measurement. Measurements with *E. coli* and the cis-state of Azo-PC show a similar course of the decay constant $\nu$ but with a small concentration-dependent decrease of initial mobility. The larger effect of the cis-state is again contrary to the effect observed with the susceptible *B. subtilis* and is in agreement with the growth delay discussed in Figure 6.7.

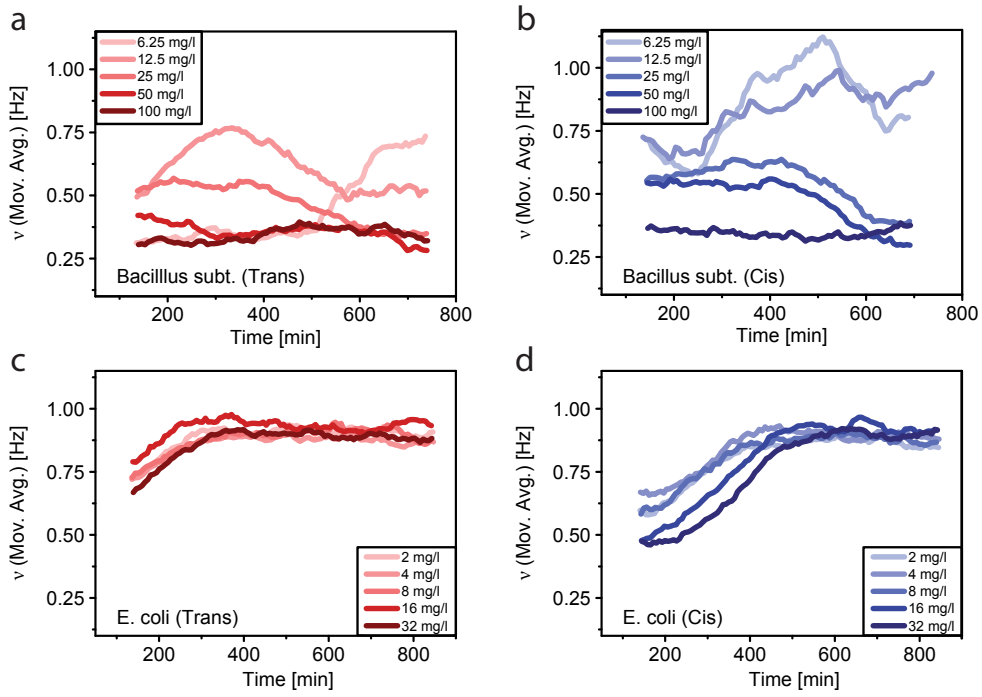


Figure 6.8: **Dynamic analysis of the mobility for Azo-PC measurements of susceptible and non-susceptible strains. a)** Moving average of $\nu$ over 40 data points for growth measurements of *B. subtilis* with Azo-PC concentrations of 0 to 100 mg/l in the trans-state. Samples with low compound concentrations show an initial increase and a generally higher mobility than samples with higher concentrations. **b)** Mobility analysis of samples with the cis-state of Azo-PC analogous to **a**. The dynamic analysis shows a similar course of the mobility as with the trans-state, but with higher $\nu$-values. **c)** Moving average of $\nu$ over 40 data points for Azo-PC trans-state measurements with *E. coli*. All samples show a slight initial increase, but no dependence of the mobility on the Azo-PC concentration. **c)** Analogous E. coli measurement with Azo-PC in the cis-state. The analysis shows a similar behavior as with the trans-state, with a small initial effect on the mobility, which is contrary to the effect observed with *B. subtilis*.

In order to quantify the effect of Azo-PC on the mobility, the decay constant $\nu$ was averaged over the whole duration for each of the 24 *B. subtilis* and 12 *E. coli* measurements (mean decay constant $\nu$, Figure 6.9). The analysis of the mean decay constant $\nu$ for Azo-PC measurements with *B. subtilis* (see Figure 6.9) shows a decrease of mobility with increasing compound concentration. The samples that were illuminated with 390 nm light, resulting in the cis-state of the compound, show a smaller decrease in mobility than the samples with the biologically active trans-state. Similar to the analysis of the growth delay in Figure 6.6b, the mean decay constant $\nu$ decreases logarithmically with the Azo-PC concentration. The respective fit functions are $y(x) = 1.08 - 1.13 \cdot ln(x + 3.89)$ for the cis-state and $y(x) = 0.72 - 0.09 \cdot ln(x - 0.48)$ for the trans-state. Again, the mean decay constant $\nu$ of measurements with 50 and 100 mg/l Azo-PC in the cis-state show a similar value as respective trans-measurements with a fifth of the concentrations, thus confirming a cis:trans-ratio of approx. 80:20. The mobility analysis of the control measurements with non-susceptible *E. coli* bacteria shows no influence of the Azo-PC compound on the decay constant $\nu$ (Figure 6.9b). A comparison of the mean decay constant $\nu$ of samples with 0 mg/l Azo-PC for the DMSO control, the *E. coli* control and the Azo-PC measurements shows that the IDA-method allows for compatible mobility measurements. The respective mean $\nu$ values are $0.85 \pm 0.21$ Hz (DMSO), $0.82 \pm 0.04$ Hz (E. coli), $0.86 \pm 0.17$ Hz (Azo-PC, trans-state) and $0.92 \pm 0.10$ Hz (Azo-PC, cis-state).

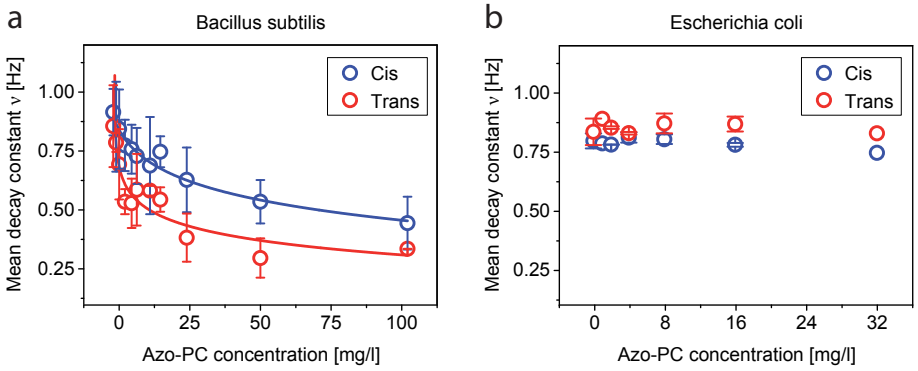


Figure 6.9: **Mean mobility $\nu$ vs. Azo-PC concentration. a)** Mobility analysis of *B. subtilis* growth measurements with Azo-PC in the cis- and trans-state. Both states show a logarithmic decrease of mobility with Azo-PC concentration, while the bioactive trans-state shows a stronger effect. **b)** The mobility analysis of growth measurements with Azo-PC in cis- and trans state and *E. coli* bacteria, which are non-susceptible to the model compound PC190723, showed no influence on the mobility in both states.

In summary, this chapter has presented a novel, photoswitchable antibiotic compound "Azo-PC" which was designed as an optical control of bacterial migration. The analysis with the IDA-method could show a logarithmically increasing delay of the growth with increasing compound concentration. In addition to this, a logarithmic decrease in mobility (mean decay constant $\nu$) with increasing compound concentration could be observed.

Both effects were stronger for the biologically active trans-state. The measurements with the photoisomeric counterpart (cis) showed an effect equal to an approximate cis:trans-ratio of 80:20.

# Chapter 7

# Analysis of Bacterial Growth in Low Volumes

The ability to start antimicrobial susceptibility measurements from only few cells and low volumes has the potential to reduce the total AST time by obviating additional waiting time needed for bacterial culture [52]. Because the IDA-method only evaluates the volume above the grating, it has an intrinsic spacial filter and no need for big sample volumes. In this chapter, bacterial growth in very low volumes of down to 60 nl is analyzed with the IDA-method. For this, a custom-designed low volume sample holder was designed. The fabrication technique and layout of the low volume sample holder is presented in the first section. Subsequently, the custom low volume sample holder was used to analyze the effects of low volumes on bacterial growth and mobility. An additional aim of the sample holder was to determine the smallest, reasonable measurement volume in order to improve the throughput of samples for the IDA-method. In the following section, the detection sensitivity and delay in growth signal for different starting concentrations of bacteria in a volume of 80 nl is evaluated. In the final section, the MIC of ampicillin and E. coli is determined in sample volumes of 80 nl and the results are compared to measurements in 150 µl. The work presented in this chapter was a collaboration with Julian Aschauer within the scope of his master thesis [101].

## 7.1 Low Volume Sample Holder

In order to measure bacterial growth in very low volumes with the IDA-method, a custom low volume sample holder was designed. A design with six rows of different volumes with six chambers per volume was chosen as it a allows the analysis of various small volumes on bacterial growth and mobility. A photograph of a finished low volume sample holder in comparison to an *Ibidi µ-Slide VI 0.4* six-channel and a 96 sample plate container is shown in Figure 7.1.

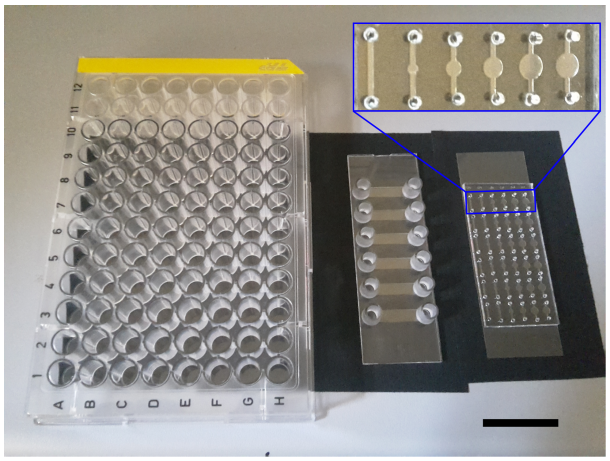

Figure 7.1: **Comparison of a 96 well plate, a 6 well microscopy slide and the custom low volume sample holder.** Typical working volumes for the 96 well plate are 100-300 µl. The 6 well microscopy slide (middle) used in a majority of this thesis need 30-150 µl sample volume per well. The custom low volume sample holder on the right is used to analyze bacterial growth and mobility with the IDA method in volumes between 60 and 656 nl. The scale bar equals 2.5 cm. Image taken from [101]

The individual sample chambers consist of a circular compartment which is connected to two valves by small channels. For the circular compartments in the middle of each chamber, five different diameters were used: 0.5, 1 , 1.5, 2 and 2.5 mm (the highest diameter was used twice to allow a reference measurement in the second channel). For the growth analysis in different volumes, sample holders with three different chamber heights of 20, 50 and 100 µm were fabricated. The resulting 15 different volumes are shown in Table 7.1.

| Chamber volumes [nl] | | ∅[mm] 2.5 | 2 | 1.5 | 1 | 0.5 |
|---|---|---|---|---|---|---|
| h[µm] | 100 | 656 | 516 | 400 | 330 | 300 |
| | 50 | 328 | 258 | 200 | 165 | 150 |
| | 20 | 133 | 103 | 80 | 66 | 60 |

Table 7.1: **Chamber volumes of the custom-designed sample holder.** The table shows the fifteen resulting chamber volumes for the five different diameters ∅ and three different heights h used for the analysis of small volumes presented in Section 7.2.

### Fabrication of the Sample Holder

For the fabrication of the sample holder, a microstructured polydimethylsiloxane (PDMS) layer was bonded to a 180 µm thick borosilicate glass microscopy slide. PDMS is often used for optical and microfluidic applications, as it is optically transparent, inert and non-

toxic. Due to its viscoelasticity, it acts like a fluid for long time scales, since the oligomer forms linear strings and is not branched by itself. The addition of siloxane cross-linkers leads to an interconnection of the single strands and resulting in an elastic solid form of the PDMS. The PDMS structure needed for the sample holder can be fabricated by casting PDMS on a silicon wafer with the negative of the desired structure [116]. The master wafer, which can be used for countless PDMS structures, was produced in the clean room at the chair of Prof. Kotthaus. During the first sample holder fabrication step, the master wafer is placed inside a standard petri dish with 90 mm diameter and fixed with a double sided adhesive tape. Next, 15 g of Sylgard184 in addition to 1.5 g curing agent are mixed and poured onto the master wafer, resulting in a layer thickness of 2-3 mm. The mixture is subsequently desiccated for 15 minutes in order to remove bubbles. For the cross-linking reaction, the petri dish is placed for six hours in an oven at 50°C. Subsequently, the PDMS layer was cut out in order to fit onto the glass coverslip and holes for sample injection were punched in at the rims of the channels (using a *Rapid-Core sampling tool* with 1.2 mm diameter). A suitable method to attach the PDMS to the glass coverslip is by oxygen plasma bonding [117]. This is achieved by plasma cleaning both the surface of the PDMS and the glass. Thus, the surfaces are oxidized, which means that O-H-groups are attached. When both surfaces are stacked, the O-H-groups react and form covalent bonds in form of Si-O-Si-groups in addition to $H_2O$ as a side product. An additional advantage of plasma oxidation is that it makes the PDMS hydrophyilic and thus improves the handling with aqueous substances [118]. For the plasma cleaning step, the PDMS structure and a cleaned borosilicate glass coverslip were placed inside a plasma cleaner. After 10 minutes of dessication, the oxygen atmosphere is adjusted to 0.2 atm and the plasma generator is activated for 24 seconds at power 2.0. Subsequently, the plasma chamber was ventilated and both components removed. In the final step, the PDMS is carefully placed onto the glass coverslip and slight pressure is applied in order to guarantee the oxygen plasma bonding.

## 7.2 Growth and Mobility Analysis in Low Volumes

Growth measurements of *B. subtilis* (NCIB 3610) were conducted using the custom low volume sample holder in order to analyze the effect of low chamber volumes on the bacterial growth and mobility as well as on the measured IDA signal. For this, an overnight culture was diluted to a turbidity equal to $OD_{600} = 0.05$ and subsequently grown at 37°C to $OD_{600} = 0.1$ in order to guarantee exponential growth behavior. The resulting day culture was diluted by a factor of 50, leading to a starting concentration of $OD_{600} = 0.002$. The bacteria suspension was injected into the sample chambers using a 2-20 µl pipette tip, as the tip diameter equals the diameter of the chamber inlets and thus allows the application of pressure in order to facilitate the injection. Remaining excess liquid was removed using a 0.1-2.5 µl pipette. Adhesive bond was attached to the top of the chamber inlets to avoid evaporation.

The resulting diffraction peak intensity-decreases and the mean normalized standard deviations for the growth measurements are shown in Figure 7.2. The smallest chamber diameter (0.5 mm) sometimes led to laser beam scattering at the structure's edges, thus preventing an analysis of the SD for chamber volumes of 60 and 150 nl, as well as of the diffraction peak intensity for 150 nl.

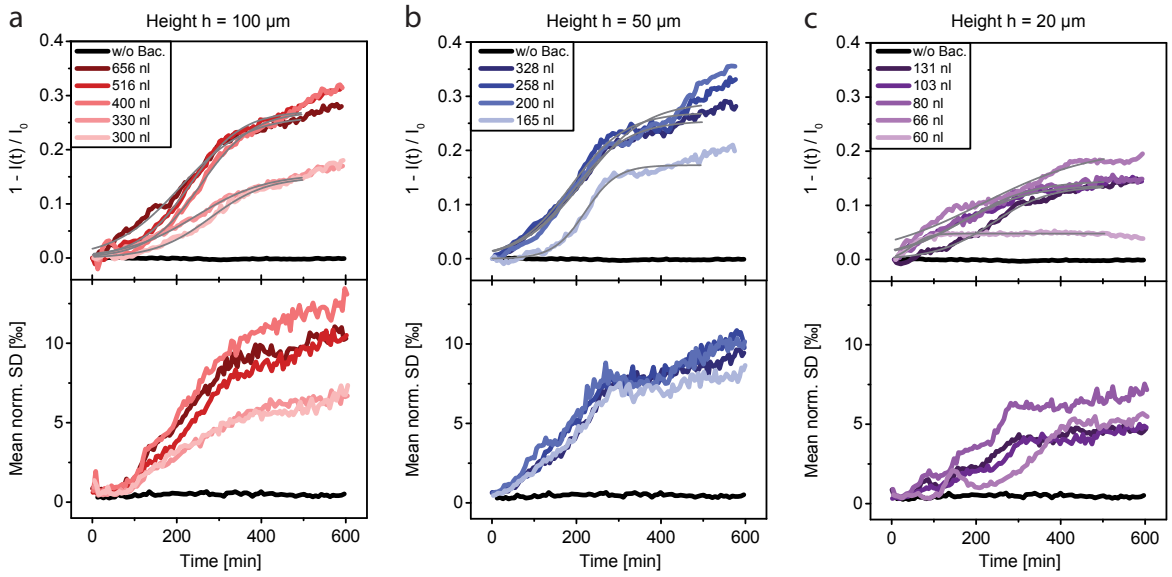


Figure 7.2: **IDA of bacterial growth in low sample volumes.** **a)** Diffraction peak intensity-decrease and mean normalized SD of *B. subtilis* growth measurements using the custom sample holder presented in Figure 7.1 and Table 7.1 with a chamber height h = 100 µm. **b)** Growth measurements analogous to panel **a** but with chamber height h = 50 µm, which lead to lower chamber volumes. The measurement in 150 nl sample volume was not evaluable, as the chamber edge obstructed the diffraction peak. **c)** Growth measurements analogous to panel **a** but with chamber heights h = 20 µm. Here, the smallest chamber diameter (d = 0.5 mm, chamber volume = 60 nl) showed short-term intensity fluctuations due to scattering of the laser beam at the chamber edges, leading to unusable SD results. Logistic growth functions were fitted to the diffraction peak intensity-decreases (gray lines).

On a first glimpse, a trend towards smaller IDA signals with decreasing chamber volume is visible both in the diffraction peak intensity-decrease and the normalized SD. A plot of the final intensity-decrease and normalized SD after 600 minutes (10h) is presented in Figure 7.3. Here, it can be seen that the final intensity-decrease and normalized SD for the three biggest chamber diameters (d = 1.5 - 2.5 mm) are similar for the heights h = 100 and 50 µm (red and blue). Furthermore, a dip in the final IDA signal can be seen for the smallest and sometimes the second smallest diameter (d = 0.5 and 1 mm, respectively). This dip could potentially arise because the edge of the smaller growth chambers

obstructs the diffraction peak, leading to a distorted IDA signal. A further possibility is that the dip originates from the stronger limitation of nutrients due to less media, leading to an earlier stationary phase of bacterial growth. The general trend towards less total growth for decreasing volumes can further be seen when taking the lowest volumes (height h = 20 µm) into account (Figure 7.3a and b). The linear function fitted to the diffraction peak intensity-decrease at t = 600 minute is $f(v) = 3.1 \cdot 10^{-4} v + 0.14$, and the respective linear fit function for the normalized SD is $f(v) = 9.5 \cdot 10^{-3} v + 5.8$.

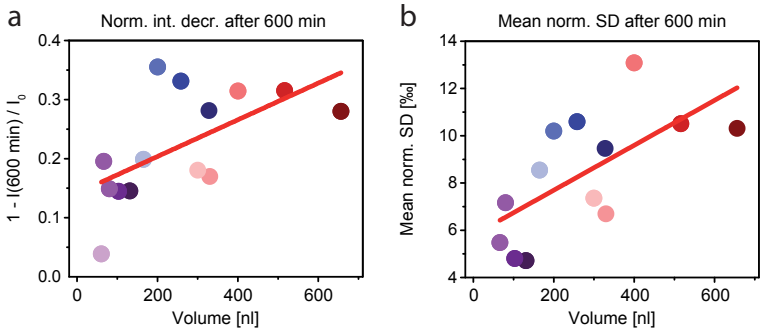


Figure 7.3: **Effect of smaller volumes on the final IDA signal. a)** Final diffraction peak intensity-decrease evaluated after 600 minutes from the IDA measurements shown in the upper row in Figure 7.2. **b)** Final mean normalized SD evaluated after 600 minutes from the IDA measurements shown in the lower row in Figure 7.2.

In order to evaluate a delay of the growth or an effect on the doubling time, a logistic function was fitted to the first 500 minute of the normalized diffraction peak intensity-decrease (Figure 7.2, gray curves). A plot of the critical growth time $t_c$, i.e. the inflection point of the fit function, is shown in Figure 7.4a. Here, no clear trend is visible except for the smallest volume of 60 nl, which does not allow a reasonable growth analysis. An evaluation of the doubling times shows consistent results with the exception of the smallest volumes v = 60 and 66 nl as well as v = 165 nl, which were all measured with the two smallest chamber diameters (7.4b). However, the average doubling time of 48 ± 18 minute is bigger than the average doubling time determined from six OD plate reader growth measurements in 1 ml sample volume of 30.5 ± 2.0 minute. A possible explanation is again the limitation of nutrients due to less media. In addition to the growth analysis, the mean mobility over the measurement duration was evaluated by applying the mobility analysis presented in Chapter 3. The results show a trend of decreasing mobility with decreasing chamber volume (Figure 7.4c), which again could arise due to limited nutrients. The shown linear fit function is $f(v) = 1.48 \cdot 10^{-4} v + 0.177$.

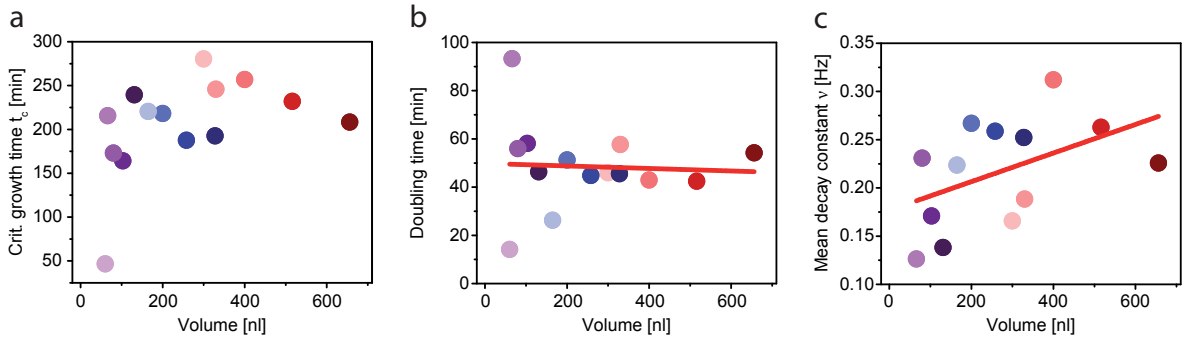


Figure 7.4: **Effect of smaller volumes on growth and mobility. a)** Critical growth time $t_c$ of the logistic fits to the diffraction peak intensity-decreases shown in Figure 7.2. With the exception of the smallest sample volume of 60 nl, no clear volume dependency is visible and the average critical growth time is 218 ± 33 minutes. **b)** Doubling times of the measurements shown in Figure 7.2. With the exception of measurements with the two smallest diameters at heights h = 20 and 50 µl, all chamber volumes allowed a consistent determination of the doubling time, with an average of 48 ± 18 minutes. This is further shown in the flat linear fit (red line) with a slope of $-0.0052 \cdot 1/\text{nl}$. **c)** Mobility analysis of the measurements shown in Figure 7.2. A trend towards a lower mobility for decreasing chamber volumes can be seen. The linear fit function is $f(v) = 1.48 \cdot 10^{-4} v + 0.177$.

## 7.3 Varying the Starting Concentration

As mentioned in the introduction to this chapter, the ability to measure antimicrobial resistance from few cells can avoid the need for bacterial culture in order to achieve a sufficient number of bacteria for the inoculum of the probing sample. For this, not only the measurement volume but also the starting bacterial concentration is decisive. To analyze the effect of different starting concentrations on the duration of growth measurements with the IDA-method, measurements with four different starting concentrations of *B. subtilis* (NCIB 3610) were conducted in MHB using the 80 nl sample chamber (h = 20 µm and d = 1.5 mm). This chamber was used because it allowed a doubling time determination in agreement with bigger sample chambers (Figure 7.4b) and the diameter did not lead to any complications, while being able to measure in less than 100 nl. The starting concentrations used in the analysis where equal to a turbidity of $OD_{600}$ = 0.1, 0.01, 0.006 and 0.001. Since an $OD_{600}$ of 0.1 corresponds to $1 \cdot 10^7$ cells/ml [119], the absolute starting numbers are approximately 1000, 100, 60 and 10 bacteria per chamber, respectively. Microscopy images of starting concentrations with $OD_{600}$ = 0.1, 0.01, and 0.001 are shown in Figure 7.5. For the lowest concentration, it was difficult to find a single bacterium with the microscope.

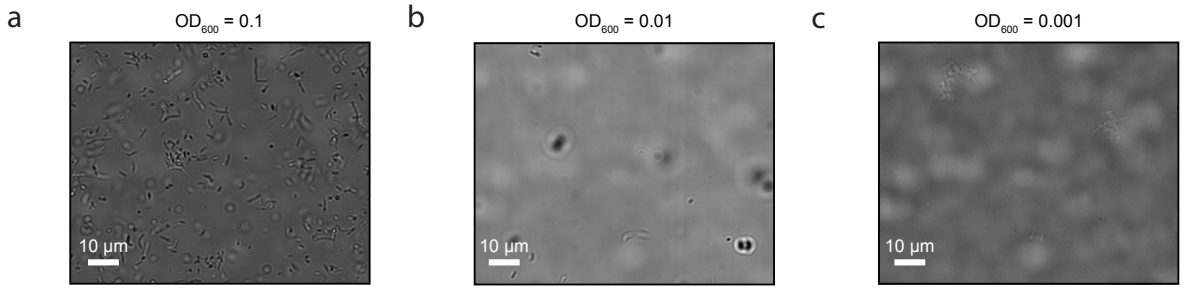


Figure 7.5: **Microscopy images of different starting concentrations.** The shown concentrations correspond to a turbidity and number of cells per 80 nl chamber of: **a)** $OD_{600}$ = 0.1 and 1000 bacteria per chamber, **b)** $OD_{600}$ = 0.01 and 100 bacteria per chamber and **c)** $OD_{600}$ = 0.001 and 10 bacteria per chamber. Images taken from [101].

The resulting time courses of the diffraction peak intensity-decrease and the mean normalized SD are presented in Figure 7.6. For the diffraction peak intensity-decrease it was difficult to achieve a reliable stability with the low volume and low concentration prototype IDA setup (Figure 7.6a). However, as it was shown in Chapter 5, the standard deviation is independent of long-term intensity instabilities and was therefore used for the growth analysis (Figure 7.6b). Being flagellated, *B. subtilis* can move easily and no attachment to the surface was observed. Thus, it can be assumed that the bacterial growth is proportional to the mean normalized SD. A logistic function was fitted to the mean normalized SD time course (Figure 7.6b, gray lines) and evaluated for the doubling time, critical growth time $t_c$. The doubling times of 31.6 minute (OD 0.1), 27.8 minute (OD 0.01), 48.2 minute (OD 0.006) and 34.7 minute (OD 0.001) showed no dependency of the starting concentration. Furthermore, the resulting average doubling time of 35.6 $\pm$ 8.9 minute is in good agreement with the doubling time of 30.5 $\pm$ 2.0 minute, which was determined from six OD plate reader measurements in 1 ml sample volume. The critical growth times $t_c$, which mark the inflection point of the fit, are presented in Figure 7.6c in red. A linear fit to the semi-logarithmic plot reveals a delay of $t_c$ by 65 minutes per order of magnitude of lower starting concentration. As a further analysis, the initial mean normalized SD was evaluated by averaging over the respective first 20 minutes (Figure 7.6c, blue) of each measurement. The linear fit shows an increase of 0.97‰ of initial SD per increasing order of magnitude in starting concentration. However, for all bacteria concentrations, the value of the initial SD was above the value of a reference measurement in the same setup with bacteria-free growth medium (Figure 7.6c, dashed line marked "w/o bacteria"). Thus, this section has shown that it is possible to detect very low bacterial cell concentrations with the IDA-method and further determine the doubling times in sample volumes of less than 100 nl.

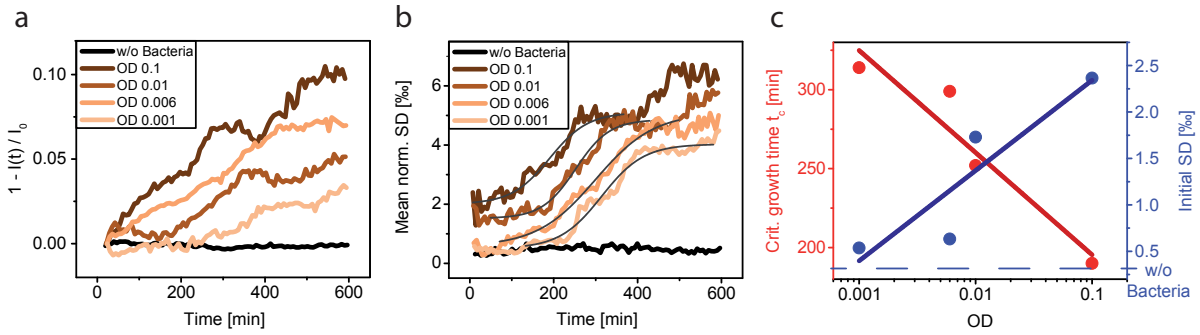


Figure 7.6: **IDA measurements of different starting concentrations in sample volumes of 80 nl.** **a)** Diffraction peak intensity-decrease for four different starting concentrations which correspond to an $OD_{600}$ of between 0.1 and 0.001. **b)** Respective mean normalized SD. For further analysis, the curves were fitted by a logistic growth function (gray lines). **c)** The analysis of the critical growth times from panel **b** (red) shows a delay of measurable growth curves by 65 minutes per decrease of starting concentration by an order of magnitude. The initial SD averaged over the respective first 20 minutes increases by 0.97‰ per order of magnitude of starting concentration. All initial mean normalized SD values were above the value of a reference measurement in the same chamber and with MHB but without bacteria (dashed line).

## 7.4 AST of Ampicillin in Ultra-Low Volume

In this section, the rapidity of antimicrobial susceptibility testing (AST) in 80 nl sample volume is analyzed and compared to AST measurements in 150 µl presented previously in Chapter 5. To this end, an ampicillin concentration series was conducted analogously to the one shown in Chapter 5 using *E. coli* bacteria and the same starting concentration of $OD_{600} = 0.004$ which is equivalent to approx. 32 bacteria in the 80 nl sample chamber. While the diffraction peak intensity-decrease of the low volume ampicillin concentration series showed a similar behavior as the mean normalized SD (Figure A.6 and 7.7a), the latter was used to determine the minimal inhibitory concentration (MIC), as it is robust towards long-term intensity instabilities. The MIC was determined as shown in Figure 5.2b, but using the mean normalized SD instead of the diffraction peak intensity-decrease. To be able to compare the results with the ampicillin concentration series in 150 µl sample volumes, the respective MIC was analogously determined using the mean normalized SD (Figure 7.7b). The resulting determined MIC values are shown for both sample volumes in Figure 7.7c. It can be seen that an MIC of approx. 4 mg/l can be detected after 120 minutes for the ultra-low sample volumes of 80 nl. Yet, the determined MIC fluctuates until 240 minutes, whereupon it remains at a constant value (Figure 7.7c, upper panel). For the higher sample volumes of 150 µl, an MIC of 2 mg/l can be detected after 120 minutes and the time curve shows less fluctuations. While literature values for the MIC for ampicillin and *E. coli* show an almost equal amount of mentions of 2 mg/l

as well as of 4 mg/l [80], it is interesting that the ultra-low volume measurements show a shift in MIC. Whether very low sample volumes have an effect on the MIC for other antibiotics will be further analyzed in future IDA projects.

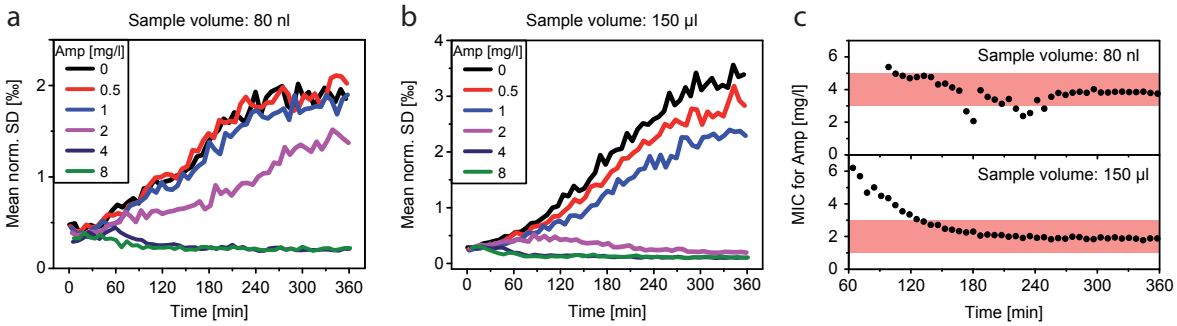


Figure 7.7: **Determining the MIC of ampicillin for *E. coli* in ultra-low and regular sample volumes. a)** Mean normalized SD of an ampicillin concentration series conducted in sample volumes of 80 nl. **b)** Mean normalized SD of an ampicillin concentration series conducted in sample volumes of 150 µl. **c)** Determined MIC value for the concentration series in sample volumes of 80 nl (upper panel) and 150 µl (lower panel).

In addition to the MIC determination, the susceptibility analysis shown previously in Chapter 5 was applied to the ultra-low volume measurements. To this end, the mean normalized SD of a sample with and without breakpoint recommendation concentration of ampicillin (8 mg/l [80]) was calculated over intervals of five seconds and averaged over the one minute acquisition intervals. For the lower sample volume of 80 nl, an antimicrobial effect could be detected after 43 minutes when the 99% confidence intervals of the mean were distinguishable (Figure 7.8a). This is only 18 minutes slower than for the higher sample volumes of 150 µl (Figure 7.8b). The difference in detection time potentially occurs from the limited nutrients and the reduced growth in lower volumes, as discussed in Section 7.2.

In summary, this chapter has shown that the IDA-method allows bacterial growth and AST measurements of low starting concentrations in less than 100 nl of sample volume. While smaller sample volumes also lead to less growth, the MIC and susceptibility of *E. coli* and ampicillin could be determined after a similar time as with conventional sample containers.

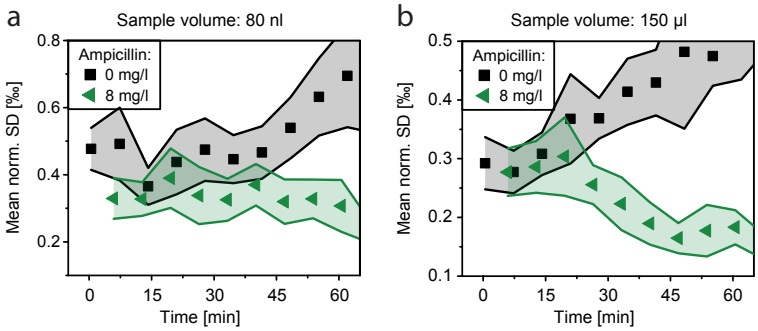


Figure 7.8: **Susceptibility testing in ultra-low and regular sample volumes. a)** The mean normalized SD of a sample without (black) and with breakpoint recommendation concentration (green) was calculated over intervals of 5 seconds and the 12 resulting values were averaged over the respective scanning acquisition times of 1 minute (bold squares and triangles). An antimicrobial effect could be detected after 43 minutes, when the 99% confidence intervals of the means (shaded error bands) could be distinguished. **b)** The same analysis in sample volumes of 150 µl allows a slightly earlier detection of the antimicrobial effect, as the 99% confidence intervals can be distinguished after 25 minutes.

# Chapter 8

# Conclusion and Outlook

In recent years, the inappropriate use of antibiotics has led to an alarming increase in antibacterial resistances (ABR) of pathogenic bacteria [4][6]. A crucial problem in the battle against ABR is the immense time consumption of current techniques of antimicrobial susceptibility testing (AST). The determination of an appropriate, narrow-spectrum antibiotic with conventional techniques can take up to several days, forcing physicians to prescribe a broad-spectrum antibiotic. This in turn leads to an increase of resistances against the latter [120][121][122]. For conventional AST techniques such as broth microdillution, a lot of time is lost on culturing bacteria, in order to achieve sufficient starting numbers for a given AST technique [52]. This step could be surpassed by a detection method with a high sensitivity and the ability to measure in very small volumes. An early identification of an appropriate antibiotic has further advantages such as lower mortality rates, shortened treatment durations, performance of less invasive procedures and substantial cost savings [71][70]. Besides ABR due to genetic mutations, bacteria can develop resistances through the formation of biofilms, thus increasing the resistance up to 1000-fold compared to their planktonic counterparts [26][27][25]. The initial steps in biofilm formation comprise the attachment of single bacterial cells to a surface, followed by the growth of microcolonies [28]. In order for a detection method to be able to measure AST of planktonic and of biofilm-forming bacterial strains, a rapid measurement of antimicrobial response in low volume with single-cell resolution as well as the ability to measure cell immobilization are highly desirable.

The aim of this thesis was the analysis and development of a diffraction-based detection method that utilizes interference disturbances induced by small objects above a 2D diffraction grating. The detection method called Interference Disturbance Analysis (IDA) records the intensity of a diffraction peak over time and is able to draw conclusions on the amount and mobility of the objects from long- and short-term intensity fluctuations.

The IDA detection method was introduced and calibrated by using 3 µm sized latex beads as a non-living model system. The beads were analyzed in an IDA setup that was

implemented inside an optical microscope in order to correlate the diffraction intensity signal to the real space (Figure 8.1a). Here, it was shown that the traversal of a single bead across the 2D grating leads to a decrease in diffraction peak intensity in combination with short-term intensity fluctuations around the mean normalized intensity (Figure 8.1b). The diffraction peak intensity-decrease is proportional to the number of beads above the grating. Furthermore, it was shown that the short-term intensity fluctuations arise due to a position dependency of the intensity-decrease (Figure 8.1c). The experimental data of the position dependent intensity-decrease was fitted by a polynomial function and used for a simulation in order to correlate the short-term intensity fluctuations with the diffusion coefficient of the beads (Figure 8.1d). With the simulation results, the diffusion coefficient of a bead moving due to Brownian motion was obtained by analyzing the respective experimental short-term intensity fluctuations. It was found that the result is in very good agreement with the theoretical diffusion coefficient of a 3 µm sized bead in the given experimental surrounding.

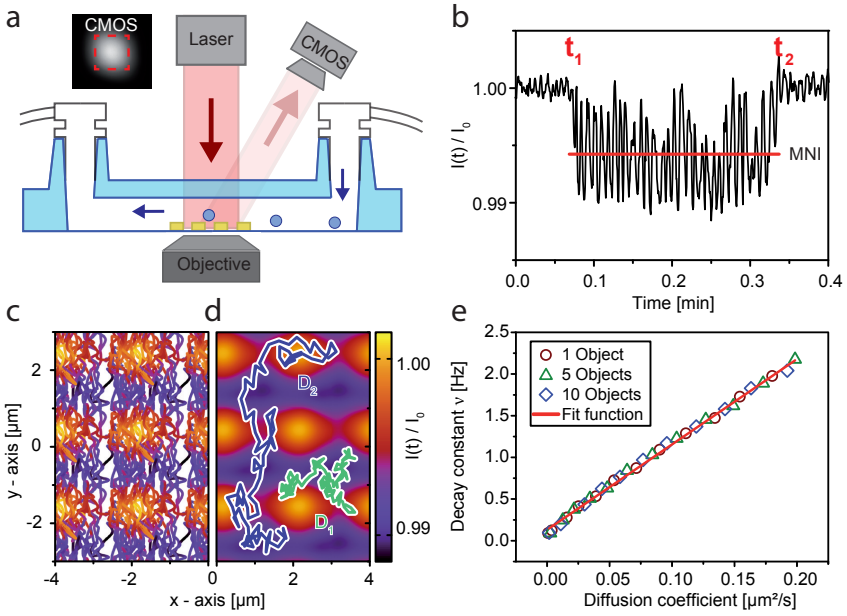


Figure 8.1: **Interference disturbance analysis of latex beads as a non-living model system. a)** Microscope-configuration of the IDA setup. **b)** The transversal of a single bead across the grating (between $t_1$ and $t_2$) leads to a decrease of the mean normalized intensity (MNI) as well as to short-term intensity fluctuations. **c)** Experimental data of the position dependent intensity-decrease of a single bead for 2 x 3 unit cells. **d)** 2D polynomial fit to the data shown in panel **c**. The highlighted lines illustrate simulated traces of beads with diffusion coefficients $D_1 = 0.05\,\mu m^2/s$ (green) and $D_2 = 0.15\,\mu m^2/s$ (blue). **e)** Correlation between the decay constant $\nu$, which is derived from Fourier analysis of the short-term intensity fluctuations, and the diffusion coefficient. Reproduced in part with permission from Nano Letters, in press. Copyright 2018 American Chemical Society.

After the calibration with a non-living model system, the growth of bacterial ensembles was analyzed with the IDA setup. When the bacteria were growing directly above the grating, a high detection sensitivity of 1.6 bacteria was measured for low cell numbers and the used grating parameters of 30 x 30 gold structures with a periodicity of 2 µm (Figure 8.2a). Further, it was shown that the decrease of the diffraction peak intensity correlates linearly with the area covered by the bacteria up to a covered area of approximately 70%. The mobility analysis introduced in the calibration section was applied to bacterial measurements. Here, a decrease of mobility by a factor of three was measured during bacterial adhesion to a glass coverslip, which was confirmed with microscopy image analysis (Figure 8.2b).

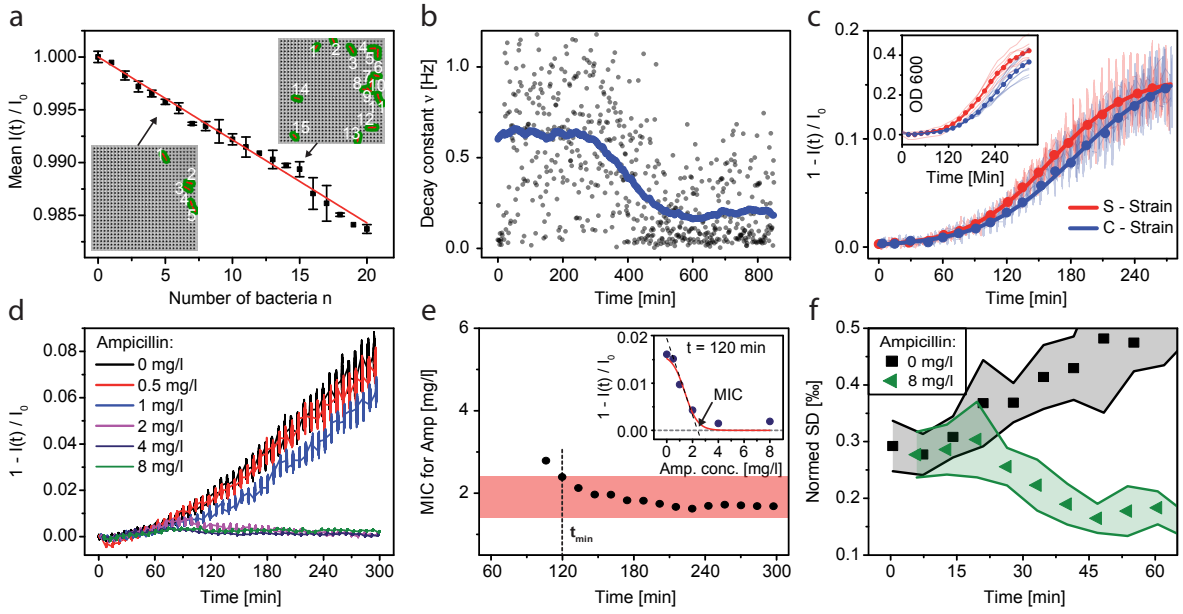


Figure 8.2: **Bacterial growth and AST measurements with the IDA setup. a)** Correlation between the normalized diffraction peak intensity and the number of bacteria n (for 1-20 bacteria). **b)** The time course of the decay constant $\nu$ for a bacterial growth measurement shows a decrease of mobility by a factor of 3.2 during attachment of the bacteria to the surface. **c)** The doubling times for two different bacterial strains were determined with the IDA setup and confirmed with optical density measurements (inset). **d)** Ampicillin concentration series for the determination of the MIC for *E. coli*. **e)** The MIC could be determined after 120 minutes. **f)** Measurements of samples without and with the breakpoint recommendation concentration of ampicillin. The analysis of the normed SD showed an antimicrobial effect after 25 minutes, when the 99% confidence intervals could be distinguished. For a resistant strain, the normed SD of both samples was indistinguishable for the total measurement duration of 10 hours. Reproduced in part with permission from Nano Letters, in press. Copyright 2018 American Chemical Society.

An alternative setup configuration was analyzed, in which the grating was placed outside of the growth chamber. This configuration enables high-throughput growth and AST measurements. While the ability to measure in high-throughput comes with a tradeoff in form of a reduced sensitivity by a factor of 3-4, the mobility analysis is still feasible with this configuration (see Chapter 6). It was shown that the high-throughput IDA configuration can be used to correctly determine bacterial doubling times (Figure 8.2c) as well as the minimum inhibitory concentration (MIC) of antibiotics (Figure 8.2d). Here, the MIC was determined for three different antibiotics and two different bacterial species in less than 2-3 hours by fitting a logistic function to the diffraction peak intensity-decrease plotted against the antibiotic concentration (Figure 8.2e). Moreover, the normalized SD was found to be an early indicator of antibiotic susceptibility while being robust against, e.g, temperature gradients arising when opening an incubator door. The antibiotic susceptibility was determined by comparing the normalized SD of samples with the breakpoint recommendation concentration to samples without antibiotic. While an antimicrobial effect could be detected in less than 30-60 minutes for susceptible strains, the normalized SD curves with and without antibiotic of a control measurement with a resistant strain were indistinguishable over the total measurement duration of 10 hours.

Subsequently, a photoswitchable antibiotic, Azo-PC, which was provided by the group of Prof. Trauner (NYU) and especially designed as an optical control of bacterial mobility was analyzed with the IDA detection method (Figure 8.3a). For this, a setup configuration with a beam splitter was presented, which allows the simultaneous measurement of four diffraction gratings. This setup was used to measure a concentration series of the photoswitchable antibiotic in the cis- and the trans-state simultaneously, using the same overnight culture of bacteria for all samples. Growth measurements with the photoswitchable antibiotic have shown a higher antimicrobial effect for the biologically active trans-state versus the inactive cis-state in form of delayed growth times (Figure 8.3b). The mobility analysis has further revealed a decrease in mobility with increasing compound concentration with again a stronger effect for the biologically active trans-state (Figure 8.3c). Thus, the desired effect of the photoswitchable antibiotic could be confirmed with the IDA detection method.

Finally, a self-designed sample container for low volume measurements was introduced and used to analyze the effect of confined volumes and media amounts on bacterial growth, mobility and the MIC. The results showed that bacterial growth could still be reliably detected in volumes of less than 100 nl. Yet, tendencies of a decrease in growth and mobility as well as a shift of the MIC towards higher concentrations were detected for smaller volumes. These findings will be analyzed in more detail in future projects with the IDA setup. With the help of the self-designed sample container and the beam splitter, the amount of samples that can be analyzed simultaneously was increased to 256. Here, the measurement volume of each sample is approximately 1000 times smaller than the volume of the sample containers used in the majority of the thesis and about 100 times smaller than the volume used in automated AST devices [21].

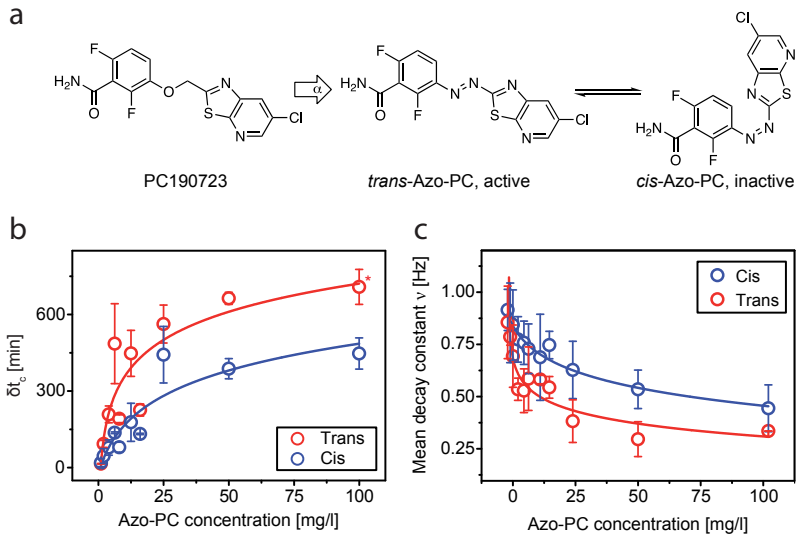


Figure 8.3: **IDA of a photoswitchable antibiotic, designed as an optical control of mobility. a)** Chemical structure of the model cytokinesis inhibitor PC190723 as well as of the biologically active trans-state and the inactive cis-state of the photoswitchable Azo-PC compound. **b)** The delay of bacterial growth was determined by calculating the difference of the critical growth times $t_c$ (derived from a logistic fit to the intensity-decrease) compared to a reference sample without the compound. The resulting $\delta t_c$ shows a stronger effect for the active trans- than for the inactive cis-state. **c)** Additionally, the mobility analysis depicts a stronger decrease of mobility with increasing Azo-PC concentration for the active trans-state as compared to the inactive cis-state of the compound.

In conclusion, it was demonstrated in this thesis that the IDA method allows the detection of small particles such as beads or bacteria as well as conclusions on the amount and mobility of the particles. It is especially suitable for bacterial measurements of low cell concentrations in small volumes and for rapid antimicrobial susceptibility testing. Furthermore, the method can be easily scaled for high throughput and allows the analysis of the effect of antibiotics on growth and mobility simultaneously both for planktonic as well as biofilm-forming bacteria. An additional advantage of the detection method is that only few components and no image analysis are needed.

In the future, combining the IDA setup with isolation techniques could enable measurements of clinical samples such as blood or urinary tract infections [67]. The use of the IDA setup in combination with antibodies attached to the gold grating could permit specific bacterial detection from polymicrobial or biological samples and allow subsequent flushing and susceptibility testing. Such applications of antibodies attached to gold structures are already in use for whole-cell bacterial detection [123]. Concerning

future improvements of the detection method, the stability of the normalized SD and the diffraction peak intensity could potentially be improved by, e.g., vibration-damping of the laser and the grating, possibly resulting in quicker AST results. Furthermore, the use of ultra thin foil for the sample chambers could improve the sensitivity of the high-throughput configuration. The sample container could be designed for even lower volumes and higher throughputs. With the current design, all samples have to be filled manually. Here, the use of microfluidics in order to fill all channels with a single valve is conceivable. Future measurements with the IDA setup could comprise the analysis of antimicrobial efficacy during different stages of biofilm formation. Furthermore, the detection method could be used in order to analyze bacterial adhesion properties towards different materials as well as surface passivations designed to avoid biofilm development.

# Bibliography


[1] Alexander Fleming. On the antibacterial action of cultures of a penicillium, with special reference to their use in the isolation of b. influenzae. *British journal of experimental pathology*, 10(3):226, 1929.

[2] Phillip I Lerner. Producing penicillin. *New England Journal of Medicine*, 351(6):524–524, 2004.

[3] Henrik C Wegener. The consequences for food safety of the use of fluoroquinolones in food animals, 1999.

[4] Alfonso J Alanis. Resistance to antibiotics: are we in the post-antibiotic era? *Archives of medical research*, 36(6):697–705, 2005.

[5] Stuart B Levy. *The antibiotic paradox: how the misuse of antibiotics destroys their curative power*. Da Capo Press, 2002.

[6] C Lee Ventola. The antibiotic resistance crisis: part 1: causes and threats. *Pharmacy and Therapeutics*, 40(4):277, 2015.

[7] Jim ONeill. Tackling drug-resistant infections globally: final report and recommendations. review of antimicrobial resistance. london: Hm government and wellcome trust; 2016. *There is no corresponding record for this reference*, 2016.

[8] John M. Martinko Michael T. Madigan. *Brock Mikrobiologie*. Pearson Studium, 11., aktualisierte auflage 2009 edition, 12 / 2008.

[9] Julian Davies and Dorothy Davies. Origins and evolution of antibiotic resistance. *Microbiology and molecular biology reviews*, 74(3):417–433, 2010.

[10] Christopher M Thomas and Kaare M Nielsen. Mechanisms of, and barriers to, horizontal gene transfer between bacteria. *Nature reviews microbiology*, 3(9):711, 2005.

[11] Otto G Vanderkooi, Donald E Low, Karen Green, Jeff E Powis, Allison McGeer, and Toronto Invasive Bacterial Disease Network. Predicting antimicrobial resistance in invasive pneumococcal infections. *Clinical Infectious Diseases*, 40(9):1288–1297, 2005.

[12] Annalisa Pantosti and Maria Luisa Moro. Antibiotic use: the crystal ball for predicting antibiotic resistance, 2005.

[13] Didier Guillemot. Antibiotic use in humans and bacterial resistance. *Current Opinion in Microbiology*, 2(5):494–498, 1999.

[14] Sara Monroe and Ronald Polk. Antimicrobial use and bacterial resistance. *Current opinion in microbiology*, 3(5):496–501, 2000.

[15] Jan E Patterson. Antibiotic utilization: is there an effect on antimicrobial resistance? *Chest*, 119(2):426S–430S, 2001.

[16] Karen Bush, Patrice Courvalin, Gautam Dantas, Julian Davies, Barry Eisenstein, Pentti Huovinen, George A Jacoby, Roy Kishony, Barry N Kreiswirth, Elizabeth Kutter, et al. Tackling antibiotic resistance. *Nature Reviews Microbiology*, 9(12):894, 2011.

[17] John G Bartlett, David N Gilbert, and Brad Spellberg. Seven ways to preserve the miracle of antibiotics. *Clinical Infectious Diseases*, 56(10):1445–1450, 2013.

[18] Terence J Centner. Regulating the use of non-therapeutic antibiotics in food animals. *Geo. Int'l Envtl. L. Rev.*, 21:1, 2008.

[19] US Department of Health, Human Services, et al. Antibiotic resistance threats in the united states, 2013. *Centers for Disease Control and Prevention*, 2013.

[20] Charles-Edouard Luyt, Nicolas Bréchot, Jean-Louis Trouillet, and Jean Chastre. Antibiotic stewardship in the intensive care unit. *Critical care*, 18(5):480, 2014.

[21] Karan Syal, Manni Mo, Hui Yu, Rafael Iriya, Wenwen Jing, Sui Guodong, Shaopeng Wang, Thomas E Grys, Shelley E Haydel, and Nongjian Tao. Current and emerging techniques for antibiotic susceptibility tests. *Theranostics*, 7(7):1795, 2017.

[22] AW Bauer, WMM Kirby, John C Sherris, and Marvin Turck. Antibiotic susceptibility testing by a standardized single disk method. *American journal of clinical pathology*, 45(4_ts):493–496, 1966.

[23] L Barth Reller, Melvin Weinstein, James H Jorgensen, and Mary Jane Ferraro. Antimicrobial susceptibility testing: a review of general principles and contemporary practices. *Clinical infectious diseases*, 49(11):1749–1755, 2009.

[24] Irith Wiegand, Kai Hilpert, and Robert EW Hancock. Agar and broth dilution methods to determine the minimal inhibitory concentration (mic) of antimicrobial substances. *Nature protocols*, 3(2):163, 2008.

[25] Philip S Stewart and J William Costerton. Antibiotic resistance of bacteria in biofilms. *The lancet*, 358(9276):135–138, 2001.

[26] David Davies. Understanding biofilm resistance to antibacterial agents. *Nature reviews Drug discovery*, 2(2):114, 2003.

[27] Kim Lewis. Riddle of biofilm resistance. *Antimicrobial agents and chemotherapy*, 45(4):999–1007, 2001.

[28] Karin Sauer, Alex H Rickard, and David G Davies. Biofilms and biocomplexity. *Microbe-American Society for Microbiology*, 2(7):347, 2007.

[29] Coherent. *Ultra-Low Noise Diode Laser Modules*. `https://www.coherent.com/`, 2018.

[30] A Pistorius and B Willershausen. Biocompatibility of dental materials in two human cell lines. *European journal of medical research*, 7(2):81–88, 2002.

[31] Thorlabs. Protected gold mirrors. `http://www.thorlabs.de/NewGroupPage9.cfm?ObjectGroup_ID=744`, November 2018. Website.

[32] J. Stephan. Optical lensing and diffraction on periodic nanostructures for sensing cell contours and motility. Master's thesis, Ludwig-Maximilians-University Munich, 2013.

[33] Eugene HECHT. *Optik*. Oldenbourg Verlag, 2001.

[34] P. Paulitschke. *Mechanische Charakterisierung einzelner und periodisch angeordneter nanoskaliger GaAs-Saeulen*. PhD thesis, LMU, 2011.

[35] Wolfgang Zinth and Ursula Zinth. *Optik: Lichtstrahlen-Wellen-Photonen*. Walter de Gruyter, 2013.

[36] David Volbers. Real-Time Interferometric Cell Ensemble Analysis. Master's thesis, LMU, 2014.

[37] Chair for Biomolecular Optics, LMU. *Coherent Image Analysis, Practical Course*, 1993.

[38] John A Myers, Brandon S Curtis, and Wayne R Curtis. Improving accuracy of cell and chromophore concentration measurements using optical density. *BMC biophysics*, 6(1):4, 2013.

[39] Konstantin Ditzel. Interferometrische Echtzeit-Detektion sphärischer Mikropartikel, 2015.

[40] Rudolf Müller. *Rauschen*, volume 15. Springer-Verlag, 2013.

[41] N Jeremy Kasdin. Discrete simulation of colored noise and stochastic processes and 1/f/sup/spl alpha//power law noise generation. *Proceedings of the IEEE*, 83(5):802–827, 1995.

[42] Mingming Wu, John W Roberts, Sue Kim, Donald L Koch, and Matthew P DeLisa. Collective bacterial dynamics revealed using a three-dimensional population-scale defocused particle tracking technique. *Applied and environmental microbiology*, 72(7):4987–4994, 2006.

[43] Mark J McBride. Bacterial gliding motility: multiple mechanisms for cell movement over surfaces. *Annual Reviews in Microbiology*, 55(1):49–75, 2001.

[44] RN Doetsch and GJ Hageage. Motility in procaryotic organisms: problems, points of view, and perspectives. *Biological Reviews*, 43(3):317–362, 1968.

[45] Daniel B Kearns. A field guide to bacterial swarming motility. *Nature Reviews Microbiology*, 8(9):634, 2010.

[46] John T Edward. Molecular volumes and the stokes-einstein equation. *Journal of Chemical Education*, 47(4):261, 1970.

[47] Albert Einstein. *Investigations on the Theory of the Brownian Movement*. Courier Corporation, 1956.

[48] George Gabriel Stokes. *On the effect of the internal friction of fluids on the motion of pendulums*, volume 9. Pitt Press Cambridge, 1851.

[49] Eric R Dufresne, Todd M Squires, Michael P Brenner, and David G Grier. Hydrodynamic coupling of two brownian spheres to a planar surface. *Physical Review Letters*, 85(15):3317, 2000.

[50] Luc P Faucheux and Albert J Libchaber. Confined brownian motion. *Physical Review E*, 49(6):5158, 1994.

[51] William Bailey Russel, WB Russel, Dudley A Saville, and William Raymond Schowalter. *Colloidal dispersions*. Cambridge university press, 1991.

[52] Alex van Belkum and Wm Michael Dunne. Next generation antimicrobial susceptibility testing. *Journal of clinical microbiology*, pages JCM–00313, 2013.

[53] Heidi Leonard, Sarel Halachmi, Nadav Ben-Dov, Ofer Nativ, and Ester Segal. Unraveling antimicrobial susceptibility of bacterial networks on micropillar architectures using intrinsic phase-shift spectroscopy. *ACS nano*, 11(6):6167–6177, 2017.

[54] Özden Baltekin, Alexis Boucharin, Eva Tano, Dan I Andersson, and Johan Elf. Antibiotic susceptibility testing in less than 30 min using direct single-cell imaging. *Proceedings of the National Academy of Sciences*, 114(34):9170–9175, 2017.

[55] Benjamin Kerr, Margaret A Riley, Marcus W Feldman, and Brendan JM Bohannan. Local dispersal promotes biodiversity in a real-life game of rock–paper–scissors. *Nature*, 418(6894):171, 2002.

[56] Gil Topman, Orna Sharabani-Yosef, and Amit Gefen. A method for quick, low-cost automated confluency measurements. *Microscopy and Microanalysis*, 17(6):915–922, 2011.

[57] Gerard J Tortora, Berdell R Funke, Christine L Case, and Ted R Johnson. *Microbiology: an introduction*, volume 9. Benjamin Cummings San Francisco, CA, 2004.

[58] Roberto Kolter, Deborah A Siegele, and Antonio Tormo. The stationary phase of the bacterial life cycle. *Annual Reviews in Microbiology*, 47(1):855–874, 1993.

[59] Elke Hebisch, Johannes Knebel, Janek Landsberg, Erwin Frey, and Madeleine Leisner. High variation of fluorescence protein maturation times in closely related escherichia coli strains. *PloS one*, 8(10):e75991, 2013.

[60] EO Powell. Growth rate and generation time of bacteria, with special reference to continuous culture. *Microbiology*, 15(3):492–511, 1956.

[61] Jacques Monod. The growth of bacterial cultures. *Annual Reviews in Microbiology*, 3(1):371–394, 1949.

[62] Sarah B Guttenplan and Daniel B Kearns. Regulation of flagellar motility during biofilm formation. *FEMS microbiology reviews*, 37(6):849–871, 2013.

[63] Gerard CL Wong and George A OToole. All together now: Integrating biofilm research across disciplines. *Mrs Bulletin*, 36(5):339–342, 2011.

[64] Courtney Reichhardt, Amy N Jacobson, Marie C Maher, Jeremy Uang, Oscar A McCrate, Michael Eckart, and Lynette Cegelski. Congo red interactions with curli-producing e. coli and native curli amyloid fibers. *PLoS One*, 10(10):e0140388, 2015.

[65] Mariana Grillo-Puertas, Josefina M Villegas, María R Rintoul, and Viviana A Rapisarda. Polyphosphate degradation in stationary phase triggers biofilm formation via luxs quorum sensing system in escherichia coli. *PloS one*, 7(11):e50368, 2012.

[66] Keegan Colville, Nicolas Tompkins, Andrew D Rutenberg, and Manfred H Jericho. Effects of poly (l-lysine) substrates on attached escherichia coli bacteria. *Langmuir*, 26(4):2639–2644, 2009.

[67] William G Pitt, Mahsa Alizadeh, Ghaleb A Husseini, Daniel S McClellan, Clara M Buchanan, Colin G Bledsoe, Richard A Robison, Rae Blanco, Beverly L Roeder, Madison Melville, et al. Rapid separation of bacteria from bloodreview and outlook. *Biotechnology progress*, 32(4):823–839, 2016.

[68] L Ferreira, F Sánchez-Juanes, JL Munoz-Bellido, and JM González-Buitrago. Rapid method for direct identification of bacteria in urine and blood culture samples by matrix-assisted laser desorption ionization time-of-flight mass spectrometry: intact cell vs. extraction method. *Clinical Microbiology and Infection*, 17(7):1007–1012, 2011.

[69] Martin Christner, Holger Rohde, Manuel Wolters, Ingo Sobottka, Karl Wegscheider, and Martin Aepfelbacher. Rapid identification of bacteria from positive blood culture bottles by use of matrix-assisted laser desorption-ionization time of flight mass spectrometry fingerprinting. *Journal of clinical microbiology*, 48(5):1584–1591, 2010.

[70] Joan Barenfanger, Cheryl Drake, and Gail Kacich. Clinical and financial benefits of rapid bacterial identification and antimicrobial susceptibility testing. *Journal of clinical microbiology*, 37(5):1415–1418, 1999.

[71] Gary V Doern, Raymond Vautour, Michael Gaudet, and Bruce Levy. Clinical impact of rapid in vitro susceptibility testing and bacterial identification. *Journal of clinical microbiology*, 32(7):1757–1762, 1994.

[72] Marlene Fredborg, FS Rosenvinge, Erik Spillum, S Kroghsbo, Mikala Wang, and TE Sondergaard. Rapid antimicrobial susceptibility testing of clinical isolates by digital time-lapse microscopy. *European Journal of Clinical Microbiology & Infectious Diseases*, 34(12):2385–2394, 2015.

[73] Chih-Yao Chung, Jhih-Cheng Wang, and Han-Sheng Chuang. Rapid bead-based antimicrobial susceptibility testing by optical diffusometry. *PloS one*, 11(2):e0148864, 2016.

[74] P Acred, DM Brown, DH Turner, and MJ Wilson. Pharmacology and chemotherapy of ampicillina new broad-spectrum penicillin. *British journal of pharmacology and chemotherapy*, 18(2):356–369, 1962.

[75] Enrique Raviña. *The evolution of drug discovery: from traditional medicines to modern drugs*. John Wiley & Sons, 2011.

[76] János Fischer, C Robin Ganellin, A Ganesan, and J Proudfoot. *Analogue-based drug discovery*. Wiley-VCH, 2010.

[77] Jean-Marie Ghuysen. Serine beta-lactamases and penicillin-binding proteins. *Annual Reviews in Microbiology*, 45(1):37–67, 1991.

[78] WA Petri. Penicillins, cephalosporins, and other $\beta$-lactam antibiotics. *Goodman and Gilman: The pharmacological basis of therapeutics, Brunton LL, Chabner BA, and Knollmann BB (ed. s), 12th edition, McGraw Hill Medical*, pages 1477–1505, 2011.

[79] Anne H Delcour. Outer membrane permeability and antibiotic resistance. *Biochimica et Biophysica Acta (BBA)-Proteins and Proteomics*, 1794(5):808–816, 2009.

[80] European Society of Clinical Microbiology and Infectious Diseases. Antimicrobial wild type distributions of microorganisms. `https://mic.eucast.org`, May 2007. Website.

[81] Jennifer M Andrews. Determination of minimum inhibitory concentrations. *Journal of antimicrobial Chemotherapy*, 48(suppl_1):5–16, 2001.

[82] Walter Sneader. *Drug discovery: a history*. John Wiley & Sons, 2005.

[83] Masarou Misumi and Nobuo Tanaka. Mechanism of inhibition of translocation by kanamycin and viomycin: a comparative study with fusidic acid. *Biochemical and biophysical research communications*, 92(2):647–654, 1980.

[84] Tomoari Kuriyama, Tadahiro Karasawa, and David W Williams. Antimicrobial chemotherapy: Significance to healthcare. In *Biofilms in Infection Prevention and Control*, pages 209–244. Elsevier, 2014.

[85] Estée Török, Ed Moran, and Fiona Cooke. *Oxford handbook of infectious diseases and microbiology*. Oxford University Press, 2016.

[86] Donald P Levine. Vancomycin: a history. *Clinical Infectious Diseases*, 42(Supplement_1):S5–S12, 2006.

[87] Steven S Branda, José Eduardo González-Pastor, Sigal Ben-Yehuda, Richard Losick, and Roberto Kolter. Fruiting body formation by bacillus subtilis. *Proceedings of the National Academy of Sciences*, 98(20):11621–11626, 2001.

[88] Chong Fang, Emanuel Stiegeler, Gregory M Cook, Thorsten Mascher, and Susanne Gebhard. Bacillus subtilis as a platform for molecular characterisation of regulatory mechanisms of enterococcus faecalis resistance against cell wall antibiotics. *PloS one*, 9(3):e93169, 2014.

[89] Daniel R Zeigler, Zoltán Prágai, Sabrina Rodriguez, Bastien Chevreux, Andrea Muffler, Thomas Albert, Renyuan Bai, Markus Wyss, and John B Perkins. The origins of 168, w23, and other bacillus subtilis legacy strains. *Journal of bacteriology*, 190(21):6983–6995, 2008.

[90] G Longo, L Alonso-Sarduy, L Marques Rio, A Bizzini, A Trampuz, J Notz, G Dietler, and S Kasas. Rapid detection of bacterial resistance to antibiotics using afm cantilevers as nanomechanical sensors. *Nature nanotechnology*, 8(7):522, 2013.

[91] Markus F Weber, Gabriele Poxleitner, Elke Hebisch, Erwin Frey, and Madeleine Opitz. Chemical warfare and survival strategies in bacterial range expansions. *Journal of The Royal Society Interface*, 11(96):20140172, 2014.

[92] Cristina García-Iriepa, Marco Marazzi, Luis Manuel Frutos, and Diego Sampedro. E/z photochemical switches: syntheses, properties and applications. *RSC Advances*, 3(18):6241–6266, 2013.

[93] Willem A Velema, Wiktor Szymanski, and Ben L Feringa. Photopharmacology: beyond proof of principle. *Journal of the American Chemical Society*, 136(6):2178–2191, 2014.

[94] José L Martínez. Antibiotics and antibiotic resistance genes in natural environments. *Science*, 321(5887):365–367, 2008.

[95] Alfredo Tello, Brian Austin, and Trevor C Telfer. Selective pressure of antibiotic pollution on bacteria of importance to public health. *Environmental Health Perspectives*, 120(8):1100, 2012.

[96] Herman Goossens, Matus Ferech, Robert Vander Stichele, Monique Elseviers, ESAC Project Group, et al. Outpatient antibiotic use in europe and association with resistance: a cross-national database study. *The Lancet*, 365(9459):579–587, 2005.

[97] Nicole Kemper. Veterinary antibiotics in the aquatic and terrestrial environment. *Ecological indicators*, 8(1):1–13, 2008.

[98] Willem A Velema, Jan Pieter Van Der Berg, Mickel J Hansen, Wiktor Szymanski, Arnold JM Driessen, and Ben L Feringa. Optical control of antibacterial activity. *Nature chemistry*, 5(11):924, 2013.

[99] Elena Contreras-García, David Martínez-López, Carla Andrea Alonso, Carmen Lozano, Carmen Torres, Miguel A Rodríguez, Pedro J Campos, and Diego Sampedro. Optical control of antimicrobial activity in quinolone derivatives. *European Journal of Organic Chemistry*, 2017(32):4719–4725, 2017.

[100] Willem A Velema, Jan Pieter van der Berg, Wiktor Szymanski, Arnold JM Driessen, and Ben L Feringa. Orthogonal control of antibacterial activity with light. *ACS chemical biology*, 9(9):1969–1974, 2014.

[101] Julian Aschauer. High Throughput Interferometric Assay for Antimicrobial Susceptibility Testing in Ultra-Low Volume. Master's thesis, LMU, 2018.

[102] David J Haydon, Neil R Stokes, Rebecca Ure, Greta Galbraith, James M Bennett, David R Brown, Patrick J Baker, Vladimir V Barynin, David W Rice, Sveta E Sedelnikova, et al. An inhibitor of ftsz with potent and selective anti-staphylococcal activity. *Science*, 321(5896):1673–1675, 2008.

[103] Nohemy A Sorto, Marilyn M Olmstead, and Jared T Shaw. Practical synthesis of pc190723, an inhibitor of the bacterial cell division protein ftsz. *The Journal of organic chemistry*, 75(22):7946–7949, 2010.

[104] José M Andreu, Claudia Schaffner-Barbero, Sonia Huecas, Dulce Alonso, María L Lopez-Rodriguez, Laura B Ruiz-Avila, Rafael Núñez-Ramírez, Oscar Llorca, and Antonio J Martín-Galiano. The antibacterial cell division inhibitor pc190723 is an ftsz polymer-stabilizing agent that induces filament assembly and condensation. *Journal of Biological Chemistry*, 285(19):14239–14246, 2010.

[105] Jeffery Errington, Richard A Daniel, and Dirk-Jan Scheffers. Cytokinesis in bacteria. *Microbiology and Molecular Biology Reviews*, 67(1):52–65, 2003.

[106] Nathaniel L Elsen, Jun Lu, Gopal Parthasarathy, John C Reid, Sujata Sharma, Stephen M Soisson, and Kevin J Lumb. Mechanism of action of the cell-division inhibitor pc190723: modulation of ftsz assembly cooperativity. *Journal of the American Chemical Society*, 134(30):12342–12345, 2012.

[107] Alan D McNaught and Alan D McNaught. *Compendium of chemical terminology*, volume 1669. Blackwell Science Oxford, 1997.

[108] Andrew A Beharry and G Andrew Woolley. Azobenzene photoswitches for biomolecules. *Chemical Society Reviews*, 40(8):4422–4437, 2011.

[109] Pau Gorostiza and Ehud Y Isacoff. Optical switches for remote and noninvasive control of cell signaling. *Science*, 322(5900):395–399, 2008.

[110] HM Dhammika Bandara and Shawn C Burdette. Photoisomerization in different classes of azobenzene. *Chemical Society Reviews*, 41(5):1809–1825, 2012.

[111] Donald E Mager. Quantitative structure–pharmacokinetic/pharmacodynamic relationships. *Advanced drug delivery reviews*, 58(12-13):1326–1356, 2006.

[112] Nicholas HG Holford and Lewis B Sheiner. Understanding the dose-effect relationship. *Clinical pharmacokinetics*, 6(6):429–453, 1981.

[113] Howard C Ansel, William P Norred, and Ivan L Roth. Antimicrobial activity of dimethyl sulfoxide against escherichia coli, pseudomonas aeruginosa, and bacillus megaterium. *Journal of pharmaceutical sciences*, 58(7):836–839, 1969.

[114] T Wadhwani, K Desai, D Patel, D Lawani, P Bahaley, P Joshi, and V Kothari. Effect of various solvents on bacterial growth in context of determining mic of various antimicrobials. *Internet J. Microbiol*, 7(1):1–8, 2009.

[115] R Phillips. Diffusion of solid particles confined in a vicous fluid, 2006. Protocol.

[116] Dong Qin, Younan Xia, and George M Whitesides. Soft lithography for micro-and nanoscale patterning. *Nature protocols*, 5(3):491, 2010.

[117] Mark A Eddings, Michael A Johnson, and Bruce K Gale. Determining the optimal pdms–pdms bonding technique for microfluidic devices. *Journal of Micromechanics and Microengineering*, 18(6):067001, 2008.

[118] Shantanu Bhattacharya, Arindom Datta, Jordan M Berg, and Shubhra Gangopadhyay. Studies on surface wettability of poly (dimethyl) siloxane (pdms) and glass under oxygen-plasma treatment and correlation with bond strength. *Journal of microelectromechanical systems*, 14(3):590–597, 2005.

[119] M Claire Arrieta, Brenda K Leskiw, and W Reuben Kaufman. Antimicrobial activity in the egg wax of the african cattle tick amblyomma hebraeum (acari: Ixodidae). *Experimental & applied acarology*, 39(3-4):297, 2006.

[120] Alex van Belkum, Géraldine Durand, Michel Peyret, Sonia Chatellier, Gilles Zambardi, Jacques Schrenzel, Dee Shortridge, Anette Engelhardt, and William Michael Dunne. Rapid clinical bacteriology and its future impact. *Annals of laboratory medicine*, 33(1):14–27, 2013.

[121] Gary V Doern, David R Scott, and Abdel L Rashad. Clinical impact of rapid antimicrobial susceptibility testing of blood culture isolates. *Antimicrobial agents and chemotherapy*, 21(6):1023–1024, 1982.

[122] JJ Kerremans, Paul Verboom, Theo Stijnen, L Hakkaart-van Roijen, Wil Goessens, HA Verbrugh, and MC Vos. Rapid identification and antimicrobial susceptibility testing reduce antibiotic use and accelerate pathogen-directed antibiotic use. *Journal of antimicrobial chemotherapy*, 61(2):428–435, 2007.

[123] Asif Ahmed, Jo V Rushworth, Natalie A Hirst, and Paul A Millner. Biosensors for whole-cell bacterial detection. *Clinical microbiology reviews*, 27(3):631–646, 2014.

# List of Figures

# Appendix

## A.1 Figures

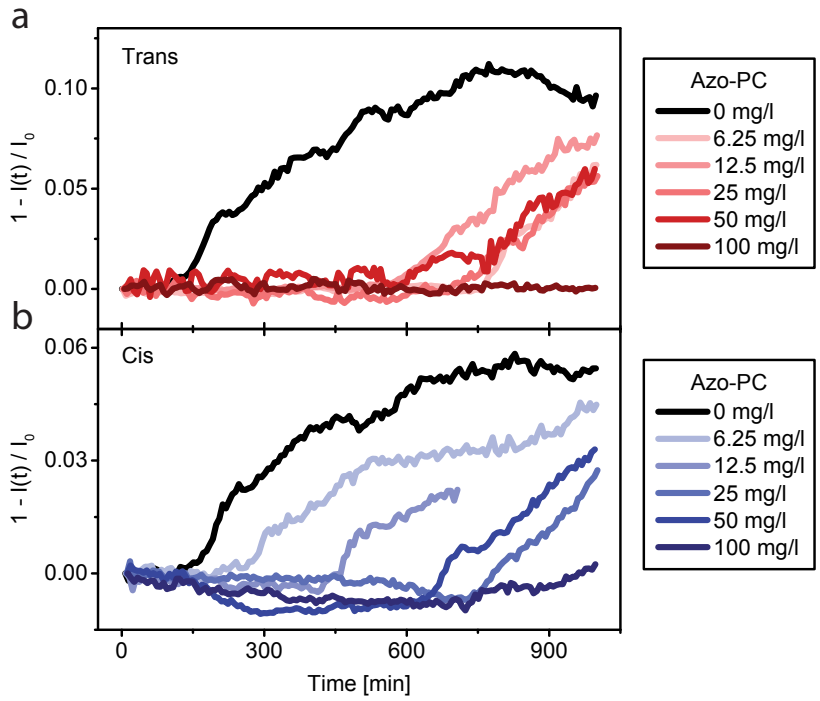


Figure A.1: **Influence of Azo-PC in the trans- and cis-state on the growth behavior of *Bacillus subtilis*.** Diffraction peak intensity for growth measurements in MHB with Azo-PC concentrations between 0 and 100 mg/l in the Trans-(**a**)) and the Cis-state (**b**)).

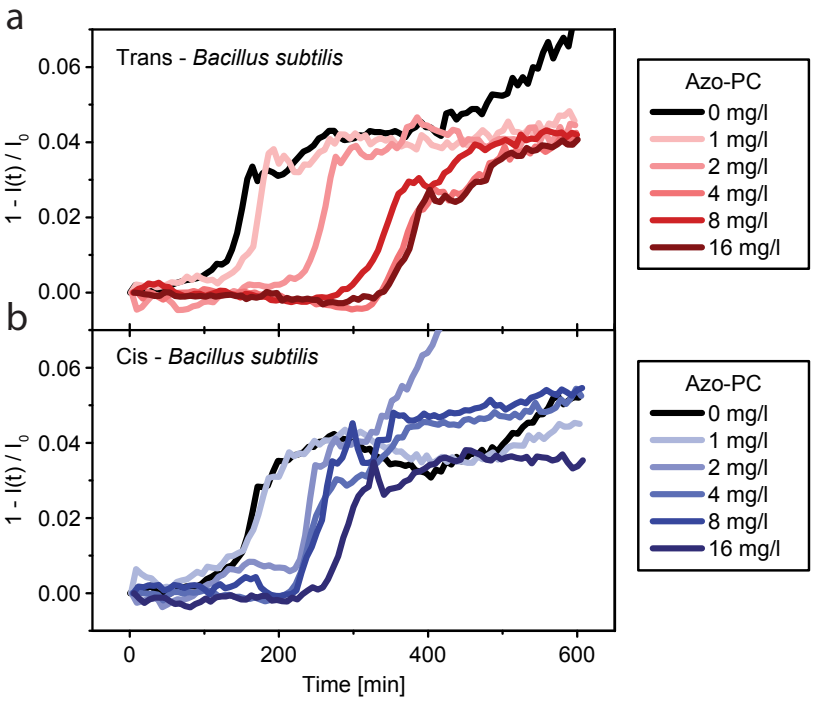


Figure A.2: **Influence of Azo-PC in the trans- and cis-state on the growth behavior of *Bacillus subtilis*.** Diffraction peak intensity for growth measurements in MHB with Azo-PC concentrations between 0 and 16 mg/l in the Trans-(**a**)) and the Cis-state (**b**)).

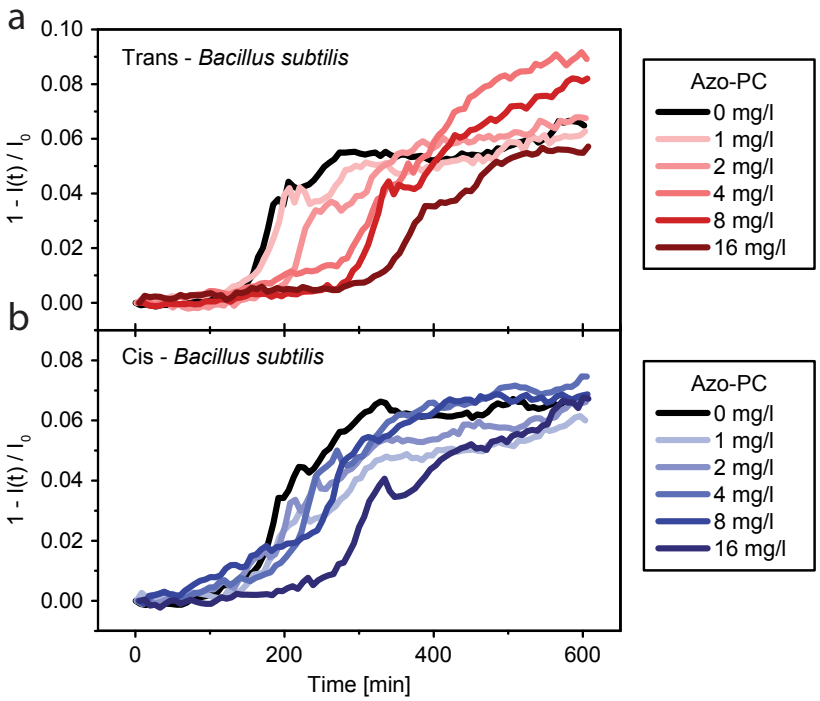


Figure A.3: **Influence of Azo-PC in the trans- and cis-state on the growth behavior of *Bacillus subtilis*.** Diffraction peak intensity for growth measurements in MHB with Azo-PC concentrations between 0 and 16 mg/l in the Trans-(**a**)) and the Cis-state (**b**)).

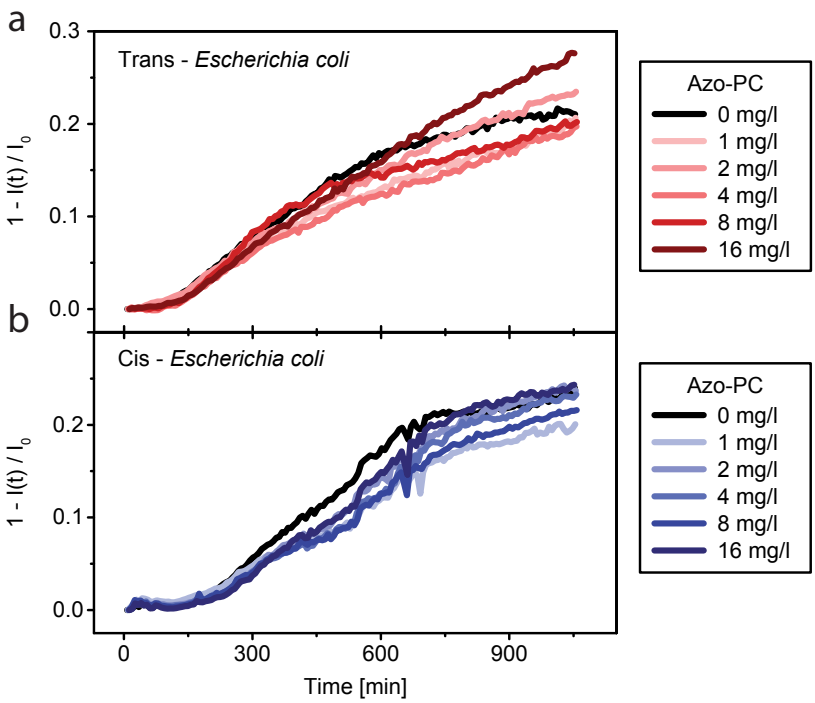


Figure A.4: **Influence of Azo-PC in the trans- and cis-state on the growth behavior of *Escherichia coli*. a)** Growth measurements of *E. coli* with 0-16 mg/l Azo-PC were conducted as a control, since *E. coli* are non-susceptible to the model-molecule of the Azo-PC trans-state. The results for Azo-PC (trans-state) show no influence of the growth of *E. coli* and are thus in good agreement with literature on PC190723 [104]. **b)** Analogous growth measurements with the cis-state of Azo-PC. The results show no strong delay of critical growth times.

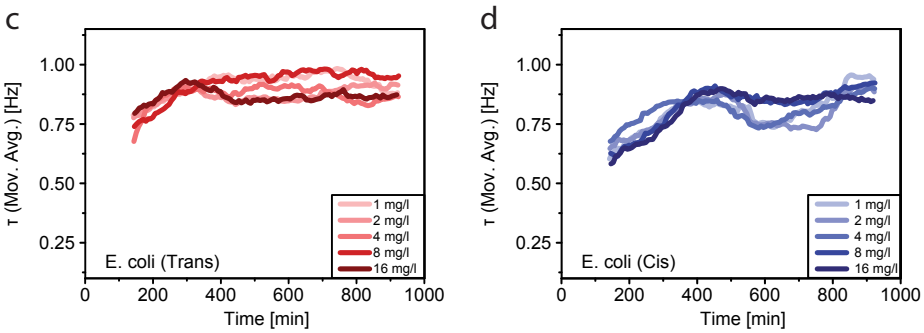


Figure A.5: **Dynamic analysis of the mobility for Azo-PC measurements of susceptible and non-susceptible strains. a)** Moving average of $\tau$ over 40 data points for Azo-PC trans-state measurements with *E. coli*. All samples show a slight initial increase, but no dependence of the mobility on the Azo-PC concentration. **b)** Analogous E. coli measurement with Azo-PC in the cis-state. Again, no effect of the Azo-PC was measured.

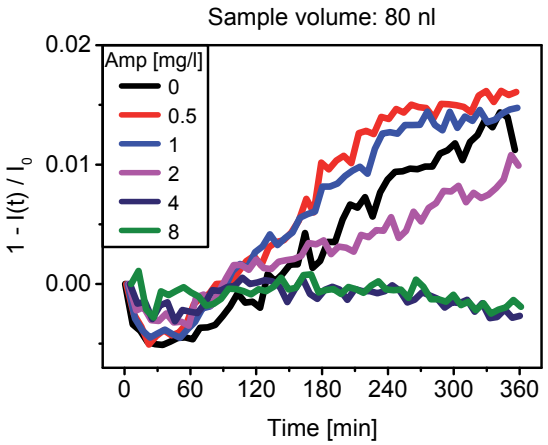


Figure A.6: **Ampicillin concentration series in sample volumes of less than 80 nl.** Diffraction peak intensity-decrease for the low volume ampicillin concentration discussed in Figure 7.7a.

# List of Publications

- D. Volbers, V.K. Stierle, K.J. Ditzel, J.O. Rädler, M. Opitz & P. Paulitschke. Interference Disturbance Analysis Enables Single-Cell Level Growth and Mobility Characterization for Antimicrobial Susceptibility Testing. *Nano Letters.* *DOI: 10.1021/acs.nanolett.8b02815.*

- K.-P. Ruehmann*, D. Volbers*, J. Aschauer, P. Paulitschke & D. Trauner. Optical Control of the Bacterial Cytoskeleton Using a Photoswitchable FtsZ-Inhibitor. *Shared first authorship. *In preparation.*

- J. Aschauer, D. Volbers & P. Paulitschke. Antimicrobial Susceptibility Testing in less than 100 Nanoliter. *In preparation.*

# Acknowledgments

There are several people that I would like to thank for helping me complete this thesis:

- Dr. Philipp Paulitschke for his guidance throughout this thesis. Especially for the interesting and productive scientific discussions which always provided me with new ideas and approaches. Furthermore, for the lunch breaks and fun group activities. I wish you all the best for your future projects!

- Prof. Dr. Joachim Rädler for giving me the opportunity to work at this great chair, for the proficient and supportive feedback as well as for his friendly and positive attitude.

- PD Dr. Madeline Opitz, for the superb collaboration, the quick and extensive feedback rounds and her warm and kind nature. Furthermore, for answering all questions concerning bacteria and for letting me work in her laboratory.

- All bachelor and master students that contributed to this, who I always enjoyed working with and from whom I learned a lot: Konstantin Ditzel for his work on the bead project, Benedikt Bichler for the work on the temperature stabilized microscopy setup and, last but not least, Julian Aschauer for the superb collaboration during his Bachelor and Master thesis.

- Dr. Bert Lorenz for correcting the paper manuscript as well as for always having a sympathetic ear and friendly mood.

- Peter Rühmann for the trouble-free collaboration on the photoswitchable compound project, albeit the time difference between New York and Munich.

- Jürgen for the countless Halong Bay visits, laid back discussions and awesome time.

- Ester for the work in the clean room and for being such a pleasant and enjoyable office neighbor.

- Valentin for being a fun office neighbor as well and for always being good for a laugh.

- Alexandra G. for the advice in the microbiology lab and for being extremely helpful and friendly at any time.

- The technical staff who helped with the sample production and setup problems, especially Philipp Altpeter, Stephan Manus and the LMU workshop.
- The dinner group, Alexandra M., Ricarda, Benedikt, and Peter for the delicious food, superb cakes, dancing nights and enjoyable lunch breaks.
- All former and current members of the AG Paulitschke for making the past years so enjoyable as well as for the group activities including the Bavarian curling and the Eisbach sessions: Andi, Andrej, Christian, Nik, Josef, Tatjana, Korbinian, Jonas and Sandro.
- All members of the LS Rädler for the awesome atmosphere at the chair, for the fun parties (especially does including Karaoke) as well as for the memorable winterschools in Antholz.
- Everyone who spell-checked and corrected parts of this thesis.
- Carolin for the great times spent during the past vacations, the exquisite cooking, the help with illustrator and photoshop as well as for the uplifting words and motivation.
- Finally, all of my friends and family with a huge special thanks to my parents, Britta and Eugen, for their endless support.